Critical behavior of a trapped interacting Bose gas

Diss. ETH No. 17793

Critical Behavior of a Trapped Interacting Bose Gas

A dissertation submitted to the
ETH Zürich

for the degree of
Doctor of Sciences

presented by

Ulrik Tobias Donner

Dipl.-Phys., University of Tübingen, Germany
born 13.10.1977 in Uppsala, Sweden
citizen of Germany

accepted on the recommendation of
Prof. Dr. Tilman Esslinger, examiner
Prof. Dr. Frédéric Merkt, co-examiner

2008

Zusammenfassung

Im Rahmen dieser Doktorarbeit wurde erstmals experimentell das kritische Regime eines gefangenen, schwach wechselwirkenden Bosegases studiert. Charakteristisch für dieses Regime, das in unmittelbarer Nähe um den Phasenübergang zum Bose-Einstein Kondensat liegt, sind starke Fluktuationen des Ordnungsparameters. Bei Annäherung an die kritische Temperatur divergiert die Korrelationslänge dieser Fluktuationen. Um diese Divergenz zu untersuchen, nutzen wir die Interferenz von Materiewellen und messen die räumliche Korrelationsfunktion erster Ordnung in Abhängigkeit von der Temperatur. Zwei Atomstrahlen werden aus unterschiedlichen Regionen eines Gases von ^{87}Rb Atomen ausgekoppelt und überlagert. Der Kontrast des resultierenden Interferenzmusters ist ein Maß für die Kohärenz der beiden Regionen. Um den Kontrast mit höchster Empfindlichkeit bestimmen zu können, setzen wir einen Resonator exzellenter Güte im stark koppelnden Regime ein, mit dem einzelne Atome im Interferenzmuster nachgewiesen werden können. Wir beobachten die Divergenz der Korrelationslänge und bestimmen den zugehörigen kritischen Exponenten der Korrelationslänge zu $\nu = 0.67 \pm 0.13$.

Wir präparieren ein Bosegas in einem Nichtgleichgewichtszustand, um das Wachstum langreichweitiger Ordnung am Phasenübergang zum Bose-Einstein Kondensat zu erforschen. Während das Gas thermalisiert und den Phasenübergang überquert, bestimmen wir Kohärenz und Dichte des Gases in Echtzeit. Dabei zeigt sich, dass das Wachstum der Kohärenz später einsetzt und früher endet als das Wachstum der Dichte.

Der Nachweis einzelner Atome in unserem Resonator stellt eine quantenmechanische Messung dar, bei der eine Materiewelle auf einen Zustand mit entweder einem oder keinem Atom im Resonator projiziert wird. Wir analysieren diesen Detektionsprozess, der auf der starken Kopplung einzelner Atome an das Lichtfeld des Resonators beruht. Die Transmission eines Lasers, der resonant mit dem leeren Resonator ist, wird stark reduziert, wenn bereits ein einzelnes Atom an das Lichtfeld koppelt. Mit dieser Methode

demonstrieren wir ein Lehrbuchbeispiel des Welle-Teilchen-Dualismus: In Analogie zum Doppelspaltversuch nach Young lassen wir einzelne Atome mit sich selbst interferieren und weisen sie dann mit Hilfe des Resonators nach.

Erstmals führen wir Experimente aus, in denen ein Bose-Einstein Kondensat kohärent mit dem Lichtfeld eines Resonators wechselwirkt. Mit Hilfe eines optischen Transportes können wir mehrere hunderttausend ultrakalte Atome in den Resonator transferieren, wo die Teilchen dann bis ins quantenentartete Regime gekühlt werden. Die neuartige Kombination von Bose-Einstein Kondensat und Resonator im stark koppelnden Regime eröffnet ein neues Gebiet der Hohlraum-Quantenelektrodynamik, in dem alle Atome identisch an das Lichtfeld koppeln. Mit einer Messung des Anregungsspektrums charakterisieren wir das System.

Abstract

The critical regime of the phase transition of Bose-Einstein condensation is studied for the first time in a trapped, weakly interacting Bose gas. In this regime, fluctuations on all length scales dominate the behavior of the gas, and the correlation length of these fluctuations diverges as the temperature approaches the critical temperature. To observe this divergence we apply a matter-wave interference technique and map out the first-order correlation function of a gas of ^{87}Rb atoms as a function of temperature. We extract two atomic beams from different regions in the sample and let them overlap. The visibility of the resulting interference pattern is a measure for the coherence of the two probed regions. An ultra-high finesse optical cavity in the strong coupling regime is used to detect single atoms in the interference pattern and to measure the visibility with ultimate sensitivity. We observe the diverging behavior of the correlation length and determine the critical exponent of the correlation length to be $\nu = 0.67 \pm 0.13$.

We apply the same interference technique to investigate in real-time the formation of long-range order in a gas crossing the phase transition to Bose-Einstein condensation, starting from a non-equilibrium situation. We find that the coherence growth starts later and ends earlier than the growth of the density of the gas. Furthermore we analyze the momentum distribution of the gas during the phase transition.

The detection of single atoms in our cavity realizes a quantum measurement of the presence of an atom, in which the matter wave is projected to a state with either one or zero atoms in the resonator. We analyze this detection process, which bases on the strong coupling of a single atom to the light field in the cavity mode. The transmission of a probe beam resonant with the empty cavity shows a significant drop if an atom couples to the cavity field. We exploit this method to demonstrate a prime example of the particle-wave duality: In a type of Young's double slit experiment we let individual atoms interfere with themselves and detect them with our cavity.

For the first time, experiments were carried out where a Bose-Einstein

condensate is coherently interacting with the light field of a resonator. Using an optical transport, we transfer several hundred thousand ultracold atoms into the cavity where we cool them to quantum degeneracy. A Bose-Einstein condensate strongly coupled to the light field of a resonator opens a new regime of cavity QED where all atoms identically couple to the cavity mode. We characterize the system by mapping out its low-excitation energy spectrum.

Contents

1 Introduction

Daily life teaches us that matter can exist in different phases and that transitions between those phases may take place if we change a controlling parameter like pressure or temperature. Raising the temperature can convert a liquid in a gas, melt a solid or demagnetize a permanent magnet. Besides the four phases solid, liquid, gaseous and plasmatic, the Bose-Einstein condensate (BEC) is considered as the fifth state of matter. While the Bose-Einstein condensed phase has been extensively investigated since its first realization in dilute gases in 1995 [1, 2], experimental studies of the phase transition itself have been scarce [3, 4, 5, 6]. In the research presented in this thesis, we explore the critical regime of the phase transition to BEC in dilute gases. This fascinating regime, where the physics is governed solely by fluctuations, could until now not be accessed experimentally.

Phase transitions occur in many different systems and their study has a long history [7, 8]. Many phase transitions manifest themselves in an abrupt change of a specific physical property like for example the density. In other cases the transition from one phase to another may be smooth. Examples for these smooth—continuous or second order—phase transitions are liquids crossing the critical point to the gas phase, the ferromagnetic-paramagnetic phase transition of a magnet or the phase transition to BEC. Second order phase transitions are accompanied by a number of typical anomalies around the critical point: physical quantities like the heat capacity or the correlation length grow without limit when the system approaches the critical point. These divergences—called critical phenomena—have their origin in large scale fluctuations appearing in the system near the critical point.

The first observation of a critical phenomenon was made in a vessel filled with carbon dioxide [9]. At boiling temperature but away from the critical point, which is defined by a certain pressure and temperature, a liquid and a gaseous phase are visible. The distinction between liquid and gas disappears right at the critical point, and the whole boiling phenomenon vanishes. The density difference between the two phases goes to zero: Instead of show-

ing two separate phases the liquid-gas mixture turns opaque. This critical opalescence is caused by bubbles of gas and droplets of liquid which intermix at all sizes from atomic length scales up to visible size—the system is governed by density fluctuations on all length scales. The bubbles and droplets of micron size cause strong scattering of light, making the mixture look opaque.

Critical phenomena are different from most other phenomena in physics in that fluctuations on widely different length scales are governing the behavior of a system. In normal situations there is a typical length scale on which the physical processes take place, like the lattice spacing in a crystal or the size of an atom or of a nucleus. At the critical point, however, all length scales from the atomic scale up to the size of the system play an important role. The vanishing of a typical length scale implies that the details of the microscopic physics become irrelevant at the critical point. The behavior is then only dependent on the symmetry properties of the system. This makes critical phenomena remarkably universal: many different and completely unrelated systems like liquids, ferromagnets or superfluids show the same critical behavior.

A prime example in the description of critical phenomena is the Ising model which consists of spins on a lattice, pointing either up or down [8]. In the ferromagnetic case there is an interaction between neighboring spins which minimizes the energy if two spins are aligned parallel. At zero temperature all spins will point into the same direction, either up or down and the system has minimum energy. This changes at finite temperature where the system explores higher energy states—the spins start to fluctuate and the interaction between them leads to a correlation of these fluctuations. At the critical temperature T_c these fluctuations are not only correlated over a small distance but over infinite distances: A single spin flip on one end of the system is correlated to a spin flip at the other end. This is a remarkable result in view of the fact that the model only takes interactions between neighboring spins into account. At the critical temperature T_c—which is determined by the strength of the interaction—the system undergoes a phase transition: below T_c the majority of the spins points in one direction, whereas above T_c there is no preferred direction of the spins.

Intuitively one expects that correlations $C(r)$ between different parts of a system decay exponentially with distance r. Far away from the critical point, the characteristic behavior of correlations can then be described by $C(r) = e^{-r/\xi}$, where ξ is the correlation length, the length scale above which the correlation function practically vanishes. For a gas, this length scale is given by the thermal de Broglie wave length.

When the temperature T approaches the critical temperature T_c, the correlation length shows critical behavior: it diverges according to $\xi \propto |\frac{T-T_c}{T_c}|^{-\nu}$, where ν is termed critical exponent [8, 10]. Exactly at the critical point the shape of the correlation function has changed drastically. The fast exponential decay has become a long-range power law decay $C(r) = r^{-\eta}$, with the critical exponent η. Correlations decaying with a power-law indicate that the system is self-similar or scale-free, because there is no characteristic length scale associated with such a power-law.

The theoretical description of critical phenomena posed one of the most challenging open questions in physics during the last century. In 1937, the Soviet physicist Landau presented a general theory of phase transitions which could qualitatively describe critical phenomena [11]. However, some years later Onsager managed to exactly calculate the thermodynamic properties of the two-dimensional Ising model [12]. Surprisingly his results showed that Landau's theory failed to predict the behavior near the critical point. This finding sparked the extensive theoretical and experimental investigation of second order phase transitions. A theory describing critical phenomena has to include fluctuations on all length scales which makes a frontal attack of this problem to appear hopeless. Yet, in 1971 Wilson solved the problem in an ingenious way, applying renormalization group theory [13]. This theory divides the problem into consecutive simpler problems which are solvable. The tools furnished by Wilson's theory allow to completely describe critical phenomena and provide a method to numerically compute quantities like critical exponents. However, the application of these conceptually brilliant methods turned out to be very challenging [10, 14], and the analysis of many interesting systems is currently subject of intense research.

To verify the theoretical findings, the comparison with more and more accurate experiments is required. Huge efforts have been made to precisely measure critical exponents, including experiments in space to minimize the influence of gravity [15]. However, to gain a more detailed understanding of both classical and quantum phase transitions [16], new experimental tools are highly desirable. In this respect, ultracold atomic gases seem to be particularly promising candidates. They can be used to prepare several model systems with virtually no defects, thereby simulating the physics of highly complicated situations of condensed matter [17]. They offer precisely controllable interactions and provide access to otherwise unaccessible properties.

In the scope of this thesis experiments were carried out observing the

critical behavior of a dilute, trapped and weakly interacting Bose gas at the phase transition of Bose-Einstein condensation. In a Bose-Einstein condensate a macroscopic number of particles occupy the same quantum state of the system, usually its ground state [18]. Such a system will show off-diagonal long-range order [19], meaning that the first-order correlation function has a finite value for distances as large as the system size. In our experiments we directly observe how the correlations of the fluctuations grow from microscopic to macroscopic dimensions as the phase transition of Bose-Einstein condensation is approached. We map out the first-order correlation function and observe the change of the exponential decay of the correlations to a power-law decay. From this data we determine the correlation length ξ as a function of temperature. We observe how the correlation length diverges when the critical point is approached and determine its critical exponent ν. In order to observe critical behavior of an ultracold gas, big experimental challenges have to be tackled: especially demanding is the precise control of the temperature of the gas and to find a measurement method which is only minimally invasive.

To be able to directly measure the correlations between two regions of the trapped gas we apply a special matter wave interference technique. We output couple atomic matter waves locally from two regions and let the two propagating waves overlap and interfere [20]. The visibility of the resulting interference pattern is a measure for the degree of correlations between the two regions. A precise detection of the modulated atomic flux is necessary to measure the visibility with high sensitivity. We achieve ultimate sensitivity employing an ultra-high finesse optical cavity in the strong coupling regime to detect single atoms [21] in the interference pattern. Because we are sensitive to single atoms, only a very low flux is needed and the disturbance of the trapped sample is negligible.

This novel method combining ultracold quantum gases and cavity quantum electrodynamics provides a new experimental tool to advance the understanding of both classical and quantum phase transitions. It allows direct and time-resolved measurements of correlations in trapped gases with high precision. Even the dynamics of a phase transition can be investigated. Applying this measurement to bosons in an optical lattice the study of the quantum phase transition from a superfluid to an insulating phase [22] can be envisioned.

Outline of the thesis:

- Chapter 2 gives the theoretical background for critical phenomena. Furthermore, the theory of cavity QED is presented.
- In Chapter 3 the experimental apparatus used for all experiments presented here is introduced.
- The observation of critical behavior of a Bose gas at the phase transition to Bose-Einstein condensation is reported in Chapter 4. We directly measure the correlation function of the gas and determine the critical exponent of the correlation length.
- In Chapter 5 we present experiments on the time-resolved measurement of the coherence growth during Bose-Einstein condensation. We investigate the dynamics of the phase transition, starting from a non-equilibrium situation.
- A modified version of Young's double slit experiment carried out with single, interfering ultracold atoms is presented in Chapter 6. The cavity QED measurement process of the presence of a single atom in the cavity is analyzed.
- In Chapter 7 we report on the transport of ultracold atoms into the cavity and on the strong collective coupling of a BEC to the cavity mode.

2 Theoretical Framework

In this chapter we present a brief introduction to the main theoretical concepts used in this thesis: the theory of critical phenomena and of cavity quantum electrodynamics. The aim is to review theoretical aspects, which will be of importance for the understanding of the experiments we report. To follow the presented discussions on Bose-Einstein condensates and on the first-order correlation function, knowledge of the concept of off-diagonal long-range order (ODRLO) is required. We add a compact overview on ODLRO and on the basic properties of Bose-Einstein condensates in Appendix A. For more detailed information the reader is referred to standard textbook literature and to the review articles cited.

2.1 Critical Phenomena

Life without the endless movement [...] *from one phase to another would be a sorry thing* (J. J. Binney in [23])

This theoretical section gives an overview of the huge research field of phase transitions and critical phenomena, which has a long standing tradition starting two centuries ago. There has been a whole set of approaches trying to tackle the challenges of a correct description of critical phenomena. After a summary of the historical development, we describe the main definitions and ideas of these different approaches. For more detailed explanations we refer to textbooks [8, 23, 10, 7, 24, 25] and review articles [26, 27, 28].

Phase Transitions

Phase transitions are traditionally divided into first-order and second-order transitions [23]. First-order phase transitions involve latent heat: as the material is cooled through an infinitesimally small temperature range around the phase transition, a finite amount of heat, the latent heat, is released. The appearance of latent heat reflects a radical reordering of the material during the phase transition. The paradigm of a first-order phase transition is the freezing of water to ice, where right at the phase transition the solid and the liquid phases of water coexist. An amount of 334 kJ/kg of latent heat has to be released to transform the water into ice.

In contrast, the behavior of a ferromagnet is a prime example for a second-order phase transition. Below a certain critical temperature T_c, the magnetization has a finite value $\mathbf{M}$. With increasing temperature of the magnet, this magnetization decreases due to thermal fluctuations of the spins. At T_c it approaches zero with infinite slope, and for $T > T_c$ the material behaves as a paramagnet. In contrast to the above example of water, there is no coexistence of the ferromagnetic and paramagnetic phase, but the two phases become indistinguishable at T_c. Consequently, there is no latent heat involved in this phase transition. This is a main feature of a second-order (also named continuous) phase transition: the properties of the system change continuously, but some of their rates (here the slope of $\mathbf{M}$) show a discontinuous behavior. Singular behavior like this is an example of a "critical phenomenon".

Both examples described above occur at a finite temperature, and in both examples the ordered phase is destroyed by thermal fluctuations. Phase transitions can also occur at zero temperature, and lots of attention has

focused on it in the last years. These so-called quantum phase transitions [16] are not triggered by thermal, but by quantum fluctuations, when a non-thermal parameter like pressure or magnetic field is changed. A famous example of an experimentally observed quantum phase transition is the superfluid to Mott insulator transition [22].

Historical Overview

One of the first experiments on critical behavior at a phase transitions was carried out in 1869 by Andrews [9], who studied the liquid-vapor critical point in carbon dioxide and observed the phenomenon of critical opalescence. When reaching the critical point, the fluid becomes milky because the density fluctuations reach the size of the wavelength of the light. Motivated by this experiment, van der Waals started to develop his theory of phase transitions. Systematic studies of the ordering in magnets followed, and a first kind of mean field theory – the molecular field theory by Weiss [29] – was developed. In the following years a wide variety of phase transitions was discovered, ranging from structural phase transitions to superfluid and superconducting phase transitions. The phase transitions were classified into first- and second-order phase transitions, with the first involving latent heat but the second not.

In 1937 Landau realized that all second-order phase transitions have in common that, at the transition point, the degree of symmetry of the system changes. Symmetry is a qualitative property, which can only appear abruptly. That is why at a second-order phase transition a certain symmetry is said to be broken. To describe this behavior of the system, Landau introduced the concept of an order parameter Φ. The thermal average of this parameter is zero in the non-ordered state (temperature above the critical temperature) and takes a finite value below the critical temperature (in the ordered phase). There is no general scheme for the definition of an order parameter, it has to be chosen for every new physical system.

In Landau theory the free energy is expanded in powers of the order parameter. This is a very general approach, because this expansion does not depend on the forces acting in the system. Landau theory proved to be very successful in the qualitative description of phase transitions. It predicts a set of critical exponents, which describe the behavior of some important physical quantities near the critical point, for example the behavior of the heat capacity, the susceptibility, the order parameter itself, or the correlation length. Those critical exponents are universal numbers and should thus – following Landau theory – be identical for every kind of phase transition. However, Onsager managed in 1944 [12] to compute exactly the partition

function and thermodynamic properties of the two dimensional Ising model. His findings, in particular the critical exponents, disagreed with the predictions from Landau theory. In addition, experiments showed that not all systems have the same critical exponents, but that there are classes of systems with the same exponents.

An extension of Landau theory was later given by the Landau-Ginzburg theory, which includes a spatially varying order parameter and thus fluctuations. When the temperature approaches the critical point, fluctuations start to dominate the system and Landau theory breaks down. The Landau-Ginzburg theory allows for an estimate of the temperature region in which fluctuations are not dominating and Landau theory is correct. However, the description of systems in the critical region, where fluctuations dominate, remained patchy.

From this challenge the ideas of non-trivial critical exponents, universality classes and of scaling relations between the critical exponents grew. In 1971 Wilson presented his renormalization group ideas, which revolutionized the understanding of phase transitions [13]. This theoretical framework, based on the Landau-Ginzburg theory, made the calculation of the critical exponents and other properties feasible and supports the picture of universality classes: The symmetry of the system and the number of components of the order parameter define the behavior of a system at a phase transition.

2.1.1 Phase Transitions and Critical Exponents

In the following discussion we will focus on the critical phenomena associated with second-order (continuous) phase transitions.

Order Parameter

A system undergoing a continuous phase transition from the high-temperature side to the low-temperature side will reduce its symmetry. For example, a ferromagnet below its critical temperature shows spontaneous magnetization into a certain direction, thereby destroying rotational invariance. Because of this reduction in symmetry, an extra parameter is needed for the description of the thermodynamics below T_c, and one introduces the order parameter Φ. The order parameter is a certain thermodynamic quantity of a system; its thermal average vanishes on one side of the phase transition, and has a non-zero value on the other side. It is a quantity which can fluctuate both in space and in time, so we can write $\Phi(\mathbf{x}, t)$.

In the above example of the ferromagnet one chooses the magnetization vector $\mathbf{M}$ as an order parameter, whereas for a Bose-Einstein condensate the

wave function ψ is the order parameter (see Appendix A.2). The temperature dependence of the order parameter for the Bose-Einstein condensate can be seen in Figure A.2 in the Appendix. The choice of the order parameter is not at all obvious, but has to be made afresh for every new system. The n-dimensional order parameter can be a scalar (like the density for the liquid-gas transition), a vector as in the above examples or a tensor. The higher the dimensionality of the order parameter is, the more complex the phase diagram will be.

Critical Exponents

Although no latent heat is involved in second-order phase transitions, this does not mean that the heat capacity is a smooth function of temperature. In fact it shows in many cases a divergence according to $\sim |\frac{T-T_\mathrm{c}}{T_\mathrm{c}}|^{-\alpha}$, where α is a so-called critical exponent. This kind of non-analytic dependence is a crucial property of continuous phase transitions. It is not limited to the behavior of the specific heat, but there are many other quantities which show a singular behavior around the critical temperature, like the susceptibility, the compressibility, the equation of states, the order parameter itself or the correlation length. Each of these properties shows a divergence at the critical temperature of the form

$$\sim |\frac{T-T_\mathrm{c}}{T_\mathrm{c}}|^{-c} . \tag{2.1}$$

The critical exponents c are typically labeled by Greek letters (α for heat capacity, β for order parameter, γ for compressibility, δ for equation of states ...). For a convenient description of these phenomena we introduce the reduced temperature

$$t = \frac{T-T_\mathrm{c}}{T_\mathrm{c}} = \frac{T}{T_\mathrm{c}} - 1 . \tag{2.2}$$

The above definition (Equation 2.1) refers only to the singular part of the interesting quantity, which is symbolized with "$\sim$". It can happen, that a critical exponent is zero, so there is no singularity. For example, $\alpha = 0$ tells us that there is no singularity in the heat capacity, which nevertheless can have a finite discontinuity at $t = 0$.

Two further important critical exponents concern the behavior of the correlation function near T_c. As we will discuss in more detail in (2.1.3), the first-order correlation function (see Equation A.9 in the Appendix) behaves for large r in the proximity of the critical temperature like

$$g^{(1)}(r) \to \frac{e^{-r/\xi}}{r^p} . \tag{2.3}$$

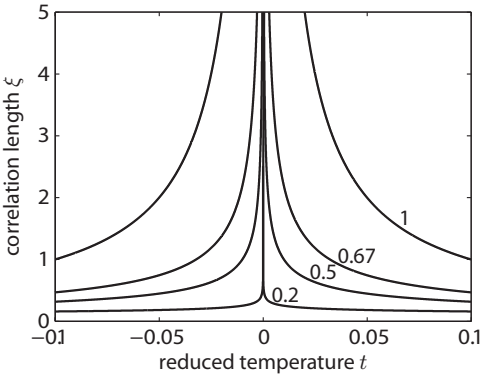

FIGURE 2.1: Divergence of the correlation length $\xi = |t|^{-\nu}$ as a function of reduced temperature $t = (T - T_c)/T_c$ for different values of the critical exponent ν. The smaller the exponent is, the sharper is the divergence. Shown are values of ν=(0.2, 0.5, 0.67, 1).

Here we introduced the correlation length ξ, which is the typical length scale over which the fluctuations of the order parameter are correlated (see 2.1.3). The exponent $p = d - 2 + \eta$ in the denominator depends on the dimensionality d of the system and on the critical exponent η. The correlation length ξ diverges, when T approaches T_c according to

$$\xi \sim |t|^{-\nu}, \tag{2.4}$$

where ν is the critical exponent for the correlation length. Figure 2.1 shows the divergence of ξ in proximity of T_c for different values of the critical exponent ν. Combining (2.3) and (2.4) it becomes clear that right at the critical temperature $\xi \to \infty$ and the nominator in (2.3) becomes unity. The first-order correlation function $g^{(1)}(r)$ will thus show for large r a power-law decay at $T = T_c$,

$$g^{(1)}(r) \to \frac{1}{r^p}. \tag{2.5}$$

It is worth noting why critical exponents have proven to be very helpful in the description of phase transitions [25]. It would of course be preferable to obtain a complete functional form for the behavior of a quantity as the specific heat or the correlation length, instead of only a number describing the singular part. However, near the critical point, the singular part is the dominating one.

Another, more important, reason for focusing on critical exponents is that they are universal, which means that they are not only valid for a specific system, but for a whole set of physical systems that can be grouped in universality classes. In addition, the critical exponents are not independent from each other, but there exists a number of scaling relations between them, arising from statistical and thermodynamical considerations.

Universality Classes

It turns out that the microscopic properties of a system are irrelevant when critical phenomena are considered. According to the universality hypothesis of Griffiths [30], physical systems fall into "universality classes" depending on the dimensionality d of the system, the dimensionality n of the order parameter and the range of interactions.

Concerning the range of interactions, one distinguishes between the case of short-ranged interactions and long-ranged interactions [31]. Short-ranged interactions are here defined by a decay of the potential as a function of distance between the particles which is faster than $r^{-(d+2)}$. In this case, which we are focusing on in the following, the behavior is universal. For long-ranged interactions the shape of the potential has to be taken into account.

Each system can be assigned to a universality class characterized by the pair (d, n). Experimental results as well as renormalization group theory suggests that all systems in the same universality class have the same critical exponents. This implies that such different systems as a superfluid and an anisotropic ferromagnet belong to the same universality class $(d = 3, n = 2)$ and show the same critical behavior at T_c. Figure 2.2 gives an overview of universality classes in the (d, n) plane.

Scaling Hypothesis

The presented critical exponents are not independent of each other, but can be related by scaling relations. Scaling means that the value of a quantity with dimension is expressed in units of a certain length scale. When this length standard is changed, the value will change accordingly. Thus, a dimensionless quantity will be invariant under this scaling.

The scaling hypothesis [32] states that in the proximity of a critical point the only characteristic length scale of a system is its correlation length ξ. Consequently ξ sets the length standard with which all other quantities with dimension are measured. Right at the critical temperature, the correlation length ξ diverges, which leads to the conclusion that the system has no

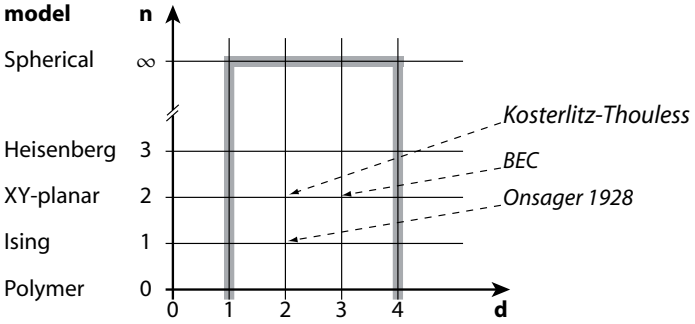

FIGURE 2.2: Overview of the universality classes, tabulated according to the dimensionality d of the system and the dimensionality n of the order parameter, together with the common model name. Some important phase transitions and the analytical solution of the Ising model by Onsager are shown. The grey box marks the boundary out of which the critical behavior of the systems is exactly known. Unfortunately the interesting physical systems lie inside the box. However, a calculation is possible by expanding the known solution in $\epsilon = 4 - d$ or in $1/n$.

characteristic length and is therefore invariant under scale transformations. The system is said to be scale invariant.

Scale invariant systems are also self-similar, which means that at any magnification there is a smaller piece of the system that is similar to the whole. This can be expressed mathematically by homogeneous functions, to which the correlation function at T_c, $g^{(1)}(r) = 1/r^p$ belongs, where p is the Hausdorff dimension. The self-similarity can be seen by increasing (scaling) the unit of length by a factor a, which transforms the correlation function as

$$g^{(1)}(r/a) = a^p g^{(1)}(r)\,. \tag{2.6}$$

If the correlation function had contained an exponential factor (like in (2.3)) it would of course not show this scale invariant behavior. At the critical temperature the scale invariance of the correlation function accounts for a scale invariance of the fluctuations: fluctuations take place on all length scales!

Under the assumption of scale invariance it is easy to derive the scaling equations by making a dimensional analysis and expressing all length scales

by $\xi \sim |t|^{-\nu}$ [8, 24]:

$$\begin{aligned} 2-\alpha &= \nu d \\ \alpha+2\beta+\gamma &= 2 \\ \gamma &= \nu(2-\eta) \\ \gamma &= \beta(\delta-1) \end{aligned} \tag{2.7}$$

These scaling laws are simple algebraic relations between the different critical exponents. They were initially based on the scaling hypothesis, but could later be proven on the basis of renormalization group theory.

Critical Slowing Down and Finite Size

In the above discussion of critical phenomena we considered systems in the thermodynamic limes and in equilibrium. However, experimentally and in numerical simulations both conditions can not be met perfectly, and this section accounts briefly for this situation.

A sharp phase transition can in general only exist in an infinite system. The finite size of a realistic system will lead to a shifting and a rounding of the critical singularities. Especially the correlation length, which diverges to infinity in the thermodynamic limes has a natural upper bound set by the size of the system. Finite-size effects can therefore be expected to become important in a temperature range, when the correlation length is on the order of the system size [33, 34, 35, 36].

The fact that, for an infinite system, the correlation length diverges to infinity and that a phase transition takes place in finite time reveals a causality problem. The growth of $\xi \to \infty$ in a finite time would mean that the growth has to be faster than the speed of light. Instead, the growth is expected to be cut off at a certain ξ, and the fluctuations will be "frozen out" [37, 38, 39]. This so-called Kibble-Zurek effect will be more pronounced when the system is quenched more rapidly across the phase transition. The timescale on which the system relaxes into equilibrium diverges, which leads to the phenomenon of critical slowing down. To evaluate whether a system is in the regime of critical slowing down or not, one has to compare the quench time (the time during which the system is forced across the critical point) with the correlation time. This correlation time can be estimated by dividing the correlation length by the characteristic velocity (typically speed of sound) with which fluctuations propagate [38].

2.1.2 Theoretical Approaches

Landau Theory

Landau theory can be understood as a unification of earlier mean-field theories such as the van der Waals theory or Weiss' molecular field theory. It is a phenomenological approach, avoiding the underlying microscopic structure and dealing only with macroscopic quantities. Landau theory is meant to describe a system in proximity of the critical point only, where the order parameter Φ is small.

This theory is based on the assumption that the free energy $\mathcal{F}$ of the system can be expanded in powers of the order parameter Φ. We can write the Landau expansion of the free energy for a system at temperature T and in an external field h (which is always zero for a Bose-Einstein condensate) as

$$\mathcal{F}(T, \Phi, h) = \mathcal{F}_0 - h\Phi + \frac{1}{2}a(T)\Phi^2 + \frac{1}{4}b(T)\Phi^4 + ... \tag{2.8}$$

Except of the term with the external field h, the expansion includes only even powers of Φ, which corresponds to the case of a second-order phase transition. To find an equilibrium situation, the free energy has to show a minimum with respect to Φ:

$$\frac{\partial \mathcal{F}(T,\Phi)}{\partial \Phi} = 0\,, \frac{\partial^2 \mathcal{F}(T,\Phi)}{\partial \Phi^2} > 0\,. \tag{2.9}$$

If $a(T), b(T) > 0$ and $h = 0$, the only minimum is $\Phi_0 = 0$, corresponding to a situation where the system is in the non-ordered phase. The situation changes for the case where $a(T) < 0$ and $b(T) > 0$, where we find the non-trivial solution

$$\Phi_0^2 = -a(T)/b(T)\,. \tag{2.10}$$

In Landau theory the expansion coefficients $a(T), b(T)$ are in turn themselves expanded in the reduced temperature t (2.2), where to lowest order $a(T) = \alpha_0 t$ and b is considered constant in the vicinity of T_c. Now the solution (2.10) can be written as

$$\Phi_0 = \pm\left(-\frac{\alpha_0 t}{b}\right)^{1/2}, \quad \text{for}\, t < 0\,. \tag{2.11}$$

With the last equation the critical exponent for the order parameter has been found: $\beta = 1/2$. From similar arguments all critical exponents can be determined [24]. They are listed in the lowest row in Table 2.1. The other values in this table are results from more refined theories discussed later.

Equation (2.11) gives two solutions for the minima of the free energy of the system. In the absence of an external field h, it is not clear in which

	n	d	α	β	γ	δ	ν	η
Ising 2D	1	2	0	1/8	7/4	15	1	1/4
Ising 3D	1	3	0.110(1)	0.3265(3)	1.2372(5)	4.789(2)	0.6301(4)	0.0364(5)
XY	2	3	-0.025 ... +0.05		1.27 ... 1.371		0.65 ... 0.700	0.026 ... 0.07
Heisenberg	3	3		0.3535 ... 0.388	1.270 ... 1.465	4.68 ... 4.85	0.642 ... 0.747	0.030 ... 0.06
Landau	-	4	0	1/2	1	3	1/2	0

TABLE 2.1: Theoretical values for the critical exponents (following [40]). All data except the two dimensional Ising model (solved by Onsager [12]) and the classical values from Landau theory are extracted from [41].

minimum the system will evolve. The situation is illustrated for the case of a one-dimensional ($n = 1$) (Figure 2.3 a) and of a two-dimensional ($n = 2$) (Figure 2.3 b) order parameter in Figure 2.3. For $n = 1$ the system has two equivalent free energy minima and is thus twofold degenerate, whereas for $n > 1$ the system shows a continuous degeneracy. A system undergoing a phase transition will be driven by fluctuations into one of the minima—the symmetry is spontaneously broken. Comparing the behavior of the order parameter (see Figure A.2 in the Appendix) to that of the free energy (see Figure 2.3) around the critical temperature, it becomes clear why second-order phase transitions are very sensitive to fluctuations: Around the critical temperature, the minimum of the free energy changes only weakly with T, while the order parameter Φ changes rapidly, and thus fluctuations which involve a large change in Φ require only a small change of free energy.

Landau theory is a mean-field theory, assuming a uniform order parameter and neglecting the fluctuations of the order parameter around its average value. Even though Landau theory provides a good understanding of phase transitions and symmetry breaking, this must lead to quantitatively wrong predictions. The influence of the fluctuations on the behavior at a phase transition was found to depend on dimensionality. Fluctuation have a decreasing effect with increasing dimensionality of both the system, d, and the order parameter, n. In fact, one can define a lower critical dimension d^- and an upper critical dimension d^+. For dimensions $d \geq d^+$, the fluctuations can be neglected, and the behavior is correctly predicted by Landau theory.

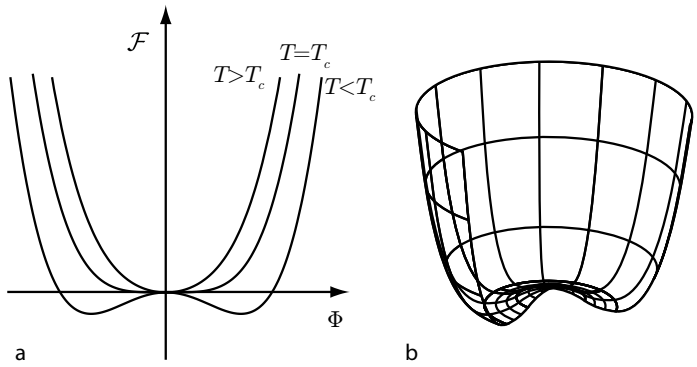

FIGURE 2.3: Dependence of the free energy $\mathcal{F}$ on the value of the order parameter Φ. (a) shows the situation for a one-dimensional ($n = 1$) order parameter for three different temperatures. Above T_c, the free energy has only one minimum, which becomes very broad for $T = T_c$. For temperatures below T_c there is a two-fold degeneracy and the system is driven by fluctuations into one realization. (b) shows the situation $T < T_c$ for a two-dimensional ($n = 2$) order parameter, where the degeneracy is continuous.

In contrast, for $d \leq d^-$ the fluctuations are so strong that they completely destroy the ordered phase, thereby inhibiting the phase transition. If the dimensionality of the system is between the critical dimensions, $d^- < d < d^+$, a phase transition will occur, but the behavior is different from Landau theory. The values for the critical dimensions depend on the universality class. For the XY-universality class ($n = 2$), to which Bose-Einstein condensation belongs, the lower critical dimension is $d^- = 2$, whereas the upper critical dimension is $d^+ = 4$.

Landau-Ginzburg Theory

Landau theory does not take any fluctuations into account. The influence of fluctuations is included by Landau-Ginzburg theory which is an extension of Landau theory. Landau-Ginzburg theory contains a fluctuating field in form of a spatially varying order parameter $\Phi(\mathbf{r})$. The theory bases on the Landau-Ginzburg free energy functional $\mathcal{F}_{\mathrm{LG}}$ which is a generalization of the Landau free energy (2.8). Due to the spatial dependence of $\Phi(\mathbf{r})$, also derivatives of the order parameter have to be included in the expansion. For an isotropic system, there is no term linear in $\nabla\Phi(\mathbf{r})$, because it would

depend on the direction of the change in $\Phi(\mathbf{r})$. Thus the simplest possible term is quadratic in $\nabla\Phi(\mathbf{r})$ and the Landau-Ginzburg free energy functional is given by

$$\mathcal{F}_{\mathrm{LG}}(\Phi(\mathbf{r})) = \int \mathcal{F}_0 - h\Phi(\mathbf{r}) + \frac{1}{2}\alpha_0 t\Phi(\mathbf{r})^2 + \frac{1}{4}b(T)\Phi(\mathbf{r})^4 + c\,(\nabla\Phi(\mathbf{r}))^2\,\mathrm{d}\mathbf{r}\,. \tag{2.12}$$

The Landau-Ginzburg free energy functional is often also called Φ^4-model. Although this model describes a phase transition in principle very well, it turns out that calculations are highly complicated [14] because higher orders have to be included in the functional (2.12) when T approaches T_c. Knowing that Landau-Ginzburg theory is correct for systems with dimensions higher than the upper critical dimension d^+, one introduces a continuous dimensionality d and tries to expand the energy functional for dimensions smaller, but close to the critical dimension. This approach is called ϵ-expansion, where $\epsilon = d^+ - d$ is the deviation from the upper critical dimension. This method can surprisingly be extended to lower dimensions, even if ϵ then is not a small parameter any more. Similar to the ϵ-expansion one can apply a $1/n$-expansion according to the dimensionality of the order parameter n. Landau theory is correct for $n = \infty$, that is why an expansion in $1/n$ was shown to be successful. The ϵ- and the $1/n$-expansion are used to reliably calculate critical exponents for the physically interesting dimensions.

Critical Region

To estimate the importance of fluctuations it is useful to compare the magnitude of the fluctuations with the mean value of the order parameter. Landau theory is correct as long as the fluctuations in the system are much smaller than the mean value of the order parameter. The amplitude of the fluctuations increases when the temperature approaches the transition temperature. One can define a temperature region around the critical temperature, the so-called critical region, in which the fluctuations dominate and thus Landau theory breaks down. The size of this region is determined by the Ginzburg criterion [42, 43, 11]

$$\frac{b^2 T_\mathrm{c}^2}{\alpha_0^{4-d} c^d} \ll |t| \ll 1\,, \tag{2.13}$$

where α_0, b and c are the expansion coefficients from (2.12) and d is the dimensionality. This means that Landau theory is only applicable in a temperature range which is sufficiently close to T_c, but not so close that fluctuations are dominating. On the other hand, this criterion also determines how close to T_c the temperature has to be in order to experimentally observe the effects of fluctuations and thus beyond mean-field behavior.

The actual calculation of the critical region is not trivial, because it depends on the microscopic details of the system. The size of the critical region is thus not universal [44]. For a conventional superconductor it can be small (10^{-14}), whereas for a high-T_c superconductor the critical region is 10^{-2}. For the case of Bose-Einstein condensation in dilute gases, the critical region has been estimated [45] in terms of the correlation length to be

$$\xi \geq \frac{\lambda_{\mathrm{dB}}^2}{\sqrt{128\pi^2 a}} \tag{2.14}$$

with the scattering length a, which yields for our experiment $\xi \geq 0.36$ µm. From this one can find via $\xi \sim |t|^{-\nu}$ the temperature range of the critical region to be on the order of 10^{-2}. Recent more advanced calculations [46] for our parameters showed that the size of the critical region is given by $t < 0.08$.

Renormalization Group Theory

In the following we want to illustrate the basic ideas of renormalization group theory. The application of this theory was a breakthrough in the description of phase transitions, and has proven to be very successful. A detailed discussion of this theory would go far beyond the scope of this thesis, and can be found in review articles [26, 28, 47] and textbooks [10, 44].

All renormalization group theories have in common that parameters which define the problem are reexpressed (transformed) in terms of some other parameters, thereby leaving the physical aspects of interest unchanged. From the behavior of these parameters under repeated transformations one can deduce the phase diagram and the critical properties of the system. Also the scaling laws, initially based on the scaling hypotheses, are found in a natural way.

A good starting point of this discussion is the Kadanoff-cell transformation [48]. For simplicity we consider the two-dimensional Ising model ($n = 1$, $d = 2$), consisting of spins on a lattice with spacing a, which can either point upwards or downwards. One can now apply a coarse-graining transformation (or renormalization) $\mathcal{R}_l$, by replacing the spins within a block of size $(la \times la)$ with a single block spin, which thereby contains l^2 spins. The direction of the block spin is given by the direction in which the majority of the contained spins point (see Figure 2.4).

The correlation length $\xi_l = \mathcal{R}_l(\xi_i)$ of the system, measured in units of the spacing $l \cdot a$ of the block spins, will now be smaller than the initial correlation length ξ_i, measured in units of the spacing a between the spins, because the physical value of the correlation length stays of course unchanged.

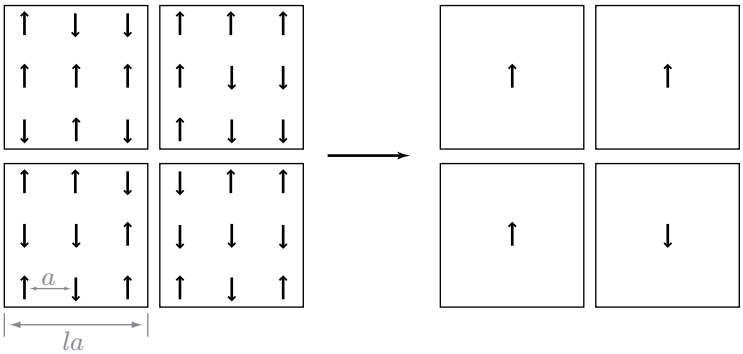

FIGURE 2.4: Block spin transformation. Spins on a lattice with spacing a are merged to blocks with length $l \cdot a$.

One can also define a Hamiltonian $\mathcal{H}_l$ for the coarse-grained system, which is identical to the Hamiltonian of the initial system, except of the new spacing between the spins. As the correlation length ξ becomes smaller under the transformation, the Hamiltonian $\mathcal{H}_l$ is further away from criticality than the initial Hamiltonian $\mathcal{H}_i$. The Hamiltonian of the system is said to have moved in the space of Hamiltonians—it flows under repeated transformations.

To be more concrete we consider the Hamiltonian to be a sum of terms describing the coupling between nearest neighbors with coupling constant K_1, next nearest neighbors (nnn) with coupling constant K_2 and so forth, where the coupling constants are temperature dependent

$$\mathcal{H} = K_1 \sum_{\langle i,j \rangle} S_i S_j + K_2 \sum_{i,j=nnn} S_i S_j + \dots \tag{2.15}$$

Under the transformation $\mathcal{R}_l$, the Hamiltonian $\mathcal{H}_l$ will be of the same form as the initial Hamiltonian $\mathcal{H}_i$. However, the set $\{K\}$ of coupling constants defining the initial Hamiltonian $\mathcal{H}_i$ will change under the transformation to a new set $\{K'\}$. For example, for a system initially without next nearest neighbor coupling, the coupling constant K_2 can become non-zero after transformation. Under repeated transformations this set of parameters is evolving in a specific way, which can be visualized in a flow diagram in coupling constants space.

Figure 2.5 shows a flow diagram for an Ising system with coupling constants K_1 and K_2. The arrows show the direction of the flows under successive renormalization group transformations.

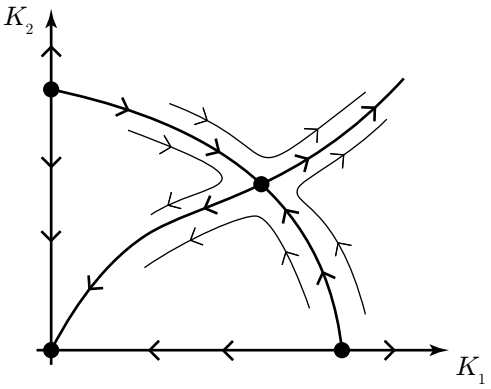

FIGURE 2.5: Flow diagram for an Ising system with nearest neighbor coupling constant K_1 and next nearest neighbor coupling constant K_2. The Hamiltonian of the system is evolving in the $K_1 - K_2$-plane under successive renormalization group transformations according to the arrows. Critical points from which the system moves away and one trivial fixed point, to which the system moves, are shown.

In the flow diagram Figure 2.5, one can find special points to which or from which the system is evolving, depending on the starting point. These points are called fixed points, and one can distinguish between trivial fixed points which attract the system and critical fixed points which are unstable.

When the system reaches a trivial fixed point, or is prepared exactly on a critical fixed point, an application of the transformation $\mathcal{R}_l$ will leave all parameters unchanged,

$$\{K^*\} = \mathcal{R}_l(\{K^*\}), \quad \xi^* = \mathcal{R}_l(\xi^*)\,, \tag{2.16}$$

where the asterisk $(^*)$ indicates that the system is on a fixed point. The second condition, which states that the correlation length stays unchanged under the transformation, can only be fulfilled for $\xi^* = 0$ or for $\xi^* = \infty$. A vanishing correlation length corresponds to a trivial fixed point, whereas an infinite correlation length corresponds to a critical fixed point. In this case the system can again be regarded as self-similar: the properties of the system stay unchanged, when one zooms out under the transformation.

From the renormalization group flow one can find the critical points and deduce properties of the system such as phase diagrams, critical temperatures and critical exponents. The calculation of the critical exponents depends on the actual realization of the transformation $\mathcal{R}_l$. The principle is to

expand the transformation $\mathcal{R}_l$ around $\{K^*\}$, to apply it to ξ^* and to compare this result to the power law $\xi \simeq |K - K^*|^{-\nu}$ expected for the behavior of the correlation length in proximity of the critical point [23, 44].

2.1.3 The Correlation Function near the Phase Transition

In the following we want to concentrate on the correlation function $g^{(1)}(\mathbf{r}, \mathbf{r}')$ of a system in proximity of a phase transition. As introduced in Section 2.1.1, the correlation function in the critical region has the asymptotic form

$$g^{(1)}(r) \underset{r>\lambda_{\mathrm{dB}}}{\longrightarrow} \frac{e^{-r/\xi}}{r^{d-2+\eta}} \quad \underset{T=T_{\mathrm{c}}}{\longrightarrow} \quad \frac{1}{r^{d-2+\eta}}\,, \tag{2.17}$$

which means it changes its shape from a mainly exponential decay to a pure power law decay when approaching the critical temperature. The correlation length ξ is a measure for the size of the regions in which the fluctuations of the order parameter are correlated. The order parameter fluctuates in domains of all sizes up to ξ. When $T \to T_{\mathrm{c}}$, the correlation length grows without limits and thus the order parameter has correlated fluctuations on all length scales.

This behavior is nicely illustrated by snapshots of the Ising model taken at different temperatures as shown in Figure 2.6. Black pixels correspond to spin down, white to spin up. For high temperatures there are many small black and white regions, generating a pepper-and-salt effect, and there is no preferred direction of the spins, i.e. there is no net magnetization. When the temperature is lowered towards T_{c}, the typical size of the monochrome regions steadily increases, until the critical temperature is reached. At this point fluctuations from infinitesimally small to infinitesimally large appear and the system can be seen as self-similar. Also at the critical temperature, no net magnetization is visible, but the correlated regions extend over the whole lattice. Below T_{c} the system spontaneously chooses a preferred spin direction, in this case spin down, corresponding to a majority of black pixels. The size of the white regions, corresponding to the fluctuations on top of the net magnetization, decreases with decreasing temperature. The correlation length ξ corresponds in this example to the typical size of the white regions. It diverges at T_{c} and falls off again when the temperature moves away from the critical temperature.

We now turn to the correlation function of a trapped Bose gas near the critical point. As explained in Appendix A.1, for temperatures far above T_{c}, the first order correlation function $g^{(1)}(r)$ falls off to zero on the length scale of the thermal de Broglie wavelength $\lambda_{\mathrm{dB}} = \sqrt{\frac{2\pi\hbar^2}{mk_{\mathrm{B}}T}}$, whereas for

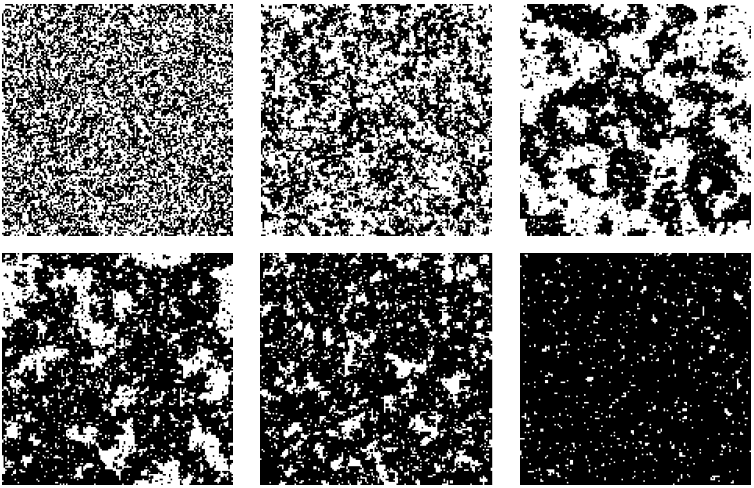

FIGURE 2.6: Snapshots of the two-dimensional Ising model at different temperatures. Black pixels correspond to spin down, white to spin up. At high temperatures (top left) there is no net magnetization, and the fluctuating regions are very small. Going to the right in the upper row the temperature is decreased, until around T_c (top right), the fluctuating regions are correlated over the whole system, but there is still no net magnetization. In the lower row the temperature is below T_c and the system has chosen to be by the majority spin down. Going to the right in the lower row, for even lower temperatures the size of the fluctuating regions decreases.

temperatures below the phase transition $g^{(1)}(r)$ falls off to a constant finite value for large distances r. The metamorphosis from the one to the other situation happens in the critical region, where the first order correlation function is given by the above equations.

The first order correlation function of a trapped Bose gas has been studied theoretically by Naraschewski and Glauber [49]. They used a mean field theory for this evaluation, neglecting critical fluctuations. The resulting critical exponent for the correlation length will thus be $\nu = 1/2$. However, to gain qualitative understanding of the correlation function near T_c their approach is very instructive. Following their reasoning, the first order correlation function $\langle \hat{\Psi}^\dagger(\mathbf{r})\hat{\Psi}(\mathbf{r}')\rangle$ of an ideal Bose gas can be evaluated for

temperatures above T_c with help of the Wigner function

$$\langle\hat{\Psi}^\dagger(\mathbf{r})\hat{\Psi}(\mathbf{r}')\rangle = \int e^{-i\mathbf{p}\cdot(\mathbf{r}-\mathbf{r}')/\hbar}\, W\left(\mathbf{p}, \frac{\mathbf{r}+\mathbf{r}'}{2}\right) \mathrm{d}\mathbf{p}\,, \tag{2.18}$$

where the Wigner function $W(\mathbf{p},\mathbf{q})$ is given in local density approximation by

$$W(\mathbf{p},\mathbf{q}) = \frac{1}{(2\pi\hbar)^3}\frac{1}{e^{(p^2/2m+V(\mathbf{q})-\mu)/k_\mathrm{B}T}-1}\,. \tag{2.19}$$

Expanding the Wigner function in a sum, the integral (2.18) reads

$$\langle\hat{\Psi}^\dagger(\mathbf{r})\hat{\Psi}(\mathbf{r}')\rangle = \frac{1}{(2\pi\hbar)^3}\int e^{-i\mathbf{p}(\mathbf{r}-\mathbf{r}')/\hbar}\sum_{s=1}^{\infty} e^{-s(\frac{\mathbf{p}^2}{2m}+V(\frac{\mathbf{r}+\mathbf{r}'}{2})-\mu)/k_\mathrm{B}T}\mathrm{d}\mathbf{p}\,. \tag{2.20}$$

Carrying out the integration over the momentum and using the de Broglie wavelength λ_dB yields

$$\langle\hat{\Psi}^\dagger(\mathbf{r})\hat{\Psi}(\mathbf{r}')\rangle = \frac{1}{\lambda_\mathrm{dB}^3}\sum_{s=1}^{\infty}\frac{1}{s^{3/2}} e^{-s(V(\frac{\mathbf{r}+\mathbf{r}'}{2})-\mu)/k_\mathrm{B}T} e^{-\frac{1}{s}\pi\frac{(\mathbf{r}-\mathbf{r}')^2}{\lambda_\mathrm{dB}^2}}\,. \tag{2.21}$$

We are interested in the situation of a harmonic trapping potential with an average trapping frequency $\bar{\omega}$. With the origin of the coordinate system chosen at the minimum of the trapping potential, we can write the correlation function for $x = y = 0$ as a function of $\Delta z = z - z'$, where z and z' are centered around the origin

$$\langle\hat{\Psi}^\dagger(z)\hat{\Psi}(z')\rangle = \frac{1}{\lambda_\mathrm{dB}^3}\sum_{s=1}^{\infty}\frac{1}{s^{3/2}} e^{s\mu/k_\mathrm{B}T} e^{-\frac{1}{s}\pi\frac{\Delta z^2}{\lambda_\mathrm{dB}^2}} \tag{2.22}$$

This sum can numerically be evaluated, where the chemical potential μ must be determined self-consistently by using the normalization relation for the atom number N [50]

$$N = \sum_{k=1}^{\infty}\frac{e^{k\mu/k_\mathrm{B}T}}{(1-e^{-k\hbar\bar{\omega}/k_\mathrm{B}T})^3}\,. \tag{2.23}$$

In Figure 2.7, a normalized version of the correlation function (2.22) is shown for three different temperatures shortly above the transition temperature T_c. Although the chosen temperatures differ only by a few percent of T_c, the corresponding correlation functions are clearly different. The closer the temperature is to the transition temperature, the longer ranged are the correlations in the system. The graph shows in grey the correlation

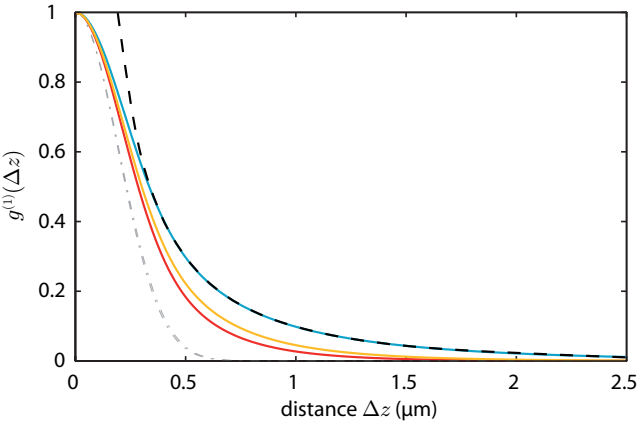

FIGURE 2.7: First order correlation function of a trapped Bose gas according to [49]. Shown are the numerically calculated correlation functions for three different temperatures (red – $1.05T_c$, orange – $1.03T_c$, blue – $1.01T_c$). The two grey dash-dotted lines are Gaussians with a width given by the de Broglie wavelengths $\lambda_{dB} \simeq 0.5\,\mu m$ corresponding to the highest and the lowest temperature. They are nearly indistinguishable in this graph. While λ_{dB} changes only marginally over the temperature region, the correlation function becomes significantly longer ranged for smaller temperatures. The black dashed line is a fit of the asymptotic correlation function (2.3) to the curve, for $\Delta z > \lambda_{dB}$.

function according to Equation A.11, which describes the decay of the correlation function on the length scale of the thermal de Broglie wavelength. The curves for both the highest and lowest temperature considered here lie so close that they cannot be distinguished in this graph. The de Broglie length changes only marginally over the temperature range considered here, and it is obvious that the correlations range longer than λ_{dB}. Additionally, the asymptotic correlation function (2.3) has been fitted to the correlation function for the lowest temperature and is shown as black dashed line.

The correlation function (2.22) can be approximated (as shown in Appendix B) to the asymptotic form

$$\langle \hat{\Psi}^\dagger(z)\hat{\Psi}(z')\rangle \to \frac{1}{\Delta z} e^{-\Delta z/\xi}, \tag{2.24}$$

with the correlation length $\xi = \sqrt{\frac{\hbar^2}{2m|\mu|}}$.

The dependence of the chemical potential μ on the temperature ($T -$

$T_c)/T_c$ gives the critical exponent ν for the correlation length. For the homogeneous noninteracting Bose gas the chemical potential is proportional to the square of $(T - T_c)/T_c$, resulting in $\nu = 1$. By contrast, for the noninteracting trapped case, the chemical potential depends only linear on temperature, resulting in $\nu = 1/2$. However, the noninteracting gas is a peculiar case from the theoretical point of view and its relation to the interacting system is limited.

The presence of interactions adds richness to the system. Determining the value of the critical exponent using Landau theory (see 2.1.2) results in a value of $\nu = 1/2$ for the homogeneous system. In the critical regime, Landau theory fails and critical fluctuations have to be taken into account. The corresponding renormalization group calculations give a value of $\nu \approx 0.67$. However, for the trapped interacting gas—the system realized typically in experiments—until now no theoretical prediction for the critical exponent has been made.

2.2 Cavity Quantum Electrodynamics

Cavity QED is about what happens to light and, in particular to its interaction with matter when it is trapped inside a box. (S. Dutra in [51])

Quantum electrodynamics (QED) describes the interaction between matter and light. It is a relativistic quantum field theory of electrodynamics, dealing with the mutual interaction between electrically charged particles, mediated by the exchange of photons. For example it successfully describes the spontaneous decay of an excited atom: The process of spontaneous emission is not an inherent property of atoms, but results from the interaction of an atom with the vacuum field. As a consequence, a modification of the vacuum field of light should lead to a change in the rate of spontaneous emission [52].

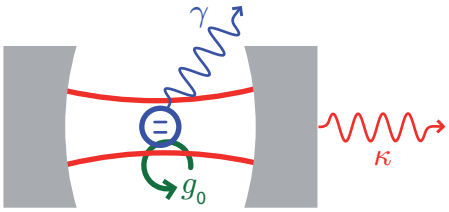

FIGURE 2.8: A two-level atom coupled with coupling strength g_0 to a single mode of a cavity. The excitation is coherently exchanged between the atom and the cavity. Dissipative processes of the system are decay of the cavity field at rate κ and decay of the atomic dipole moment at rate γ.

This is where cavity quantum electrodynamics comes into play, because an effective modification of the vacuum field can be achieved with the help of a cavity, which singles out specific modes from the free electromagnetic field mode spectrum. An atom inside a cavity will experience an enhanced coupling to the field modes supported by the cavity and will thus increase its rate of spontaneous emission into the cavity mode by the Purcell factor $Q\lambda^3/V_{\mathrm{cav}}$, where Q is the quality factor of the cavity, λ is the wavelength of the radiation and V_{cav} is the mode volume of the cavity. If the quality of the resonator is high enough, the excitation is coherently exchanged between the cavity and the atom. To reach this so called strong-coupling regime the decay rates of the systems—the decay rate of the field in the resonator κ and the spontaneous decay rate γ of the atomic dipole moment—have to be smaller than the coupling rate $g_0 \gg (\kappa, \gamma)$.

At its core, cavity QED describes the coupling of a two-level emitter to a single mode of a resonating structure. A very natural system consists of a single two-level atom placed in the mode of a high finesse cavity (see Figure 2.8). Cavity QED is an active area of research and meanwhile a wide variety of emitters like molecules, ions, Rydberg atoms, quantum dots or cooper pair boxes have been coupled to different kinds of resonating structures ranging from Fabry-Pérot or microtoroid resonators to microcavities based on photonic bandgap crystals or microwave circuit structures [53].

In our experiment, ultracold ^{87}Rb atoms are coupled to an ultra-high finesse optical cavity. To provide a theoretical basis for the understanding of the cavity QED part of our experiments, we will in the following first introduce some basic resonator properties before the interaction of a single atom with the field of a cavity is explained in the Jaynes-Cummings model. The theory is extended to the situation where many atoms are coupled simultaneously to the cavity mode, which is described by the Tavis-Cummings Hamiltonian. This section ends with a brief discussion of dissipation in cavity QED systems.

2.2.1 Optical Resonators

A Fabry-Pérot (or plane parallel) interferometer consists of two parallel, highly reflective flat mirrors separated by a variable distance l_{res}. The mirrors can be characterized by their reflectivity $\mathcal{R}$, their transmissivity $\mathcal{T}$ and by their losses $\mathcal{L}$, where $\mathcal{R}+\mathcal{T}+\mathcal{L}=1$. All three parameters depend in general on the wavelength λ of the light impinging onto the mirror, and are determined by the coating of the mirrors and the materials used.

The electro-magnetic field confined in the resonator forms a sinusoidal standing wave pattern and is discretized by the condition $n\lambda/2 = l_{\mathrm{res}}$ for the wavelength λ, where n is an integer. By varying either the length l_{res} of the cavity or the wavelength λ of the light, this resonance condition can be fulfilled and the transmission of the cavity will show a maximum. The resonance condition can also be written in terms of frequency, introducing the free spectral range $\Delta\nu_{\mathrm{FSR}}$, which is the frequency distance between neighboring longitudinal cavity modes:

$$\Delta\nu_{\mathrm{FSR}} = \nu_{n+1} - \nu_n = \frac{c}{2\,l_{\mathrm{res}}}\,. \tag{2.25}$$

The line width $\Delta\nu$ of the resonances depends on $\Delta\nu_{\mathrm{FSR}}$ and on the reflectivity $\mathcal{R}$ of the mirrors (assuming identical mirrors):

$$\Delta\nu = \Delta\nu_{\mathrm{FSR}}\frac{1-\mathcal{R}}{\pi\sqrt{\mathcal{R}}} = \frac{\Delta\nu_{\mathrm{FSR}}}{\mathcal{F}}\,, \tag{2.26}$$

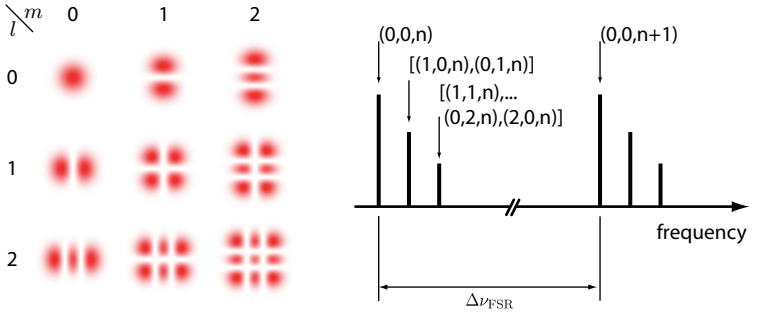

FIGURE 2.9: Left: Intensity distribution of the lowest order TEM modes of a cavity. Right: Frequency spacing of the TEM modes in a near planar cavity. The longitudinal modes (characterized by n) are spaced by the free spectral range $\Delta\nu_{\mathrm{FSR}}$.

where the finesse

$$\mathcal{F} = \frac{\pi\sqrt{\mathcal{R}}}{1-\mathcal{R}} \underset{\mathcal{R}\to 1}{\approx} \frac{\pi}{1-\mathcal{R}} = \frac{\pi}{\mathcal{L}+\mathcal{T}} \tag{2.27}$$

has been introduced. A photon will be reflected $\mathcal{F}/\pi$ times on average before it gets lost due to scattering or absorption. As a consequence, the power inside the cavity is $\mathcal{F}/\pi$ times larger than the input power. The line width $\Delta\nu$ is closely related to the decay rate $\kappa = \pi\Delta\nu$ of the field in the resonator, which is half the decay rate of the intensity inside the resonator.

To achieve a stable resonator geometry and thus to assure photon confinement in the radial direction, many applications work with curved mirror surfaces which fulfill the stability condition $0 \leq (1-l_{\mathrm{res}}/r_{c1})(1-l_{\mathrm{res}}/r_{c2}) \leq 1$, where r_{c1} and r_{c2} are the radii of curvature of the two mirrors.

The spatial distribution of the field inside the cavity is given by the solutions of the differential equations describing the field [54]. The general solution is provided by the Hermite-Gaussian modes, which read at the position of the mode waist ($z = 0$):

$$E_{lmn}(x,y,0) = H_l\left(\frac{\sqrt{2}x}{w_0}\right) H_m\left(\frac{\sqrt{2}y}{w_0}\right) e^{-\frac{x^2+y^2}{w_0^2}} . \tag{2.28}$$

The fundamental TEM_{00} mode ($l = m = 0$) is the Gaussian mode, which is characterized by the order of the longitudinal mode n only. For indices $l, m \neq 0$ a more complex transverse structure describes the field in the cavity (see Figure 2.9).

For a TEM_{00} mode the radius of the mode as function of distance z from its waist with waist radius w_0 is given by

$$w(z) = w_0 \sqrt{1 + \left(\frac{z}{z_\mathrm{R}}\right)^2}\,, \tag{2.29}$$

with the Rayleigh length $z_\mathrm{R} = \pi w_0^2/\lambda$. The radius of curvature of the wavefront is

$$R(z) = z\left(1 + \left(\frac{z_\mathrm{R}}{z}\right)^2\right)\,. \tag{2.30}$$

In a cavity with curved mirrors the wavefront radius of curvature must match the radius of curvature of the mirror surface at the position of the mirrors. From this condition one finds an expression for the mode waist of a Gaussian beam in the cavity

$$w_0 = \sqrt{\frac{l_\mathrm{res}\lambda}{2\pi}} \sqrt[4]{\frac{2r_c}{l_\mathrm{res}} - 1}\,. \tag{2.31}$$

In our experiment we use a symmetric ($r_{c1} = r_{c2} = r_c$) and near planar ($r_c \gg l_\mathrm{res}$) cavity. Since the length of the resonator is short compared to the Rayleigh length, the wavefronts in the resonator can be approximated as plane waves and the mode waist will vary only marginally over the cavity length. An integration over the cavity mode function gives the mode volume $V_\mathrm{cav} = \pi/4 w_0^2 l_\mathrm{res}$. For this type of resonators the frequency spectrum is given by [55]

$$\nu_{lmn} = \frac{c}{2l_\mathrm{res}}\left(n + \frac{1+l+m}{\pi}\left(\frac{2l_\mathrm{res}}{r_c}\right)^{1/2}\right)\,. \tag{2.32}$$

2.2.2 Jaynes-Cummings Model

The Jaynes-Cummings model describes the interaction of a two-level atom with the quantized mode of a cavity, neglecting dissipative effects. It is of great interest in quantum optics because of its physical significance and because it is analytically solvable. The atom is characterized by its ground state $|g\rangle$ with energy $\hbar\omega_g$ and its excited state $|e\rangle$ with energy $\hbar\omega_e$. The cavity mode supports photons of energy $\hbar\omega_c$ and is described in a Fock state basis $|n\rangle$, with n being the number of photons in the cavity mode. In the rotating wave approximation the Jaynes-Cummings Hamiltonian then reads

$$\mathcal{H}_\mathrm{JC} = \hbar\omega_g \hat{g}^\dagger\hat{g} + \hbar\omega_e \hat{e}^\dagger\hat{e} + \hbar\omega_c \hat{a}^\dagger\hat{a} + \hbar g_0(\hat{e}^\dagger\hat{a}\hat{g} + \hat{g}^\dagger\hat{a}^\dagger\hat{e})\,, \tag{2.33}$$

where $\hat{g}$ (or $\hat{g}^\dagger$) and $\hat{e}$ (or $\hat{e}^\dagger$) are the annihilation (or creation) operators of an atom in state $|g\rangle$ or $|e\rangle$ respectively, and $\hat{a}$ (or $\hat{a}^\dagger$) is the annihilation (or creation) operator of a photon in the cavity mode. The operators $\hat{g}$ and $\hat{e}$ are not independent but have to satisfy the condition $\hat{g}^\dagger\hat{g} + \hat{e}^\dagger\hat{e} = 1$. The atom field coupling strength is given by g_0, which depends on the dipole matrix element $\mathcal{D}$ for the transition $|g\rangle \rightarrow |e\rangle$ and on the cavity mode volume V_{cav}:

$$g_0 = \frac{\mathcal{D}}{\hbar}\sqrt{\frac{\hbar\omega_c}{2\epsilon_0 V_{\mathrm{cav}}}}\,. \tag{2.34}$$

From the expression for g_0 one sees that a small mode volume is preferable to increase the coupling strength.

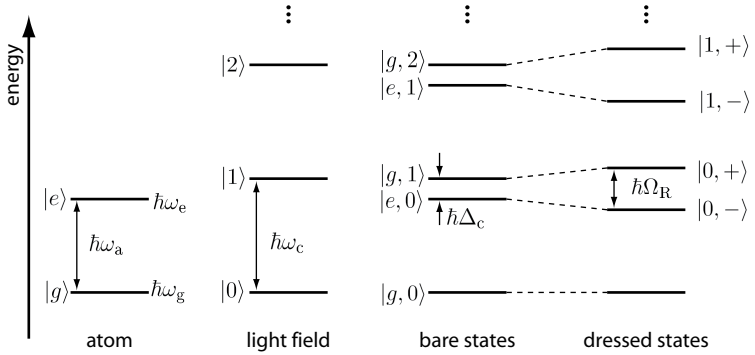

FIGURE 2.10: Coupling of a two-level atom to the light field contained in a cavity. Ground and excited state of the atom have an energy difference of $\hbar\omega_a$, whereas the energy of one photon in the cavity is $\hbar\omega_c$, resulting in a detuning $\Delta_c = \omega_c - \omega_a$. The coupling leads to a splitting of the dressed states by the Rabi frequency $\hbar\Omega_R$.

For the Hamiltonian without the interaction term the bare states $|g, n+1\rangle$ and $|e, n\rangle$ form a canonical basis, displaying the state of the atom and the number of photons in the cavity. Subtracting the energy $\hbar\omega_g$ from the Hamiltonian and expanding it in the bare state basis, (2.33) now reads in the $(n+1)$-excitation sector

$$\mathcal{H}_{\mathrm{JC}} = \hbar\begin{pmatrix} (n+1)(\Delta_c + \omega_a) & \sqrt{n+1}g_0 \\ \sqrt{n+1}g_0 & (n+1)\omega_a + n\Delta_c \end{pmatrix}, \tag{2.35}$$

with the atomic transition frequency $\omega_a = \omega_e - \omega_g$ and the detuning of the cavity resonance with respect to ω_a, $\Delta_c = \omega_c - \omega_a$.

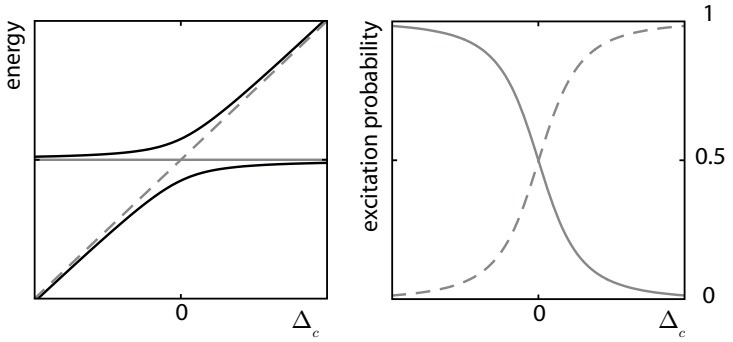

FIGURE 2.11: Left: Energy diagram of the Jaynes-Cummings model as a function of cavity detuning Δ_c for a single excitation in the system. The bare states are shown in grey, where the solid line corresponds to $|e,0\rangle$, and the dashed line to $|g,1\rangle$. The dressed states $|\pm\rangle$ are shown as solid black lines. Right: Excitation probability for the upper dressed state of the left picture. For $\Delta_c < 0$, the excitation is mainly in the atom, whereas for $\Delta_c > 0$ it is mainly in the light field.

Diagonalizing the Hamiltonian one finds the eigenenergies $E_{n,\pm}$ corresponding to the eigenstates $|n,+\rangle$ and $|n,-\rangle$:

$$E_{n,\pm} = \hbar(n+\frac{1}{2})\Delta_c + \hbar(n+1)\omega_a \pm \sqrt{\Delta_c^2 + 4g_0^2(n+1)} \quad (2.36)$$

$$|n,+\rangle = \cos\phi_n|g,n+1\rangle + \sin\phi_n|e,n\rangle \quad (2.37)$$

$$|n,-\rangle = -\sin\phi_n|g,n+1\rangle + \cos\phi_n|e,n\rangle\,, \quad (2.38)$$

where the dressed states $|n,\pm\rangle$, split by the n-photon Rabi frequency $\Omega_{\mathrm{R}}^n = \sqrt{\Delta_c^2 + 4g_0^2(n+1)}$, are expressed as a linear combination of the bare states, which corresponds to a rotation in the Hilbert space of the system by the mixing angle

$$\phi_n = \frac{-2g_0\sqrt{n+1}}{\Delta_c - \sqrt{4g_0^2(n+1)+\Delta_c^2}}\,. \quad (2.39)$$

It is instructive to plot the bare state excitation probabilities of the system as a function of detuning Δ_c for one of the dressed states. The weight of the bare states changes with detuning and for increasing detuning the dressed states become more and more cavity- respectively atom-like (see Figure 2.11). For very large detuning the dressed states approach the bare states, as expected. In an experiment which is sensitive to the cavity output, only the cavity-like part of the spectrum in Figure 2.11 can be recorded.

2.2.3 Tavis-Cummings Model

The Jaynes-Cummings model, which describes a single atom interacting with the cavity mode, can be extended to the case where N atoms are participating in the process. We modify the single-atom Hamiltonian (2.33) accordingly by summing over all N atoms in the system [56], where the atom i is localized at $\mathbf{r}_i$ and thus couples with a position dependent coupling strength $g(\mathbf{r}_i)$

$$\mathcal{H} = \sum_{i=1}^{N} \hbar\omega_g \hat{g_i}^\dagger \hat{g_i} + \sum_{i=1}^{N} \hbar\omega_e \hat{e_i}^\dagger \hat{e_i} + \hbar\omega_c \hat{a}^\dagger \hat{a} + \sum_{i=1}^{N} \hbar g(\mathbf{r}_i)(\hat{e_i}^\dagger \hat{a} \hat{g_i} + \hat{g_i}^\dagger \hat{a}^\dagger \hat{e_i}) \,. \tag{2.40}$$

The total excitation operator $\hat{n}_T = \hat{a}^\dagger\hat{a} + \sum_i \hat{e_i}^\dagger \hat{e_i}$ commutes with the Hamiltonian (2.40), so that its eigenspectrum breaks up into manifolds corresponding to the number of total excitations n_T in the system. In our typical experiments we work with very low light intensities, so that an analysis taking only the lowest two manifolds $n_T = \{0, 1\}$ into account is justified. The absolute ground state of the system with $n_T = 0$ is given by the situation where all atoms are in the ground state and the cavity contains no photon: $|0_c; g_1, g_2, \ldots, g_N\rangle$. Following this notation we can introduce the basis states for the manifold $n_T = 1$ with one excitation in the system: for $|1_c; g_1, g_2, \ldots, g_N\rangle$ all atoms populate their ground states and the excitation manifests as a photon in the cavity mode, whereas for $|0_c; g_1, \ldots, e_i, \ldots, g_N\rangle$ there is no photon in the cavity and a single atom (atom i) is excited.

For indistinguishable atoms the latter state is a Dicke state [57]. These states can be written as a coherent superposition of all possible realizations with a single atomic excitation

$$|0_c; g_{N-1}, e\rangle = \frac{1}{\sqrt{N}} \sum_{i=1}^{N} |0_c; \delta_{1i}, \delta_{2i}, \ldots, \delta_{Ni}\rangle \,, \tag{2.41}$$

where δ_{ij} is the Kronecker symbol and 0 (1) corresponds to an atom in its ground (excited) state. The Dicke states are of importance for the description of excitations in coherent spin states, and are currently explored for the realization of quantum memories [58].

A substantial and quite radical step to simplify the Hamiltonian (2.40) was done by Tavis and Cummings [59], who assumed identical coupling of all atoms ($g(\mathbf{r}_i) = g$). Under this condition, (2.40) is solvable and recovers for $n = 1$ the results of the Jaynes-Cummings Hamiltonian, but now with a collective coupling of $g\sqrt{N}$ instead of the single-atom coupling g_0. Accordingly, the splitting of the bare states caused by the coupling will be increased by a factor of $\sqrt{N}$.

Realizing the strict condition of identical coupling for N atoms seems to be impossible at the first glance. However, coupling a BEC to a cavity turns out to be a perfect realization of the Tavis-Cummings model—in a BEC all atoms populate the same wave function and thus also couple identically to the mode of a cavity.

2.2.4 Dissipation in Cavity QED Systems

Every realization of a cavity QED system will naturally include dissipation, as the system couples to the environment and cannot be considered as a closed system anymore. The usually unavoidable dissipation due to decay of the excited atomic state (at rate γ) and due to decay of the cavity field (at rate κ) will significantly alter the pure Hamiltonian evolution. Although coupling to the environment disturbs the system and is thus undesirable, it is also a prerequisite for gathering information from the system. An open cavity QED system can be pumped from the outside and produces a continuous photon flux output which is not taken into account by the Jaynes-Cummings Hamiltonian in its fundamental form.

To model the dissipative cavity QED system, standard quantum optics methods have to be applied, leading to a master equation for the density operator. Details can be found elsewhere [60], for here we concentrate on the solution for the intracavity photon number of a weakly pumped system. The intracavity photon number is an important experimental parameter, because it is directly proportional to the cavity output. For a given pump rate η one finds the average photon number [61, 62]

$$\langle \hat{a}^\dagger \hat{a} \rangle = \eta^2 \frac{\Delta_p^2 + \gamma^2}{(\gamma\kappa + g_0^2 - \Delta_p(\Delta_p - \Delta_c))^2 + (\Delta_p\kappa + (\Delta_p - \Delta_c)\gamma)^2}, \qquad (2.42)$$

where $\Delta_p = \omega_p - \omega_a$ is the detuning of the probe beam frequency ω_p from the atomic resonance. In Figure 2.12 the intra cavity photon number is shown as a function of cavity and probe detuning. An experiment relying on the cavity output flux only gives a signal when the system is "cavity like". Also shown in Figure 2.12 is the intra cavity photon number as a function of both coupling strength g_0 and probe detuning Δ_p for the cavity detuning $\Delta_c = 0$.

To characterize a cavity QED system one can compare the coupling strength g_0, which defines the splitting of the dressed states, to the loss rates γ and κ which define the line widths in the spectrum. It is instructive to look at the single-atom cooperativity

$$C_1 = \frac{g_0^2}{2\gamma\kappa} \qquad (2.43)$$

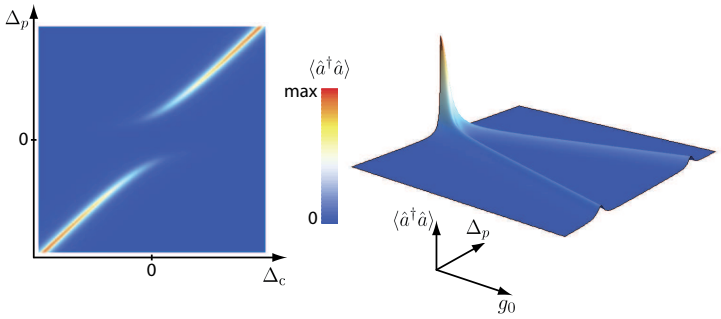

FIGURE 2.12: Intra cavity photon number $\langle \hat{a}^\dagger \hat{a} \rangle$ in a Jaynes-Cummings like system including dissipation. Left: $\langle \hat{a}^\dagger \hat{a} \rangle$ as a function of cavity detuning Δ_c and probe detuning Δ_p for a system in the strong coupling regime. Right: $\langle \hat{a}^\dagger \hat{a} \rangle$ as a function of coupling strength g_0 and probe detuning Δ_p. This graph corresponds to a section through the left graph at $\Delta_c = 0$ for different couplings g_0. The strong coupling regime is reached when the two branches are separated.

as a squared quality factor [63], where the "oscillator" in this case is given by the coherent transfer of excitation between the cavity and the atom. A significant change in the energy spectrum of a coupled atom-cavity system can be expected when the atom number is larger than the critical atom number

$$N_c = \frac{1}{C_1} = \frac{2\gamma\kappa}{g_0^2}. \tag{2.44}$$

The critical photon number n_c is defined as the number of intracavity photons which saturate the atomic system

$$n_c = \frac{\gamma^2}{2g_0^2}. \tag{2.45}$$

With the above definitions, one can introduce the condition for strong coupling $g_0 \gg (\gamma, \kappa)$, i.e. a system with a high Q-factor with single atoms and single photons. A cavity QED system in the strong coupling regime is sensitive to changes in atom and photon number on the single quantum level. This implies that besides fascinating experiments on extensions of the above theory such a highly sensitive system is also ideally suited for the detection of single atoms [21].

3 Preparing and Probing Ultracold Atoms

For the experiments described in this thesis we used an apparatus integrating a ultrahigh-finesse optical cavity into a system able to produce Bose-Einstein condensates. It was designed starting in 2001 to combine the research fields of BEC and cavity QED for the first time.

The two main constituents of the apparatus are the ultrahigh vacuum (UHV) system and the laser setup, accompanied with electronic devices, computer controls and cameras. Excellent vacuum requirements have to be met in order to prepare the atoms in a perfectly isolated environment. The ultrahigh-finesse optical cavity, including a vibration isolation system had to be installed in close proximity to the position where the BEC is produced, which posed a challenge in designing the setup. As a result all magnetic coils needed for cooling and trapping of the atoms were put into the UHV chamber, and a novel design including nested vacuum chambers was developed. The vacuum chamber and the surrounding optical elements are installed on an optical table.

The lasers deliver the light needed for cooling, trapping, manipulation and detection of the atoms, as well as for the stabilization and probing of the cavity system. All lasers are installed on a second optical table. Here, intensities and frequencies of all light sources are controlled before the light is injected into polarization maintaining optical fibers which guide the light to the optical table with the vacuum setup. The experiment is computer controlled with help of a software developed in our research group.

This chapter gives an overview of the experimental apparatus with which the measurements described in this thesis were carried out. After introducing the setup we describe the main steps for production of a BEC in the magnetic trap and for the detection of single atoms in the cavity, located 36 mm below the magnetic trap. This chapter ends with a description of the optical transport of atoms from the magnetic trap into the cavity. At the position of the cavity mode the atoms are trapped in a crossed beam dipole trap and a BEC is produced, opening the path to new experiments

(see Chapter 7).

The experimental apparatus—except the optical transport and the production of a BEC in the cavity—is described in detail in the theses of my predecessors Anton Öttl [64] and Stephan Ritter [65] as well as in an article presenting and characterizing our system [66].

3.1 Experimental Setup

3.1.1 Vacuum System

The vacuum system consists of two nested steel chambers which are operated at different pressures (see Figure 3.1). The inner chamber is connected to a part containing the dispensers, our repository for Rubidium atoms. It provides with a pressure of 10^{-9} mbar an environment for efficient loading of the magneto-optical trap (MOT), which needs a high vapor pressure of ^{87}Rb atoms. The inner chamber can be optically accessed through windows (see Figure 3.2) separating it from the main chamber. It is connected to the main chamber with a differential pumping tube. Through this tube the atoms collected in the MOT are transported magnetically into the main chamber.

The main chamber itself is kept at a pressure of 10^{-11} mbar, minimizing the loss of ultracold atoms due to collisions with background gas atoms. The inner chamber including the magnetic coils is mounted on the top flange of the main chamber, while its bottom flange supports the assembly for the cavity. The whole vacuum system is covered with a mu-metal shielding to reduce the influence of fluctuating external magnetic fields on the cold atoms. A magnetically quiet environment is a prerequisite for all experiments relying on the selective output coupling of atoms from the magnetically trapped ensemble.

The coils needed for the MOT, the magnetic transport and the trapping of the atoms in the final QUIC trap (quadrupole Ioffe configuration) [67] are shown in a section of the experimental setup in Figure 3.2.

3.1.2 Cavity Setup

The ultrahigh-finesse optical cavity used in our experiments consists of two highly reflective dielectric Bragg mirrors with ultralow losses. The coating provides a reflection band centered around $\lambda = 780\,\text{nm}$ with a width of 40 nm. The radius of curvature of the mirror surfaces is 75 mm, which, together with a length of the cavity of 175.9 µm results in a near-planar resonator geometry. The mode waist radius is 25.25 µm, such that the cavity mode volume is $88 \cdot 10^3\,\mu\text{m}^3$. The free spectral range is 852 GHz and the cavity linewidth is 2.5 MHz, resulting in a finesse of $\mathcal{F} = 340 \cdot 10^3$. A slight birefringence splits the resonance frequency of the cavity for the two orthogonal, principal polarization axes by 1.7 MHz.

The length of the cavity can be varied with a piezo tube (see Figure 3.3). The piezo tube has four radial bores of 1 mm diameter which allow for lateral

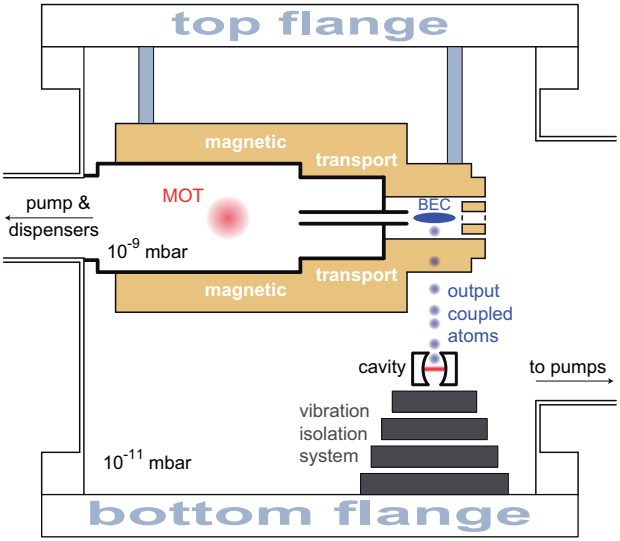

FIGURE 3.1: Sketch of the vacuum system. With an inner chamber at a pressure of 10^{-9} mbar and a main chamber at a pressure of 10^{-11} mbar the design meets the requirements for combining a BEC with a cavity. In the inner chamber the atoms are cooled in a magneto-optical trap before they are transported magnetically to the main chamber. Here they are evaporatively cooled to BEC in a magnetic trap 36 mm above the cavity. The cavity is mounted on a vibration isolation system supported by the bottom flange of the main chamber, while the inner chamber and the magnetic coils are suspended on the top flange. Figure adopted from [66].

access of atoms and laser beams. The cavity is mounted on top of a vibration isolation system which prevents coupling of acoustic noise to the cavity.

In the experiments presented in this thesis we probe the transmission of the cavity with a probe laser, which can be locked relative to an atomic resonance (typically at λ=780.2 nm). The length of the cavity—and with it its resonance frequency—has to be stabilized relative to the probe laser with an accuracy better than $0.5\lambda/\mathcal{F} \approx 1$ pm. We stabilize it with a Pound-Drever-Hall lock [68] using a stabilization laser at λ=830 nm and apply a locking scheme [69, 66] that allows us to independently adjust the cavity resonance and the frequency of the probe laser. The power of both the stabilization and the probe laser are independently actively controlled.

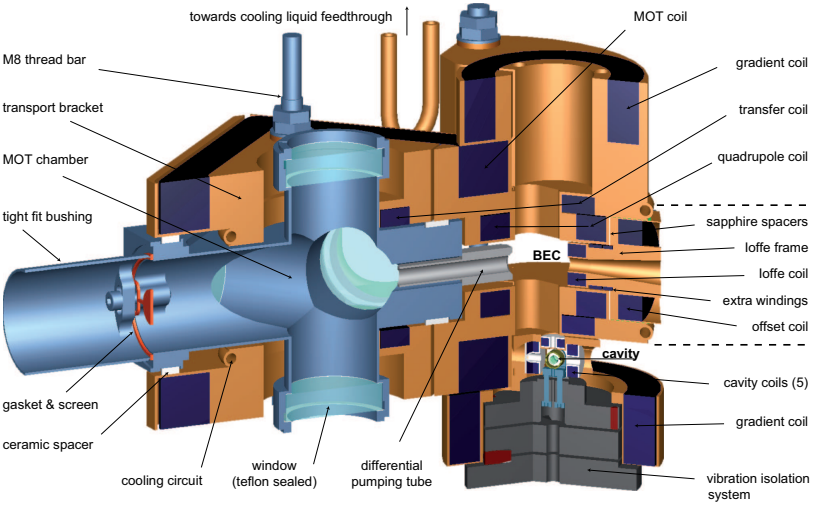

FIGURE 3.2: Section through the complete assembly inside the main vacuum chamber including all magnetic coils. It illustrates the inner chamber with the windows and the differential pumping tube connecting the two vacua. The nested design of the different magnetic coils is cooled via a cooling fluid circuit. Figure adopted from [66].

3.2 Experimental Procedure

The experiment is operated periodically with a cycle time of approximately 60 s. During each run of the experiment a new BEC is created. In the experiments described in Chapter 4–6 the ultracold cloud of atoms is trapped magnetically in the QUIC trap. We investigate the sample by output coupling atoms (see Section 4.3.2) and detecting them with our cavity.

3.2.1 Preparation of Ultra-Cold Atomic Samples

The experiment starts with loading the magneto-optical trap with ^{87}Rb atoms from the dispenser source [70]. The MOT operates on the D2 line of ^{87}Rb ($5^2S_{1/2} \rightarrow 5^2P_{3/2}$) at a wavelength of 780 nm. After 18 s of loading, about $2{\cdot}10^9$ atoms are collected in the MOT. The magnetic fields are switched off and we sub-Doppler cool the atoms in a 10 ms optical molasses phase. A homogeneous magnetic field is applied and the atoms are optically pumped during 2 ms to the low-field seeking state $|F = 1, m_F = -1\rangle$. All

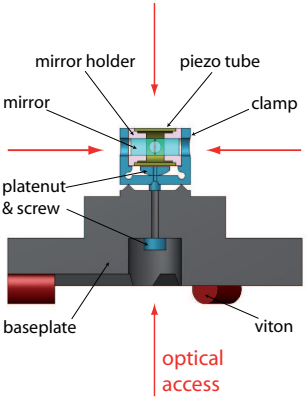

FIGURE 3.3: Plane cut through the assembled cavity design. The mirrors are mounted in ceramic holders. Their distance can be controlled with help of a piezo tube which is pre-loaded by the clamp. The piezo tube features four radial bores which give optical access to the interior. Figure adopted from [66].

lasers are shut off, the cloud is magnetically trapped and the transport sequence starts. The atoms are conveyed within 1 s of magnetic transport [71] over a distance of 82 mm until they reach the position of the QUIC trap in the main chamber.

In the QUIC trap we perform radio frequency induced evaporative cooling over 25 s and end up with pure Bose-Einstein condensates of up to $3 \cdot 10^6$ atoms in a trap with trapping frequencies of $(\omega_x, \omega_y, \omega_z) = 2\pi \cdot (38.5, 7.3, 29.1)$ Hz. We can apply resonant absorption imaging on all three axes to determine atom number and temperature of the cloud after time of flight.

3.2.2 Single-Atom Detection

From the magnetically trapped sample we output couple atoms by shining in resonant microwaves which locally spin-flips atoms into an untrapped state (see Section 4.3.2 and 4.3.3). The freed atoms fall downwards due to gravity and hit the cavity mode 36 mm below the magnetic trap (see Figure 3.1). The detection of single atoms falling through the cavity mode exploits the strong coupling between the atom and the cavity mode. The presence of an atom in the cavity mode leads to a splitting of the resonance line of the empty cavity by more than the cavity linewidth (see Section 2.2.2). The

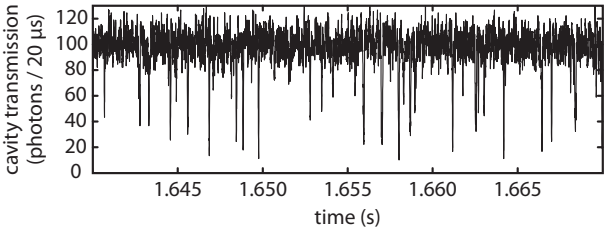

FIGURE 3.4: Cavity detection recording of single atoms falling through the cavity mode. The sudden drop of the shot-noise limited cavity transmission clearly identifies single atom transits. Figure adopted from [66].

transmission of a probe laser resonant with the initially empty cavity will significantly drop due to the presence of a single atom in the cavity.

The atom-field coupling rate g_0 in our system is large compared to the dissipative rates, the decay rate κ of the cavity field and the dipole decay rate γ of the atom: with the relevant cavity QED parameters $(g_0, \kappa, \gamma) = 2\pi \cdot (10.6, 1.3, 3.0)\,\mathrm{MHz}$, the system is in the strong coupling regime.

We monitor the transmission of the probe beam through the cavity with a single-photon counting module, where the detection efficiency for an intracavity photon is 5 %. A typical trace of the cavity transmission with single atoms passing the cavity mode is shown in Figure 3.4. We integrate the signal from the single-photon counting module over 20 µs and set the criterion for single detection events to a minimum reduction of 4 times the standard deviation of the shot noise limited empty cavity transmission. We estimate the false atom detection rate to be below $0.5\,\mathrm{s}^{-1}$. The detection efficiency was measured to be $(24\pm5)\,\%$ for atoms output coupled from a BEC and estimated to be 1 % for atoms output coupled from a thermal cloud. This efficiency is mainly limited by the spatial extend of the atomic beam being larger than the cavity mode [66].

3.3 Preparation of a BEC Inside the Cavity

In a second set of experiments we investigate the interaction of a BEC strongly coupled to the cavity mode (see Chapter 7). We added an optical transport to the system described above, that conveys the atoms from the QUIC trap into the cavity. During the transport, the atoms are trapped in the dipole potential of a red detuned standing wave pattern formed by two counterpropagating laser beams. This standing wave pattern—and with it

the trapped atoms—can be shifted by detuning the relative frequency of the two laser beams [72, 73]. At the position of the cavity mode the atoms are transferred into a crossed beam dipole trap, where we produce a BEC in a final evaporation stage. A sketch of the transport is shown in Figure 3.5.

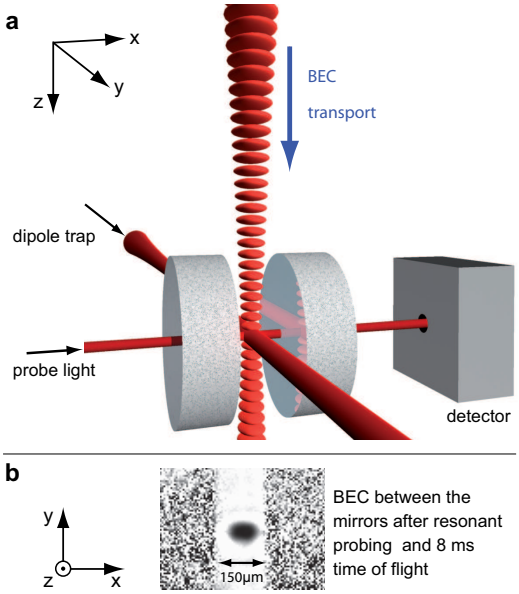

FIGURE 3.5: **a**, 36 mm above the cavity, $3.5 \cdot 10^6$ ultracold atoms are loaded into the dipole potential of a vertically oriented one-dimensional optical lattice. This trumpet-shaped standing wave has its waist inside the ultrahigh-finesse cavity and is composed of two counter-propagating laser beams. A vertical translation of the lattice transports the atoms into the cavity mode. There, they are loaded into a crossed-beam dipole trap formed by a focused beam oriented along the y axis and one of the transport beams. **b**, Almost pure condensates with $2.2 \cdot 10^5$ atoms are obtained.

3.3.1 Optical Setup

All laser beams used for transport and trapping of the atoms are provided from different tapered amplifiers seeded by the same external cavity diode laser. The diode laser is locked with a Doppler-free rf-spectroscopy to a ^{133}Cs resonance at 852 nm to guarantee an absolute frequency stability. Lock-

ing this laser on a different resonance results in a different final position of the transported atoms. Frequencies and intensities of the laser beams are precisely controlled by acousto-optical modulators, which are driven by home-built, computer controlled direct digital synthesizers [74], locked to a 10 MHz GPS standard.

The optical fibres guiding the light from the laser table to the table with the vacuum chamber are suspended in an isolatedly mounted tube to minimize pickup of phase noise. We measured the relative phase noise of the two transport beams with an interferometer. At a difference frequency of 50 kHz the phase noise is less than -100 dBc/Hz at an offset frequency of 10 kHz. With these parameters we transport the atoms without significant heating due to phase noise.

The optical access for the transport beams is limited because they need to be thread through the spacing of ∼150 µm between the cavity mirrors. A beam with a too big waist at the position of the cavity would be cut by the mirrors. On the other hand, a too tight focus would result in a strongly divergent beam, being cut at another position in the vacuum chamber. Perpendicular to the axis of the cavity we have better spatial access and the beam waist can be chosen larger.

We use cylinder lens telescopes to achieve an aspect ratio of 1:2 for the transport beams. They are focused to the position of the cavity with a $f = 400\,\mathrm{mm}$ achromatic lens. We measured the beam waists to be $(w_x, w_y) = (25, 50)\,\mu\mathrm{m}$. At the position of the magnetic trap the standing wave has spread to $(w_x, w_y) = (390, 200)$ µm. This beam geometry is optimized to be only minimally cropped by parts inside the vacuum chamber and we achieve a transmission of more than 92 % through the chamber including losses at the windows.

3.3.2 Transport of the Atoms

We found that we achieve BECs with higher atom number at the position of the cavity mode, when we transport a cold but thermal cloud of atoms and cool to quantum degeneracy after the transport, instead of loading already a BEC into the transport beams. A BEC trapped in the vertically oriented standing wave potential shows Bloch oscillations due to the gravitational acceleration. Because of interactions between the atoms these oscillations dephase rapidly and lead to heating and the destruction of the BEC.

We prepare $3.5 \cdot 10^6$ ^{87}Rb atoms in the $|F, m_F\rangle = |1, -1\rangle$ state close to the critical temperature in the QUIC trap 36 mm above the cavity. During 300 ms we ramp up a horizontal magnetic field which shifts the minimum of the magnetic trap over 400 µm to the position of the trap provided by

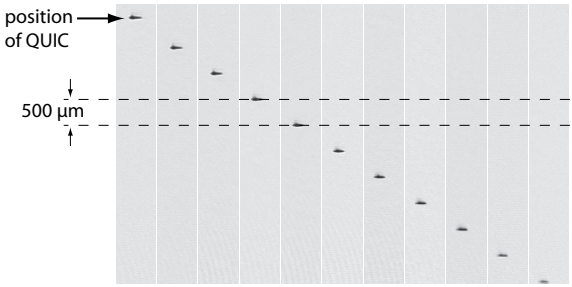

FIGURE 3.6: Optical transport of a cold atomic cloud. Shown are absorption images of atoms trapped in the potential of the standing wave, starting from the position of the magnetic trap (QUIC). Gravity points downwards and the cloud has been transported over a distance of 500 µm between successive images.

the transport lasers. In the next 100 ms the power of both transport beams is ramped up to the maximally available power of 76 mW in each beam. This yields a trap depth of 1.1 µK and trapping frequencies of $(\omega_x, \omega_y, \omega_z) = 2\pi \cdot (23, 6, 17.5 \cdot 10^3)$ Hz. We switch off the magnetic trap and apply a small magnetic field to provide a quantization axis, such that the atoms are solely trapped in the standing wave potential.

Initially the difference frequency between the counterpropagating transport beams was chosen to be $\delta = 0$, resulting in the standing wave. By tuning δ to a negative value, the standing wave pattern, and with it the atoms, moves downwards at a velocity $v = \lambda\delta/2$. The frequency difference as a function of time t is given by

$$\delta = \frac{\delta_{\max}}{2}\left(1 - \cos(\frac{2\pi t}{T})\right), \tag{3.1}$$

where $\delta_{\max} = 1690$ kHz is the maximum detuning and the transport is completed in $T = 100$ ms. This yields a maximum acceleration of 22.4 $\mathrm{m\,s^{-2}}$. The power in the laser beams is kept constant until the intensity at the position of the atoms has increased by a factor of ten. Subsequently, this intensity is kept constant. Absorption images of successive steps of the transport are shown in Figure 3.6. Because of continuous evaporative cooling during the transport, the number of atoms arriving at the cavity is reduced to typically 8.4×10^5 atoms with a small condensate fraction present.

The location of the cavity mode can be determined by loading the atoms into the dipole potential formed by the stabilization light of the cavity at a

wavelength of $\lambda = 830\,\mathrm{nm}$. The number of atoms remaining in this trapping potential after switching off both transport beams is a measure for how good the final position of the transport overlaps with the cavity mode.

3.3.3 Trapping at the Position of the Cavity Mode

At the position of the cavity mode, the atoms are loaded into a crossed-beam dipole trap formed by one of the transport beams and an additional, horizontal dipole beam with a waist radius of $w_x = w_z = 27\,\mu\mathrm{m}$ (see Figure 3.5). The frequency of this dipole beam is detuned by a few hundred MHz with respect to the frequency of the transport beams. We increase the power of the horizontal beam from zero to its maximum value of 42 mW during 30 ms. Afterwards the power of the upper transport beam is shut down in 30 ms. A final stage of evaporative cooling is performed by suitably lowering the laser power in both remaining beams to final trapping frequencies $(\omega_x, \omega_y, \omega_z) = 2\pi \times (290, 43, 277)\,\mathrm{Hz}$, ending up with an almost pure condensate of 2.2×10^5 atoms.

4 Critical Behavior of a Trapped Interacting Bose Gas

The phase transition of Bose-Einstein condensation is studied in the critical regime, where fluctuations extend far beyond the length scale of thermal de Broglie waves. Using matter-wave interference we measure the correlation length of these critical fluctuations as a function of temperature. The diverging behavior of the correlation length above the critical temperature is observed, from which we determine the critical exponent of the correlation length for a trapped, weakly interacting Bose gas to be $\nu = 0.67 \pm 0.13$.

After an introduction to the idea of the measurement we present an extended analysis of the applied method of two-frequency output coupling. We give details on the evaluation of the data and close the chapter with a discussion.

The experimental results of this chapter have been published in [75]: T. Donner, S. Ritter, T. Bourdel, A. Öttl, M. Köhl and T. Esslinger, *Critical Behavior of a Trapped Interacting Bose Gas*, Science 315, 1556 (2007), and in [76]: M. Köhl, T. Donner, S. Ritter, T. Bourdel, A. Öttl, F. Brennecke, T. Esslinger, *Criticality and Correlations in Cold Atomic Gases*, Advances in Solid State Physics 47, 79 (2008).

4.1 Introduction

Phase transitions are among the most dramatic phenomena in nature, when minute variations in the conditions controlling a system can trigger a fundamental change of its properties. The phase transition scenario of Bose-Einstein condensation in a weakly interacting atomic gas lies in the same universality class (3D XY) as the λ-transition of liquid helium. A BEC in a dilute gas is unique as it is free of impurities and the two-body interactions are precisely known. As the gas condenses, trapped bosonic atoms of a macroscopic number accumulate in a single quantum state and can be described by the condensate wave function, the order parameter of the transition. However, it has proven to be experimentally difficult to access the physics of the phase transition itself. In particular, the critical regime has escaped observation as it requires an extremely close and controlled approach to the critical temperature.

We report on a measurement of the correlation length of a trapped Bose gas of ^{87}Rb atoms within the critical regime just above the transition temperature. We observe the divergence of the correlation length ξ when approaching the critical point at T_c and determine the critical exponent ν of the correlation length.

Idea of the Measurement

Critical exponents are in most experiments determined by measuring thermodynamic properties of a system, like the heat capacity. However, quantum gases are mesoscopic systems with typically only some 10^6 particles, so that the extraction of a critical exponent from a thermodynamic property would need so far unmatched sensitivity. The trick in this experiment is not to measure a thermodynamic property but to directly measure the single-particle density matrix $\langle\hat{\Psi}^\dagger(\mathbf{r})\hat{\Psi}(\mathbf{r}')\rangle$, which is the first-order correlation function. From this, the correlation length can be extracted. By measuring the correlation length as a function of temperature we obtain its critical exponent. The challenge of this experiment is to have an accurate determination of the density matrix $\langle\hat{\Psi}^\dagger(\mathbf{r})\hat{\Psi}(\mathbf{r}')\rangle$ and to control the temperature increment precisely. Because we want to measure correlations in the same sample at different temperatures, our method must be only minimally invasive.

The applied method can be seen in close analogy to the famous double slit experiment of Thomas Young, where the coherence properties of a light field are measured [77]. In Young's experiment, a double slit with slit distance d is illuminated by the light field. The two slits are coupling the incoming light field to two new wave functions which can interfere. The visibility

of the interference pattern on a screen is a direct measure for the spatial coherence of the light. If the light field is perfectly phase coherent over the distance d, the visibility will be 1, whereas the interference pattern vanishes for vanishing coherence. Carrying out the experiment as a function of slit distance yields the first order correlation function of the light field.

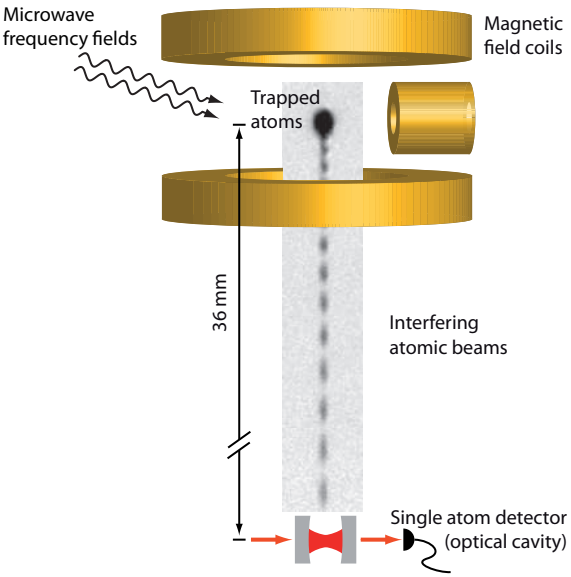

FIGURE 4.1: Sketch of the experimental principle. The atomic cloud is prepared near the critical temperature in a magnetic trap. Atoms can be extracted from well defined horizontal planes by shining in resonant microwave fields, which transfer atoms locally to an untrapped state. A double slit experiment is realized by output coupling atoms from two planes. The absorption image shows the interference pattern of the matter waves. The visibility of the interference pattern can be continuously monitored with a high-finesse optical cavity used as a single atom counter.

In our experiment, atomic matter waves are extracted from two horizontal planes in the cloud, whose position—and thereby distance—can be accurately controlled [20]. The matter waves overlap and travel downwards due to gravity. Because of the difference in gravitational potential, the matter waves from the two planes have at the same position different phases, which leads to an interference pattern. The visibility of this interference

pattern is a measure for the phase coherence of the atomic cloud, locally probed at the positions of the two planes. The distance between two arbitrary points on the two planes is irrelevant: The length which corresponds to the slit distance is given by the shortest distance between the horizontal planes, because the interference happens only in direction of gravity. By measuring the visibility of the interference pattern for different distances of the two planes, the single-particle density matrix can be mapped out.

This idea was first applied in the group of Tilman Esslinger in Munich. In their experiments [20], a high flux of output coupled atoms was needed, because the visibility of the interference pattern was determined in absorption images. After taking the absorption image with resonant light, the sample was heated drastically and the experiment had to be repeated.

In our experiment the sample may be only minimally affected by the measurement, because we want to continuously monitor the visibility of the interference pattern. In addition, strong output coupling would change the properties of the gas. To circumvent these drawbacks of the original idea [20], we extend it and use a single atom detector through which the interference pattern passes, instead of absorption imaging. The single atom detector, in our experiment a high finesse optical cavity in the strong coupling regime, allows us to reduce the flux of atoms by a factor of 10^4 with respect to the absorption image. This novel method is thus only minimally invasive and features all requirements mentioned above. A sketch of the experimental principle is shown in Figure 4.1.

We prepare the atomic cloud slightly below the critical temperature, such that a small condensate fraction is present. The sample will then heat up at a very low and constant rate due to heating mechanisms inherent to our apparatus. We continuously and weakly output couple atoms and record the visibility of the interference pattern as a function of time, which corresponds to temperature.

This procedure is carried out for different distances of the output coupling planes, in order to map out the single-particle density matrix as a function of both distance and temperature (see Figure 4.2). The collected data is divided into small temperature intervals, and for each interval the correlation length is extracted from the correlation function. We finally end up with the correlation length as a function of temperature, which we fit with a power law to find the critical exponent ν of the correlation length.

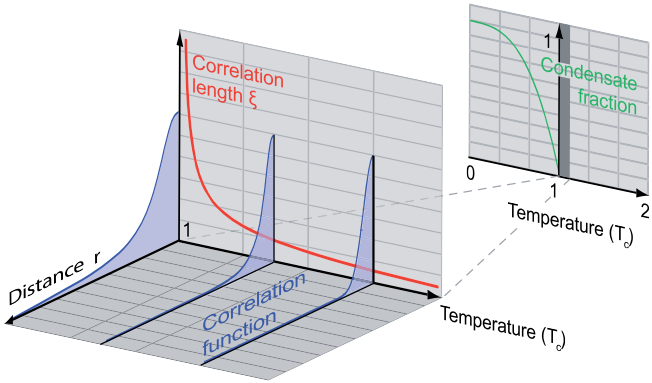

FIGURE 4.2: Schematics of the correlation function and the correlation length close to the phase transition temperature of Bose-Einstein condensation. Above the critical temperature T_c the condensate fraction is zero (see right) and for $T \gg T_c$ the correlation function decays approximately as a Gaussian on a length scale set by the thermal de Broglie wavelength λ_{dB}. As the temperature approaches the critical temperature long-range fluctuations start to govern the system and the correlation length ξ increases dramatically. Exactly at the critical temperature ξ diverges and the correlation function decays algebraically for $r > \lambda_{dB}$ (see Equation (4.1)).

4.2 Background

4.2.1 Theory

In a Bose gas the physics of fluctuations of the order parameter is governed by different length scales. Far above the phase transition temperature, classical thermal fluctuations dominate. Their characteristic length scale is given by the thermal de Broglie wavelength λ_{dB} and the correlation function can be approximated by $\langle\hat{\Psi}^\dagger(r)\hat{\Psi}(0)\rangle \propto \exp(-\pi r^2/\lambda_{dB}^2)$ with r being the separation of the two probed locations [49]. Nontrivial fluctuations of the order parameter close to the critical temperature become visible when their length scale becomes larger than the thermal de Broglie wavelength. The density matrix of a homogeneous Bose gas for $r > \lambda_{dB}$ can then be expressed by the correlation function [8]

$$\langle\hat{\Psi}^\dagger(r)\hat{\Psi}(0)\rangle \propto \frac{1}{r}\exp(-r/\xi), \tag{4.1}$$

where ξ denotes the correlation length of the order parameter. More precisely $\langle\hat{\Psi}^\dagger(r)\hat{\Psi}(0)\rangle \propto r^{-(1+\eta)}\exp(-r/\xi)$ with η being a critical exponent (see also Section 2.1.3). However, the calculated and measured values of η are on the order of 10^{-2} and therefore we neglect η in our analysis. The correlation length ξ is a function of temperature T and diverges as the system approaches the phase transition (see Figure 4.2). This results in the algebraic decay of the correlation function with distance $\langle\hat{\Psi}^\dagger(r)\hat{\Psi}(0)\rangle \propto 1/r$ exactly at the phase transition. The theory of critical phenomena predicts a divergence of ξ according to a power-law

$$\xi \propto |(T - T_\mathrm{c})/T_\mathrm{c}|^{-\nu}, \tag{4.2}$$

where ν is the critical exponent of the correlation length and T_c the critical temperature. The value of the critical exponent depends only on the universality class of the system.

Determining the value of the critical exponent using Landau's theory of phase transitions results in a value of $\nu = 1/2$ for the interacting, homogeneous system [10]. This value is the result of both a classical theory and a mean-field approximation to quantum systems. However, calculations initially by Onsager [12] and later the techniques of the renormalization group method [10] showed that mean-field theory fails to describe the physics at a phase transition. Very close to the critical temperature—in the critical regime—the fluctuations become strongly correlated and a perturbative or mean-field treatment becomes impossible, making this regime very challenging.

We consider a weakly interacting Bose gas with density n and the interaction strength parameterized by the s-wave scattering length $a = 5.3\,\mathrm{nm}$ in the dilute limit $n^{1/3}a \ll 1$. In the critical regime the fluctuations of $\hat{\Psi}$ become more dominant than its mean value. Mean-field theory, which takes no fluctuations into account, fails in this regime. The size of the critical regime can be determined by the Ginzburg criterion $\xi > \lambda_\mathrm{dB}^2/(\sqrt{128}\pi^2 a) \simeq 0.4\,\mu\mathrm{m}$ [45]. This criterion in correlation length can be converted to a criterion in reduced temperature, which gives for our system approximately $|T - T_\mathrm{c}|/T_\mathrm{c} \lessapprox 10^{-2}$. Recent, more detailed calculations [46] for the parameters of our experiment showed that the critical region is given by $|T - T_\mathrm{c}|/T_\mathrm{c} < 0.08$. The enhanced fluctuations in the critical regime manifest themselves also in a nontrivial shift of the critical temperature of Bose-Einstein condensation, which is a topic of current discussion [78, 79, 80, 81, 82].

Meanwhile, advanced theoretical methods have increased the understanding of the critical regime in a gas of weakly interacting bosons [78, 79, 80, 83, 84]. The most accurate calculations for the 3D XY universality class, to which the phase transition to Bose-Einstein condensate both in dilute

gases and in liquid ^{4}He belongs, give for the homogeneous system values of $\nu = 0.67155 \pm 0.00027$ resulting from a high-precision Monte Carlo study [85] and $\nu = 0.67098 \pm 0.00020$ resulting from a seven-loop Φ^4 theory [86]. Yet, the theoretical description of the experimental situation, a Bose gas in a harmonic trap, has remained unclear.

4.2.2 Experiments

The critical regime of a weakly interacting Bose gas offers an intriguing possibility to study physics beyond the usual mean-field approximation [87]. However, until now such effects have been observed in cold atomic gases only in systems with reduced dimensionality. The transition from a one dimensional interacting gas in the superfluid phase to the Mott insulating phase can not be correctly described in mean-field theory and has been experimentally demonstrated [88]. In two other experiments in one-dimensional systems [89, 90] beyond-mean-field behavior could be observed entering the regime of a Tonks-Giradeau gas. Finally, in a two-dimensional system the Berezinskii-Kosterlitz-Thouless crossover of a Bose gas could be realized [91].

In several other areas of physics, the experimental study of critical phenomena has a long-standing history, starting with the observation of critical opalescence at the liquid-vapor critical point [9] and reaching to high precision measurements of critical exponents. An outstanding experiment is the measurement of the critical exponent α of the heat capacity in liquid helium [15], which is a member of the 3D XY universality class. In this work an unprecedented accuracy was reached by sending the whole measurement apparatus into space to avoid the influence of gravity. The critical exponent $\alpha = -0.0127 \pm 0.0003$ from this experiment is the best known so far and can be perfectly reproduced by elaborate theories (see chapter 4.2.1). Applying the scaling relation (see chapter 2.1.1) $\nu = (2 - \alpha)/3$, a value of $\nu = 0.6709 \pm 0.0001$ can be deduced from this measurement.

With our experiment we enter for the first time the critical regime of a quantum gas in three dimensions. The system is unique, because it is free of impurities and the interactions between the particles are well known and could even be controlled. The applied method allows us to directly map out the first-order correlation function and to measure the correlation length. Using a single-atom detector to analyze the interference pattern of the extracted atoms we meet the requirement of disturbing the sample only minimally during the measurement. We are able to control the temperature of the sample precisely and to continuously monitor the correlations over time, which opens intriguing possibilities in the study of the dynamics of phase transitions.

4.3 Methods

4.3.1 Preparation of the Sample near Criticality

To prepare the ultra-cold atomic gas we load 10^9 laser cooled ^{87}Rb atoms in the $|F = 1, m_F = -1\rangle$ hyperfine ground state in the magnetic trap. The sample is evaporatively cooled and we end up with $N = 4 \times 10^6$ atoms at a temperature slightly below the critical temperature $T_c = 146\,\mathrm{nK}$. To be less sensitive to shot-to-shot fluctuations of the atom number, we chose a relatively high atom number. The trapping frequencies are $(\omega_x, \omega_y, \omega_z) = 2\pi \times (39, 7, 29)\,\mathrm{Hz}$, where z denotes the vertical axis. From these parameters one can calculate the thermal de Broglie wavelength to be $\lambda_{\mathrm{dB}} = 0.5\,\mu\mathrm{m}$, and with a peak density [92] of $n = 2.3 \times 10^{13}\,\mathrm{cm}^{-3}$ the elastic collision rate is $90\,\mathrm{s}^{-1}$.

During our measurement the atomic cloud is heated at a constant rate, and we can keep track of the sample crossing the phase transition. To leave the system in thermal equilibrium a very low heating rate is needed. We do not actively heat the sample but exploit the inherent technical heating mechanisms of our apparatus. Energy is transferred to the atomic cloud due to fluctuations of the trapping potential and due to collisions with residual background gas. Another heating mechanism is resonant stray light from the laser system. Covering the table with the laser setup we could lower the heating rate by a factor of two and end up with a rate of $4.4 \pm 0.8\,\mathrm{nK/s}$, which was determined from absorption images. This corresponds to a heating power of about $7 \times 10^{-25}\,\mathrm{W}$. Using this technique we can observe the system passing the critical regime over a time scale of seconds.

4.3.2 Output Coupling the Atoms—Theory

After preparation of the atomic sample just below the transition temperature T_c, the actual measurement starts. We output couple atoms from two distinct regions in the cloud and analyze the resulting interference pattern. How the output coupling process works and how the visibility of the interference pattern is related to the first order correlation function shall be discussed in the following sections.

We introduce the output coupling mechanism with a semi-classical model where the atoms are assumed to be localized. While this model gives an intuitive picture of the output coupling, it does not really describe the experimental situation of delocalized atoms. To account for this, we present a quantum mechanical description of the problem, and finally give a relation between the measured interference pattern and the correlation function of

the trapped cloud. Further and complementary studies of this topic can be found in [93, 94, 95, 96].

Semi-Classical Model of Output Coupling

To understand the output coupling of atoms from the trapped atomic cloud, one has to remember that the atoms are trapped magnetically. Figure 4.3 shows a level diagram for the two hyperfine ground states $5\ ^2S_{1/2}$ of ^{87}Rb. The Zeeman sublevels are split due to a weak magnetic field, and the atoms are trapped in the low-field-seeking state $|F = 1, m_F = -1\rangle$. In our experiments the atoms are output coupled by transferring them into the untrapped state $|F = 2, m_F = 0\rangle$, which is in lowest order insensitive to magnetic fields, so that the output-coupled atoms are falling downwards due to gravity. The transfer to the untrapped state is achieved by coupling the two levels with a resonant microwave frequency ω_{mw}.

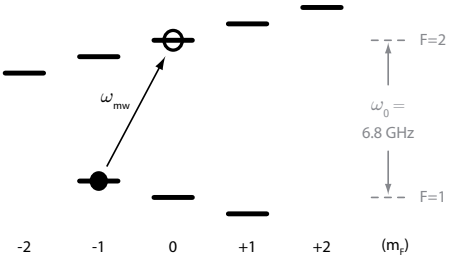

FIGURE 4.3: Zeeman splitting of the two hyperfine ground states of ^{87}Rb in a weak magnetic field. The atoms are prepared in the $|F = 1, m_F = -1\rangle$ state, which is trapped magnetically. Applying a microwave frequency with $\hbar\omega_{\mathrm{mw}} = \hbar\omega_0 - \mu|B(\mathbf{r}|)$ atoms are transferred to the untrapped state $|F = 2, m_F = 0\rangle$.

Output coupling occurs at locations where the total energy difference between the trapped and the untrapped state is equal to $\hbar\omega_{\mathrm{mw}}$. This implies that the resonance condition is space dependent, because the magnetic field, and with it the energies of the Zeeman levels, changes across the atomic cloud. Only atoms at positions where the local magnetic field $B(\mathbf{r})$ fulfills the resonance condition $\hbar\omega_{\mathrm{mw}} = \hbar\omega_0 - \mu|B(\mathbf{r})|$ are transferred into the untrapped state, where $\hbar\omega_0$ is the hyperfine splitting of the two ground states and μ is the magnetic dipole matrix element for the transition. The magnetic field of the QUIC trap increases linearly with distance from the magnetic minimum. Hence, surfaces of constant magnetic field form ellipsoidal shells

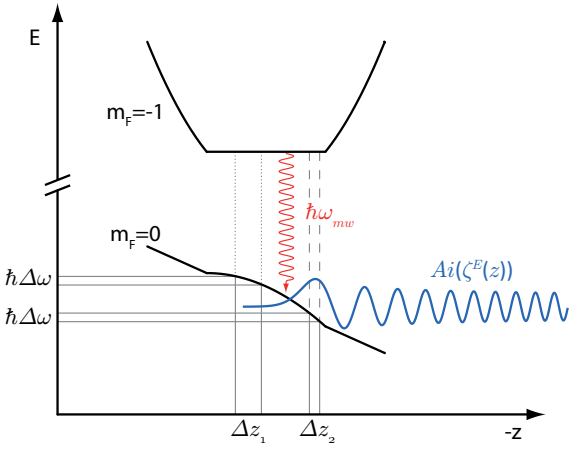

FIGURE 4.4: Energy diagram of the output-coupling mechanism. The total energy of the atoms in the trapped $|F = 1, m_F = -1\rangle$ and the untrapped $|F = 2, m_F = 0\rangle$ state are shown as black lines. The energy difference $\hbar\omega_0$ between the two hyperfine states has been subtracted from the $|F = 2, m_F = 0\rangle$ state. Both the trapping potential and the gravitational potential are affected by the mean field. A resonant microwave frequency with energy $\hbar\omega_{\mathrm{mw}}$ couples the two states locally (shown in red). The wave function for the output-coupled atoms in the gravitational potential is an Airy function $Ai(\zeta^E(z))$ (shown in blue). The grey lines point up the nonlinear dependence of the output coupling position on the photon energy: The dotted and the dashed lines represent two pairs of microwave fields with equal $\Delta\omega$. Only output coupling with pairs of microwave fields symmetric to the center of the trapping potential will result in a linear dependence.

centered around the magnetic minimum.

Without gravity, the center of the atomic cloud would be at the minimum of the magnetic trapping field. However, gravity causes a displacement of the minimum of the total potential from the magnetic field minimum. Hence the cloud is centered at a position $z_{\mathrm{sag}} = g/\omega_z^2$, where ω_z is the vertical trapping frequency and g is the acceleration due to gravity. In our experiment the gravitational sag z_{sag} is on the order of 160 µm, which is large compared to the extension of the atomic cloud. As a consequence the sections between the atomic cloud and the shells of constant magnetic field can well be approximated by horizontal planes. A resonant microwave frequency output couples atoms from one distinct plane in the cloud, and the position of the

plane can be chosen via the microwave frequency ω_{mw}.

Besides gravity and the trapping potential, the atoms also experience the mean-field potential due to the interatomic interactions. The untrapped atoms will also be exposed to this potential, until they fall out of the trapped cloud. The interactions between the output-coupled atoms in the beam can be neglected due to the low density of the atomic beam. Figure 4.4 shows an energy diagram illustrating the situation. The trapping potential of the $|F = 1, m_F = -1\rangle$ atoms is flattened due to the mean field interactions, while the gravitational potential which the untrapped $|F = 2, m_F = 0\rangle$ atoms experience becomes deformed. From the diagram it becomes clear that a certain energy of the microwave photon will output couple atoms at a defined position z. Changing the frequency of the photon changes the vertical position of output coupling accordingly. However, a change $\Delta\omega$ in frequency is proportional to a distance Δz in space only when the frequencies are centered around the minimum of the trapping potential [97] (see Figure 4.4).

The eigenfunctions of the output-coupled atoms in the linear gravitational potential are given by Airy functions $Ai(\zeta^E(z))$, with the parameter $\zeta^E(z) = (z - E/(mg))/l$ and the natural length $l = (\hbar^2/(2m^2g))^{1/3}$ [98]. The classical turning point of a particle with energy E coincides with the first inflection point of the wave function at $z_0 = E/(mg)$. The usual Airy function $Ai(\zeta^E(z))$ does not suffice to describe the falling beam of atoms, but gives only a stationary picture of the situation. To include the dynamics, a complex superposition of the Airy function $Ai(\zeta^E(z))$ with the Airy function of the second kind $Bi(\zeta^E(z))$ has to be used [93]. This is in analogy to the description of a traveling planar wave where both cosine and sine are used to describe the movement. However, in the following we restrict our discussion to the description with the real function $Ai(\zeta^E(z))$.

Quantum Mechanical Model of Output Coupling

The above discussion of output coupling uses a semi-classical approach, where the atoms are output coupled at a certain fixed position. To describe the output coupling of atoms from a trapped Bose gas into free output modes in a quantum mechanical picture, we start with the definition of the systems Hamiltonian following [94]. The model takes two possible states into account, a trapped state $|t\rangle$ (e.g. $|F = 1, m_F = -1\rangle$) with the corresponding atomic field operator $\hat{\Psi}_t$ and an untrapped (free) state $|f\rangle$ (e.g. $|F = 2, m_F = 0\rangle$) with the corresponding field operator $\hat{\Psi}_f$. During output coupling, the two states are coupled by a microwave resonant with the transition $|t\rangle \rightarrow |f\rangle$, and atoms are transferred from the trapped to the

untrapped state. The Hamiltonian of this system can be written as

$$\hat{\mathcal{H}} = \hat{\mathcal{H}}_t + \hat{\mathcal{H}}_f + \hat{\mathcal{H}}_{\text{couple}}\,, \tag{4.3}$$

where the dynamics of the trapped and the free atoms is described by $\hat{\mathcal{H}}_t$ and $\hat{\mathcal{H}}_f$, while the coupling between the two states is described by $\hat{\mathcal{H}}_{\text{couple}}$.

In this part of the description of the output coupling we focus on the coherence properties and neglect all interactions between the atoms. Accordingly, the many-body Hamiltonian $\hat{\mathcal{H}}_t$ describing the trapped atoms includes only a kinetic term and the trapping potential $V_t(\mathbf{r})$

$$\hat{\mathcal{H}}_t = \int \mathrm{d}^3\mathbf{r}\hat{\Psi}_t^\dagger(\mathbf{r})\left(-\frac{\hbar^2\nabla^2}{2m} + V_t(\mathbf{r})\right)\hat{\Psi}_t(\mathbf{r})\,, \tag{4.4}$$

and for the free atoms the dynamics are described by

$$\hat{\mathcal{H}}_f = \int \mathrm{d}^3\mathbf{r}\hat{\Psi}_f^\dagger(\mathbf{r})\left(-\frac{\hbar^2\nabla^2}{2m} + V_f(\mathbf{r})\right)\hat{\Psi}_f(\mathbf{r})\,, \tag{4.5}$$

where the potential $V_f(\mathbf{r})$ influences the propagation of the untrapped atoms. The two states are coupled by a weak microwave at frequency ω_{mw}, and the Hamiltonian $\hat{\mathcal{H}}_{\text{couple}}$ can be expressed in the rotating wave approximation as

$$\hat{\mathcal{H}}_{\text{couple}} = \hbar\int \mathrm{d}^3\mathbf{r}\lambda(\mathbf{r},t)\hat{\Psi}_f^\dagger(\mathbf{r})\hat{\Psi}_t(\mathbf{r}) + h.c.\,, \tag{4.6}$$

where $\lambda(\mathbf{r},t) = \Omega e^{-i\Delta_{\text{em}}t}$ is the coupling amplitude with the Rabi frequency Ω and the detuning $\Delta_{\text{em}} = \omega_{\text{mw}} - \tilde{\omega}_0$ of the microwave from the transition frequency $\tilde{\omega}_0$ for an atom at the trap center. The momentum transfer of the microwave photon can be neglected here.

The coupled equations of motion for the trapped and the free field operator can be found from the Hamiltonian $\hat{\mathcal{H}}$. We are interested in the evolution of the output coupled atoms which fall in the gravitational potential. It is useful to expand the field operator $\hat{\Psi}_f$ in the natural basis $\{\varphi_\mathbf{k}\}$ of the free atoms in the potential V_f, where $\mathbf{k}$ denotes the momentum state of the output-coupled atoms with energy $E_\mathbf{k} = \hbar\omega_\mathbf{k}$,

$$\hat{\Psi}_f(\mathbf{r},t) = \sum_\mathbf{k}\varphi_\mathbf{k}(\mathbf{r})\hat{b}_\mathbf{k}(t)\,. \tag{4.7}$$

Here we introduced the annihilation operator $\hat{b}_\mathbf{k}$ for a particle in the specific mode $\varphi_\mathbf{k}$. For a linear potential like the gravitational potential, the modes $\varphi_\mathbf{k}$ are again represented by Airy functions. Knowledge of the temporal evolution of all $\hat{b}_\mathbf{k}$ allows the description of the untrapped atoms. For a

system where all atoms initially (at $t = 0$) are in the trapped state, a formal solution [94] for these operators is given by

$$\hat{b}_{\mathbf{k}}(t) = -i \int_0^t \mathrm{d}t' \int \mathrm{d}^3\mathbf{r} \varphi_{\mathbf{k}}^*(\mathbf{r}) \lambda(\mathbf{r}, t') e^{-i\omega_{\mathbf{k}}(t-t')} \hat{\Psi}_t(\mathbf{r}, t') \,. \tag{4.8}$$

This expression can be evaluated using the definition for the coupling amplitude $\lambda(\mathbf{r}, t)$,

$$\hat{b}_{\mathbf{k}}(t) = -i\Omega e^{-i\omega_{\mathbf{k}}t} \underbrace{\int \mathrm{d}^3\mathbf{r} \varphi_{\mathbf{k}}^*(\mathbf{r}) \hat{\Psi}_t(\mathbf{r}, t')}_{\langle \varphi_{\mathbf{k}} | \hat{\Psi}_t \rangle} \underbrace{\int_0^t \mathrm{d}t' e^{-i(\Delta_{\mathrm{em}} - \omega_{\mathbf{k}})t'}}_{(\star)} \,, \tag{4.9}$$

where the second integration $(\star)$ will lead for long times to a decrease in spectral width and thereby to a very sharp resonance condition

$$(\star) = e^{-i\frac{1}{2}(\Delta_{\mathrm{em}} - \omega_{\mathbf{k}})t} \frac{\sin(\frac{1}{2}(\Delta_{\mathrm{em}} - \omega_{\mathbf{k}})t)}{\frac{1}{2}(\Delta_{\mathrm{em}} - \omega_{\mathbf{k}})} \underset{t\to\infty}{\longrightarrow} e^{-i\frac{1}{2}(\Delta_{\mathrm{em}} - \omega_{\mathbf{k}})t} \delta(\Delta_{\mathrm{em}} - \omega_{\mathbf{k}}) \,. \tag{4.10}$$

The spectral width is thus Fourier limited, which corresponds to an energy uncertainty due to the finite output-coupling time. For long enough times there is only one state $\varphi_{\mathbf{k}}$ in the basis of the untrapped states which has a finite probability to be populated:

$$\hat{b}_{\mathbf{k}}(t) = -i\Omega \langle \varphi_{\mathbf{k}} | \hat{\Psi}_t \rangle e^{-i(\frac{1}{2}(\Delta_{\mathrm{em}} + \omega_{\mathbf{k}})t)} \delta(\Delta_{\mathrm{em}} - \omega_{\mathbf{k}}) \,. \tag{4.11}$$

All $\hat{b}_{\mathbf{k}}$ vanish, except the one for which $\Delta_{\mathrm{em}} = \omega_{\mathbf{k}}$ is fulfilled, and the sum in Equation 4.7 collapses to a single term. The wave function of the output coupled atoms depends on the overlap $\langle \varphi_{\mathbf{k}} | \hat{\Psi}_t \rangle$ between the trapped and the free state, where the δ-function in (4.11) defines the energy of the wave function:

$$\hat{\Psi}_f(\mathbf{r}, t) = -i\Omega \varphi_{\mathbf{k}}(\mathbf{r}) \langle \varphi_{\mathbf{k}} | \hat{\Psi}_t \rangle e^{-i(\frac{1}{2}(\Delta_{\mathrm{em}} + \omega_{\mathbf{k}})t)} \,. \tag{4.12}$$

The discussion hitherto has been valid for any potential V_f for the free atoms. We now become more specific and use a one-dimensional model with the gravitational potential $V_f(r) = mgr$, for which the Airy functions $Ai(\zeta^E(z))$ are good eigenfunctions. Due to the fast oscillatory behavior of the Airy function, the overlap $\langle \varphi_{\mathbf{k}} | \hat{\Psi}_t \rangle$ is only significant in a narrow region around the classical turning point. Thus we can assign a position z to each frequency $\omega_{\mathbf{k}}$ and change the index describing the output wave function from $\mathbf{k}$ to z:

$$\hat{\Psi}_f(r, t) = -i\Omega \varphi_z(r) \langle \varphi_z | \hat{\Psi}_t \rangle e^{-i\omega_z t} \,. \tag{4.13}$$

With Equation 4.13 we found an expression for the wave function of the atoms output coupled with a single frequency. This allows us in the following to discuss the output coupling with two frequencies.

Two-frequency Output Coupling and the First-Order Correlation Function

Output coupling simultaneously with two different microwave frequencies will release two atomic wave functions with an energy difference given by the difference in energy of the microwave photons $\Delta E = \hbar(\omega_{z1} - \omega_{z2}) = \hbar\Delta\omega$. For two-frequency output coupling which is symmetric with respect to the trap center this energy difference can be directly related to a distance $\Delta z = \Delta E/(mg)$ between the classical output coupling planes. The two beams will overlap, interfere and show an interference pattern, if the regions of output coupling were phase coherent. This is perfectly true for a Bose-Einstein condensate and a corresponding absorption image is shown in Figure 4.1. The contrast of the interference pattern will be reduced or even vanish if the regions of output coupling are only partially coherent. The visibility of the interference pattern is hence a measure for the degree of coherence of the sources. Probing the visibility for different pairs of microwave frequencies means probing the coherence of the cloud as a function of distance. With this method the spatial first-order correlation function can be measured, as we will discuss in the following.

For output-coupling with two microwave frequencies ω_{z1} and ω_{z2} the field operator for the untrapped matter wave can be written using Equation (4.13) in a one dimensional model as

$$\hat{\Psi}_f(r,t) = -i\Omega\left(\varphi_{z1}(r)\langle\varphi_{z1}|\hat{\Psi}_t\rangle e^{-i\omega_{z1}t} + \varphi_{z2}(r)\langle\varphi_{z2}|\hat{\Psi}_t\rangle e^{-i\omega_{z2}t}\right), \quad (4.14)$$

where the indices $z1, z2$ correspond to the vertical positions of classical planes of output-coupling.

The resulting interference pattern as a function of position r (where the center of the cloud is at $r = 0$) and time t is characterized by the density operator $\left\langle\hat{\Psi}_f^\dagger(r,t)\hat{\Psi}_f(r,t)\right\rangle$, which can be interpreted as the time dependent flux of atoms [93]

$$\left\langle\hat{\Psi}_f^\dagger(r,t)\hat{\Psi}_f(r,t)\right\rangle \propto \frac{1}{\sqrt{|r|}}\left[1 + V(\Delta z)\cos\left(\sqrt{\frac{2}{g|r|}}(\omega_{z1} - \omega_{z2})|r| + (\omega_{z1} - \omega_{z2})t\right)\right], \quad (4.15)$$

where the modulation of the flux corresponds to the visibility $V(\Delta z)$ of the interference pattern, which is a function of the classical slit distance $\Delta z = |z1 - z2|$. Depending on the coherence of the output-coupling regions, the visibility $V(\Delta z)$ can vary between 0 and 1. Equation (4.15) shows that the interference pattern is not equidistant in space, but that the wavelength of the interference pattern becomes longer for higher r, because the atoms are accelerated due to gravity g (see Figure 4.1).

We are interested in the interference pattern at the fixed position of the detector r_0. The flux of the atoms passing our detector is modulated in time at the difference frequency $\Delta\omega$ of the output coupling frequencies. Evaluating the density operator $\left\langle \hat{\Psi}_f^\dagger(r_0,t)\hat{\Psi}_f(r_0,t)\right\rangle$ at a fixed position one finds a simplified form of equation (4.15)

$$\left\langle \hat{\Psi}_f^\dagger(r_0,t)\hat{\Psi}_f(r_0,t)\right\rangle \propto \Big(1+V(\Delta z)\cos(\Delta\omega t+\phi)\Big)\,, \tag{4.16}$$

with a certain phase ϕ.

The relation between the first-order correlation function of the trapped gas $\left\langle \hat{\Psi}_t^\dagger(r_1)\hat{\Psi}_t(r_2)\right\rangle$ and the measured visibility $V(\Delta z)$ shall be discussed in the following. The detailed calculation is presented in Appendix C, here we show only the main results. Using (4.14), we show that the visibility is directly related to the first order correlation function of the trapped gas through

$$V(\Delta z) = A\int \varphi_{z1}(r_1)\varphi_{z2}(r_2)\left\langle \hat{\Psi}_t^\dagger(r_1)\hat{\Psi}_t(r_2)\right\rangle \mathrm{d}r_1\mathrm{d}r_2\,, \tag{4.17}$$

with the normalization constant A.

Restricting the discussion for the moment to a purely Gaussian correlation function, Equation 4.17 can be evaluated:

$$V(\Delta z) = A\int e^{-\pi\frac{(\tilde{r}-\Delta z)^2}{\lambda_{\mathrm{dB}}}} \underbrace{\int \varphi_{-\tilde{r}/2}(R)\varphi_{\tilde{r}/2}(R)e^{-\frac{R^2}{2R_{\mathrm{th}}^2}}\mathrm{d}R\,\mathrm{d}\tilde{r}}_{(\star)}\,, \tag{4.18}$$

with the thermal de Broglie wavelength λ_{dB} and the radius of a thermal trapped gas R_{th}.

Equation (4.18) is a convolution of the Gaussian decay of the correlation function with the integral $(\star)$. The wave functions $\varphi_{\pm\tilde{r}/2}(R)$ are Airy functions which are orthogonal to each other. Accordingly, the integration $(\star)$ will result in a sharp peak with a width depending on R_{th}: the larger R_{th} is, the smaller will the width of the peak be. For parameters corresponding to our experiment we numerically calculate the result of $(\star)$ as a function of $\tilde{r}$, as well as its convolution with the Gaussian decay. The results are plotted in Figure 4.5. We conclude that in our parameter range, the visibility as a function of distance Δz reproduces the first-order correlation function of the trapped gas very well. This result would change for very small trapped samples, where the integral $(\star)$ shows a much broader peak.

Following [49] the correlation function of the Bose gas $\left\langle \hat{\Psi}_t^\dagger(r_1)\hat{\Psi}_t(r_2)\right\rangle$ in local density approximation can be written as a sum $\sum_k 1/k^{3/2}\Gamma^k(R)\gamma^{1/k}(r)$

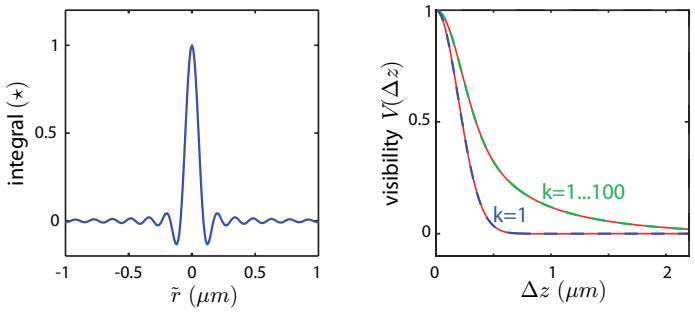

FIGURE 4.5: Left: Numerical evaluation of the integral ($\star$) in Equation (4.18) for the parameters of our experiment. The integration of the product of two Airy functions over a finite interval given by the cloud size results in a narrow, peaked function. Right: The visibility $V(\Delta z)$ as a function of distance Δz according to Equation (4.18) is shown as blue dashed line for our parameters, including only $k = 1$. A comparison to the visibility expected from the correlation function $\langle \hat{\Psi}_t^\dagger(\Delta z)\hat{\Psi}_t(0)\rangle$ is shown in red (again only in lowest order, $k = 1$), and good agreement is found. The same analysis was carried out for the first 100 terms of the correlation function at a temperature $T = 1.03T_c$. Again there is very good agreement between the original correlation function (red) and the correlation function according to the convolution in Equation 4.18 (green).

(see Equation 2.21), where $\Gamma(R)$ depends only on the center of mass coordinate $R = (r_1 + r_2)/2$ and $\gamma(r)$ depends only on the relative coordinate $r = r_1 - r_2$. We restricted ourselves to the Gaussian decay of the correlation function, which is the first term of the sum, having the fastest decay. The above calculation can be equivalently carried out for each summand k, and summing over all contributions the full result can be obtained. With rising k, the peak resulting from integration ($\star$) will become broader, but at the same time $\gamma(r)^{1/k}$ shows a less pronounced decay. As a result the convolution of $\gamma(r)^{1/k}$ with ($\star$) will still reproduce the k-th contribution to the correlation function. In Figure 4.5 the result for a correlation function according to Equation 2.21 including the first 100 terms is shown (green) in comparison to the original correlation function (red). We conclude that for our parameters, the visibility $V(\Delta z)$ is a good measure for the first order correlation function.

However, one has to keep in mind that this model makes two simplifications: it is a one-dimensional model and it takes no interactions between the

atoms into account. A more detailed model would go beyond the scope of this thesis, but we are convinced that both simplifications have only minor influence on our results.

4.3.3 Output Coupling the Atoms—Experiment

Output Coupling with Microwave Frequencies

In the experiment output coupling of the atoms is achieved by shining in two well-defined microwave frequencies (see Figure 4.1) at about 6.8 GHz [99]. To achieve a maximal visibility of the atomic interference pattern it is important to balance the power of the two frequencies. We split the output signal of a microwave frequency generator into two signals and mix each of them with a different radio frequency. The resulting mixing products are combined and include the sum and the difference frequencies of the initial frequencies. With a narrow bandpass filter we select only the sum frequencies, which we amplify and feed into a helical microwave antenna inside the vacuum chamber. The impedance is matched with a stub tuner.

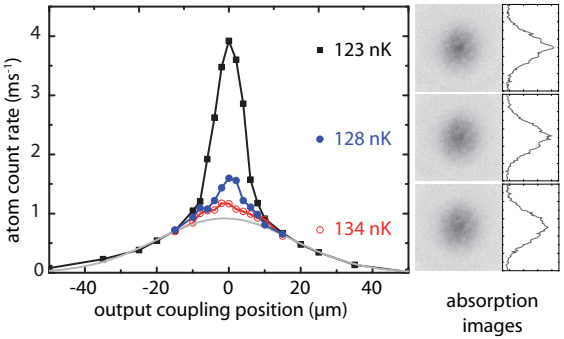

FIGURE 4.6: Analysis of the density distribution of the trapped ultracold atom gas by output coupling at different vertical positions relative to the center of the cloud and measuring the resulting atom count rate with the single-atom detector. The center of the cloud can easily be determined with this method. The profiles for three different temperatures around T_c are shown in comparison with the absorption images. The high sensitivity of the cavity detector to quantum degenerate atoms allows for precise observation of the onset of Bose-Einstein condensation. Image taken from [66].

The relative phase of the two microwave frequencies will determine the phase of the atomic interference pattern [97]. In order to have the same

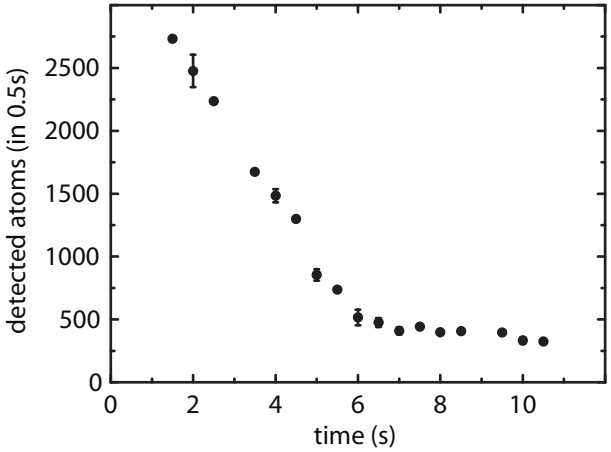

FIGURE 4.7: Crossing the phase transition. While the trapped cloud is heated with a low heating rate, the flux of atoms on our single atom counter is monitored. When the system crosses the phase transition a kink appears. Atoms were output coupled from the center of the cloud.

starting phase of the interference pattern in each experimental run, we stabilize all frequency generators on a 10 MHz GPS reference signal and control the starting phase of the two radio frequencies.

As discussed in Section 4.3.2 the planes of output coupling have to be chosen symmetric with respect to the center of the cloud. This center can be found by scanning a single microwave frequency and detecting the flux of atoms on our single-atom detector. The result is shown in Figure 4.6. Having determined the center of the cloud, the flux of atoms as a function of temperature can be used to check that we prepare the sample slightly below the critical temperature. The flux of atoms output coupled from the center is clearly increased if there is a small condensate fraction present (see Figure 4.6 and 4.7).

The microwave power determines the number of output-coupled atoms. A high flux of atoms improves the statistics of our measurement but has two drawbacks. First, output coupling with stronger microwave power reduces the atom number in the sample during the measurement and induces a systematic error of our results. Second, a too high flux saturates the single atom detector, which results in a reduced visibility of the measured interference pattern. To minimize both effects and still collect enough data we

chose a count rate of $800\,\mathrm{s}^{-1}$. At this count rate we still detect an interference pattern with 100 % visibility for a frequency difference of 1 kHz of the output coupling frequencies, whereas the visibility decreases linearly to 96 % for a count rate of $1600\,\mathrm{s}^{-1}$. Taking the detection efficiency of our detector for thermal atoms of about 1 % into account, we output couple with a rate of approximately $8 \times 10^4\,\mathrm{s}^{-1}$ from the sample.

The Detector as a Momentum Filter

The first-order correlation function is a measure for correlations between two points in space. In our experiment we do not output couple from two points but from two planes. However, due to the geometry of our setup which acts as a momentum filter, we directly measure the two-point correlation function.

With a typical source size of $2R_{\mathrm{th}} \approx 60\,\mu\mathrm{m}$, a distance of 36 mm between source and detector and an active detector area of about $(35 \times 150)\,\mu\mathrm{m}^2$ [66] the geometry acts mainly as a momentum filter in the transverse directions. This effect has been studied in detail in [65], including a Monte Carlo simulation. The most important result, shown in Figure 4.8, shows that we detect nearly exclusively atoms which have zero transverse momenta in the trap.

The momentum filter has to be considered when evaluating the correlation function. In the usual definition of the first-order correlation function one integrates over all momenta (p_x, p_y, p_z) and evaluates the correlation function as a function of Δz for $(x = y = 0)$, which yields (see Section 2.1.3)

$$\langle \hat{\Psi}^\dagger(z)\hat{\Psi}(z')\rangle = \frac{1}{\lambda_{\mathrm{dB}}^3}\sum_{s=1}^{\infty}\frac{1}{s^{3/2}}e^{s\mu/k_{\mathrm{B}}T}e^{-\frac{1}{s}\pi\frac{\Delta z^2}{\lambda_{\mathrm{dB}}^2}}\,. \tag{4.19}$$

For the evaluation of our measurement the calculation has to be adapted to the experimental situation. We output couple from extended planes but use a momentum filter. Instead of setting two spatial coordinates (x, y) to zero and integrating over all momenta, we now have to set two momentum components to zero $(p_x = p_y = 0)$ and to integrate over the spatial dimensions (x, y) and over the longitudinal momentum component p_z.

We put the origin of our coordinate system to the center of the cloud and assume symmetric output coupling: $z = -z'$, and $\Delta z = z - z'$. Furthermore, we set $(p_x = p_y = 0)$ and introduce new, better suited coordinates ($\bar{x} = \frac{x+x'}{2}$, $\bar{y} = \frac{y+y'}{2}$ and $\bar{z} = \frac{z+z'}{2} = 0$). Following the reasoning in Section 2.1.3 and exploiting the symmetry of the Wigner function in generalized coordinates $(\mathbf{r}, \mathbf{p})$ for our system, we can write the first order correlation

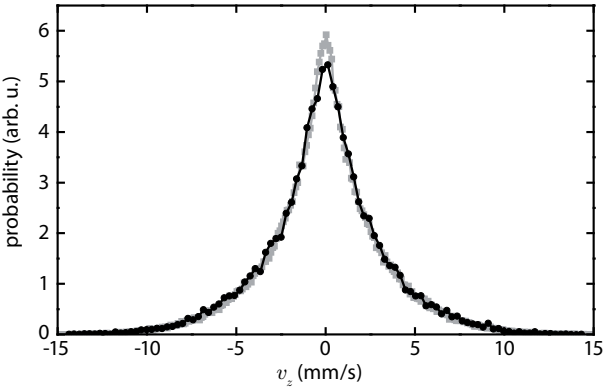

FIGURE 4.8: Probability distribution for the vertical velocity of atoms output coupled from a plane at the center of the cloud. Shown as black circles is the distribution for atoms with an initial momentum distribution corresponding to a Bose gas 0.2% above the critical temperature, filtered by our setup. This has to be compared to the situation where the initial distribution has no transverse momenta, $p_x, p_y = 0$ (shown as grey squares). Simulation and image adopted from [65].

function

$$\langle\hat{\Psi}^\dagger(z)\hat{\Psi}(z')\rangle = \frac{1}{(2\pi\hbar)^3}\int\!\!\int\!\!\int_{-\infty}^{\infty} \mathrm{d}\bar{x}\mathrm{d}\bar{y}\mathrm{d}p_z e^{-i\mathbf{p}(\mathbf{r}-\mathbf{r}')/\hbar}\frac{1}{e^{(\frac{\mathbf{p}^2}{2m}+V(\frac{\mathbf{r}+\mathbf{r}'}{2})-\mu)/k_\mathrm{B}T}-1}. \tag{4.20}$$

More explicitly and writing the fraction as a sum one finds

$$\begin{aligned} &= \tfrac{1}{(2\pi\hbar)^3}\sum_{s=1}^{\infty} e^{s\frac{\mu}{k_\mathrm{B}T}}\int\!\!\int\!\!\int_{-\infty}^{\infty}\mathrm{d}\bar{x}\mathrm{d}\bar{y}\mathrm{d}p_z e^{-\frac{i}{\hbar}\left(p_x(x-x')+p_y(y-y')+p_z(z-z')\right)}\cdot \\ &\cdot e^{-\frac{p_x^2+p_y^2+p_z^2}{2mk_\mathrm{B}T}} e^{-s\frac{m}{2k_\mathrm{B}T}\left(\omega_x^2\bar{x}^2+\omega_y^2\bar{y}^2+\omega_z^2\bar{z}^2\right)}, \end{aligned} \tag{4.21}$$

where we now put in ($p_x = p_y = 0$, $\Delta z = z - z'$) and carry out the integration over p_z

$$= \frac{1}{(2\pi\hbar)^3}\sum_{s=1}^{\infty} e^{s\frac{\mu}{k_B T}}\sqrt{\frac{2\pi m k_\mathrm{B}T}{s}} e^{-\frac{\pi}{s}\frac{\Delta z^2}{\lambda_\mathrm{dB}^2}}\int\!\!\int_{-\infty}^{\infty}\mathrm{d}\bar{x}\mathrm{d}\bar{y} e^{-s\frac{m\omega_x^2\bar{x}^2}{2k_\mathrm{B}T}} e^{-s\frac{m\omega_y^2\bar{y}^2}{2k_\mathrm{B}T}}. \tag{4.22}$$

Evaluating the residual integral finally gives

$$\langle\hat{\Psi}^\dagger(z)\hat{\Psi}(z')\rangle \propto \frac{1}{\lambda_{\mathrm{dB}}^3}\sum_{s=1}^{\infty}\frac{1}{s^{3/2}}e^{s\mu/k_{\mathrm{B}}T}e^{-\frac{1}{s}\pi\frac{\Delta z^2}{\lambda_{\mathrm{dB}}^2}}, \tag{4.23}$$

which is proportional to the expression for the usual correlation function (4.19). However, we consider only the normalized correlation function $g^{(1)}(\Delta z)$. The experimental situation can be mapped onto the well known first-order correlation function in the usual definition. Again we can approximate this for large Δz (see Section 2.1.3 and Appendix B) and find the asymptotic form

$$\langle\hat{\Psi}^\dagger(z)\hat{\Psi}(z')\rangle \to \frac{1}{\Delta z}e^{-\Delta z/\xi}, \tag{4.24}$$

with the correlation length $\xi = \sqrt{\frac{\hbar^2}{2m|\mu|}}$.

4.3.4 Data Evaluation

We took data during a total time interval of 2.5 s for 8 different separations Δz of the output coupling regions. Each repetition of the experiment results in a trace which covers 1 s and the total raw data consists of more than 350 traces with single atom arrival times. The first hours of data had to be discarded because the atom number drifted and the system had to be readjusted. That is why there is a break in the data. The data for different separations Δz were taken in random order to avoid systematic errors due to drifts of the apparatus.

The raw data is evaluated in several steps as shown in Figure 4.9. Each trace is cut into segments of length Δt (point (1) in Figure 4.9), before the visibility of the interference pattern is extracted from each segment in a Fourier transformation. This is done for all separations Δz and we end up with data sets $V(\Delta z)$ for each time interval corresponding to a correlation function $g^{(1)}(\Delta z)$ for each temperature interval ΔT (see (3) in Figure 4.9). In a next step each of these data sets is fit for $\Delta z > \lambda_{\mathrm{dB}}$ with the asymptotic form of the correlation function (4.24), which gives the correlation length ξ for each temperature interval (see (4) in Figure 4.9). The final step is to plot the correlation length as a function of reduced temperature $t = \frac{T-T_{\mathrm{c}}}{T_{\mathrm{c}}}$ and to fit this dependence with a power law $\xi(t) \propto t^{-\nu}$, yielding the critical exponent ν (see (5) and (6) in Figure 4.9).

Determining the Visibility

To extract the visibility of the interference pattern from a data set containing single-atom arrival times we apply a simple form of a Fourier transformation.

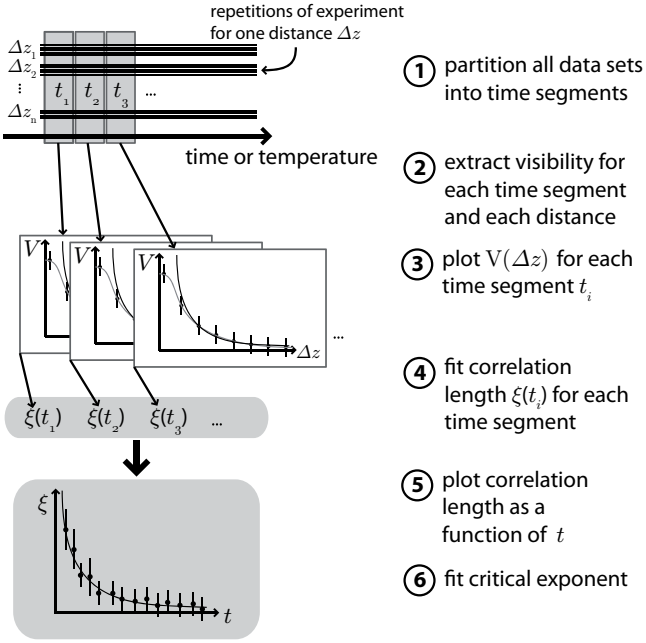

FIGURE 4.9: Evaluation of the data. The raw data consists of several repetitions of the experiment for each separation Δz of the output coupling planes. Each trace is cut into time intervals of length Δt, which correspond to temperature intervals ΔT. For each interval the visibility is extracted. This results in a number of data sets $V(\Delta z)$ corresponding to correlation functions for each temperature interval. A fit of the correlation length for each data set gives the correlation length as a function of temperature, from which the critical exponent ν can be extracted.

We are only interested in the amplitude of the frequency component at which the atomic flux is modulated, which corresponds to the difference frequency $\Delta\omega$ of the two output coupling frequencies (see Equation 4.16). The phase ϕ_0 of the interference pattern relative to the timing of the experimental cycle is dependent on Δz but well known, because we control the phase of the microwave frequencies [97]. We sum up all N atom arrival times t_a and get a complex number s

$$s = \frac{2}{N} \sum_{a=1}^{N} e^{i\Delta\omega t_a} , \tag{4.25}$$

from which we extract amplitude A_s and phase ϕ_s. The complex number s can be interpreted as a vector in the complex plane and the visibility of the interference pattern is given by the projection of s onto the phase ϕ_0

$$V = A_s \cos(\phi_s - \phi_0)\,. \tag{4.26}$$

This method is visualized in Figure 4.10.

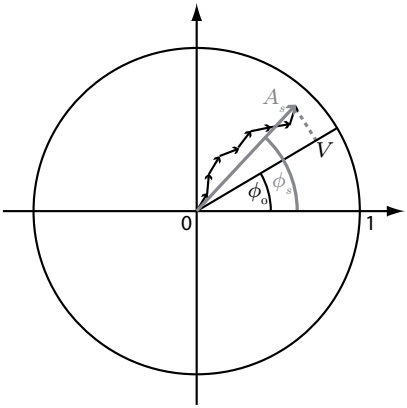

FIGURE 4.10: Extracting the visibility V from N single atom-arrival times t_a. Each small black arrow of length $2/N$ corresponds to one event, where the angle depicts the phase given by $e^{i\Delta\omega t_a}$. The resulting grey arrow with amplitude A_s and phase ϕ_s is projected onto the expected phase ϕ_0 which yields the visibility V.

We checked that the visibility of the interference pattern emerging from a pure BEC is 100% within the error bars of 2 % for separations of the output coupling planes $\Delta z < 3\,\mu\text{m}$. However, the visibility decreases due to several technical reasons for larger separations Δz (see [65] and Section 5).

4.4 Results and Discussion

4.4.1 Long-Range Correlations and the Critical Exponent

Figure 4.11 shows the measured visibility as a function of separation Δz for three different temperatures very close to T_c. The strong temperature dependence of the correlation function is directly visible. The visibility decays on a much longer length scale than predicted by the thermal de Broglie wavelength λ_{dB} (shown in grey). As the temperature approaches the

critical point, the visibility curves become more long ranged and similarly the correlation length ξ increases. The observation of long-range correlations shows how the size of the correlated fluctuating regions strongly increases as the temperature is varied only minimally in the vicinity of the phase transition. These long-ranged correlations of the fluctuating regions herald the onset of the ordered phase on the other side of the transition.

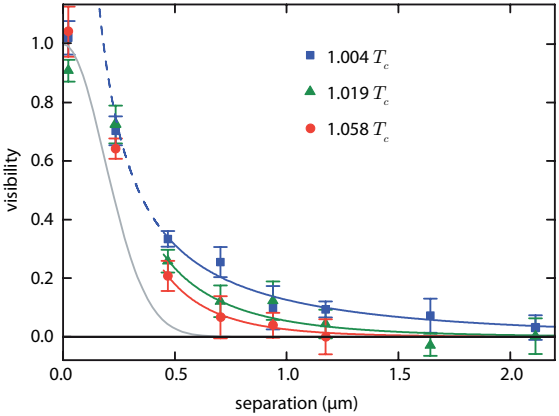

FIGURE 4.11: Spatial correlation function of a trapped Bose gas close to the critical temperature. Shown is the visibility of the matter wave interference pattern originating from two regions separated by Δz in an atomic cloud just above the transition temperature. The grey line is a Gaussian with a width given by the thermal de Broglie wavelength λ_{dB} which changes only marginally for the temperature range considered here. The experimental data show phase correlations extending far beyond the scale set by λ_{dB}. The solid lines are a fit proportional to $\frac{1}{\Delta z} e^{-\Delta z/\xi}$ for $\Delta z > \lambda_{\mathrm{dB}}$. Each data point is the mean of, on average, 12 measurements; the error-bars are $\pm$ standard deviation.

The error bars of the data points in Figure 4.11 display the standard deviation of the mean of, on average, 12 measurements. In each experimental run the temperature of the sample will be slightly different due to fluctuations during the preparation of the atoms. This effect, together with the shot noise on the data, leads to the given error bars.

For each time (or temperature) interval we fit the visibility $V(\Delta z)$ with the asymptotic form of the correlation function $g^{(1)}(\Delta z) \propto \frac{1}{\Delta z} e^{-\Delta z/\xi}$, which yields the correlation length ξ. The asymptotic form is valid for large Δz. However, as we have access only to a finite range of distances, we need

an estimation of the error we make when fitting to data points with small Δz. We checked with a theoretical model that the error in the correlation length is less than 2 % when the asymptotic form is fitted to data points with $\Delta z > \lambda_{\mathrm{dB}}$. This error increases strongly if data points for shorter separations Δz are included (e.g. more than 10 % error in ξ for a fit to data points with $\Delta z > 0.5\lambda_{\mathrm{dB}}$).

The measured correlation length as a function of temperature is shown in Figure 4.12. It is obvious that the correlation length ξ diverges when the system reaches the critical temperature. The size of the error bars for the correlation length increases when the temperature approaches the critical point. In this regime small shot-to-shot fluctuations in the temperature of the cloud lead to big fluctuations in the fit of the correlation length. The error in determining the temperature of a data point is hence included in the error bar of the correlation length.

Generally, an algebraic decay of the correlation length as a function of temperature is predicted. We fit the data with the power law $\xi \propto \left(\frac{|T-T_{\mathrm{c}}|}{T_{\mathrm{c}}}\right)^{-\nu}$, leaving both the critical exponent ν and the critical temperature T_{c} as a free fit parameter. This makes our analysis independent of an exact calibration of both temperature and heating rate, provided that the heating rate is constant: a heating rate scaled by a factor would leave the exponent of the power law unaffected.

A parameter which has influence on our result is the temporal offset t_0 of the analyzing time-bin window. Depending on the exact starting point t_0 of our evaluation the fit for the critical exponent gives a certain spread of values. To become independent of this offset t_0, we let the evaluation for all correlation lengths run for 70 different temporal offsets $0 < t_0 < \Delta t$, and fit the the critical exponent to the whole data set, containing all results for ξ. The result is the same as for first fitting the critical exponent to the data sets of the individual temporal offsets and taking the average afterwards [75]. In both cases the error $\tilde{\sigma}_\nu$ of the resulting critical exponent will be underestimated, because the data sets are not independent. The correct estimate for the error is given by the mean value σ_ν of the reduced χ^2 error resulting from the individual fits.

It is important that the length of the time (or temperature) interval Δt has been chosen optimally in the beginning of the data evaluation. Our data set consists only of a finite number of atom arrival times. Cutting the raw data into too short intervals will lead to a strong influence of shot noise on the determination of the visibility. On the other hand, the determination of a precise value of the critical exponent depends on the temperature resolution of the measurement. Long time intervals imply integrating over large

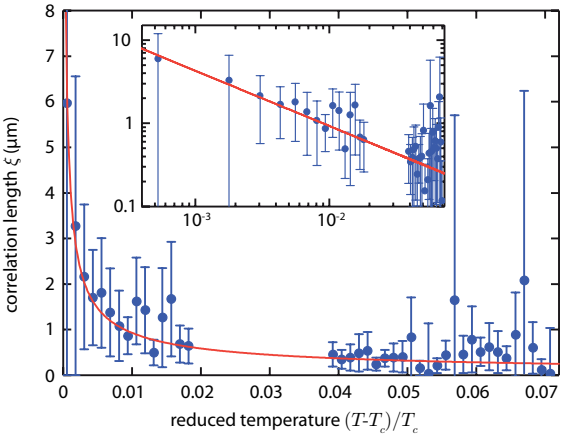

FIGURE 4.12: Divergence of the correlation length ξ as a function of temperature. The red line is a fit of the power law $\xi \propto \left(\frac{|T-T_c|}{T_c}\right)^{-\nu}$ to the data with ν and T_c as free parameters. Plotted is one data set for a specific temporal offset t_0. The error bars are $\pm$standard deviation, according to fits of the correlation length. They also reflect the scattering between different data sets. Inset: Double logarithmic plot of the same data.

temperature intervals, which decreases the temperature resolution.

The time-bin length was chosen to optimize between the shot-noise limited determination of the visibility and sufficiently good temperature resolution. In figure 4.13 we show the dependence of both the value ν of the critical exponent and of the error $\tilde{\sigma}_\nu$ on the segment size Δt of the time-bin window. A pronounced minimum in the error $\tilde{\sigma}_\nu$ of the critical exponent indicates the optimal time bin length of approximately 70 ms. For shorter segment sizes the error in ν increases due to shot noise of the data.

We choose a segment size of $\Delta t = 72$ ms and find a corresponding value of $\nu = 0.67$ for the critical exponent. Instead of choosing the minimum in the error one can also average the results for the critical exponents for a certain range of segment sizes where the error is smaller than a threshold value (e.g. $\tilde{\sigma}_\nu < 0.05$ gives $62\,\text{ms} < \Delta t < 79\,\text{ms}$), which again gives a value of $\nu = 0.67$. That this value coincides exactly with the theoretical value is coincidence, which becomes clear when looking at the error bar. We give the reduced χ^2 error σ_ν, averaged over the individual fits and finally find for the critical

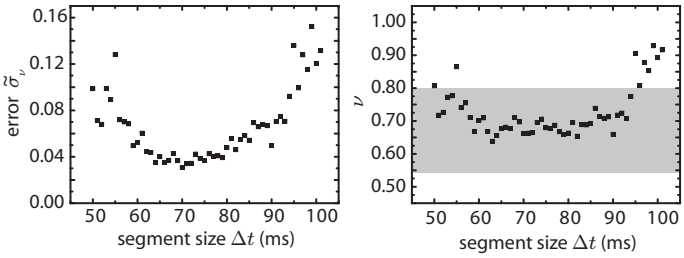

FIGURE 4.13: Determination of the optimum segment size Δt. A short segment size is preferable in order to have a good temperature resolution. On the other hand, shot noise increases the error of the result. We choose a segment size of Δt=72 ms and find the corresponding critical exponent $\nu = 0.67 \pm 0.13$. Shown in the left graph is the underestimated error $\tilde{\sigma}_\nu$ of a fit to dependent data sets, whereas our estimated error $\sigma_\nu = \pm 0.13$ is the averaged error of individual fits to independent data (shown as a grey bar in the right graph).

exponent $\nu = 0.67 \pm 0.13$.

Using the given heating rate, the segment length of $\Delta t = 72$ ms corresponds to a temperature resolution of $\Delta T = 0.3$ nK, which yields a relative temperature resolution of $\Delta T/T_c = 0.002$. The error in the determination of the critical temperature T_c is calculated in the same way as the error for the critical exponent and we find $\sigma_{T_c} = 0.08$ nK.

4.4.2 Discussion

Finite Measurement Time

Our measurement naturally takes place in a finite time, which poses the questions how well the system is in thermal equilibrium and if the system comes into the regime of critical slowing down.

In general a system with changing temperature is never in thermal equilibrium, so we have to ask how far the system is out of thermal equilibrium. A gas relaxes from a non-equilibrium situation to its equilibrium velocity distribution by collisions of the particles. A Bose gas far off equilibrium needs on the order of seven collisions per particle to relax [100]. The gas in our experiment has been held for several seconds in the trap before the actual measurement starts, so it will be in a situation close to thermal equilibrium. Only the constant heating rate of 4.4 nK/s puts energy into the system and

drives it away from equilibrium. With the collision rate of $90\,s^{-1}$ we assume the system close to equilibrium at any time.

However, the above mentioned argumentation is only valid for systems away from the critical point. When approaching the phase transition the timescale on which the system relaxes into equilibrium diverges, which leads to the phenomenon of critical slowing down [44]. In a system quenched (forced) over the phase transition, the correlated regions become increasingly larger until the system has no time to equilibrate anymore and the fluctuations are "frozen out" [38]. To estimate the relevant time scale the system needs to relax when the fluctuating regions have the size of the correlations length ξ, we have to divide this correlation length by the characteristic velocity at which fluctuations propagate. This velocity is the speed of sound, which in our situation is on the order of $v_s \approx 1\,mm/s$. This yields for the largest measured correlation lengths a correlation time $\tau \approx 10\,ms$, which is short compared to the segment size. Thus we do not expect to be in a regime where critical slowing down is important.

Heat Capacity

Our evaluation relies on the assumption of a constant heat rate. However, the heat capacity of the gas also experiences a divergence at the critical point, described by the critical exponent α which is on the order of -0.01 for the 3D XY universality class. The small value of this critical exponent implies that the divergence is very narrow and does not significantly affect the temperature region in which our measurement takes place. We estimate the resulting error in the critical exponent ν to be less than 0.01.

Finite Size

In general, a sharp, pure divergence exists only in the thermodynamic limes. Finite-size effects are expected when the correlation length is large [34] and will result in a rounding and shifting of the critical singularities. This has been observed in liquid helium confined in micro structures [35]. Finite-size effects may lead to a slight underestimation of ν for our conditions. Moreover, the harmonic confining potential introduces a spatially varying density. The phase transition takes place at the center of the trap and non-perturbative fluctuations are thus expected within a finite radius R [83]. Using the Ginzburg criterion as given in [45] we find $R \approx 10\,\mu m$, whereas the rms size of the thermal cloud is $58\,\mu m$. The longest distance we probe in our experiment is $2\,\mu m$ which is well below this radius R.

Improvements

It would be desirable to increase the accuracy of this measurement. The high temperature resolution could be achieved because the heating rate was minimized and because the method of measuring the coherence is very sensitive. In addition the robust construction of the apparatus is an important prerequisite. However, an improvement could certainly be achieved with an even lower heating rate. Residual stray light has to be eliminated, better vacuum conditions could be achieved and the fluctuations of the trapping potential could be further damped. A part of the inaccuracies stems probably from residual oscillations in the position of the trapped cloud which lead to small oscillations in the visibility. We tried to filter these oscillations during the data evaluation but could not achieve a more accurate value for ν. The reason for these oscillations is not obvious, but could be related to transport and preparation of our sample. Better statistics would certainly also help, but during longer measurements the whole apparatus will show bigger drifts.

4.5 Summary

In this experiment we observed long-range critical correlations in a trapped interacting Bose gas, and measured the critical exponent for the correlation length of this system. We applied a double-slit interference experiment and exploited the single-atom detection capability to have continuous access to the first-order correlation function of the trapped gas. The measured value of $\nu = 0.67 \pm 0.13$ for the critical exponent is in good agreement with the predictions from renormalization group theory.

The observed phase transition lies in the 3D XY universality class which also includes the λ-transition of liquid helium. One expects to observe the same critical exponents despite the fact that the density differs by ten orders of magnitude. In the measurements with liquid helium the critical exponent of the specific heat α has been measured with great accuracy in a spaceborne experiment [15]. Through the scaling relation $\alpha = 2 - 3\nu$ the value of the critical exponent $\nu \simeq 0.67$ can be found. Alternatively, the exponent $\zeta \simeq 0.67$ (which is related to the superfluid density $\rho_s = |\Psi|^2$ instead of the order parameter Ψ) can be measured directly in second sound experiments in liquid helium [101, 102]. Due to an argument by Josephson [103] it is believed that $\nu = \zeta$, however, a measurement of ν directly through the density matrix has so far been impossible with helium.

The technique of counting single atoms extracted from a trapped Bose gas is only minimally invasive and allows the continuous, time-resolved study of a

quantum system over seconds. It opens intriguing possibilities to study also dynamic phase transitions where the system is quenched across the critical point. The method is not limited to the study of the classical normal to superfluid transition. Implementing an optical lattice, a system undergoing a quantum phase transition from a superfluid to an insulating state [22] could be investigated.

5 Observing the Formation of Long-Range Order

We have experimentally investigated the formation of off-diagonal long-range order in a gas of ultracold atoms. A magnetically trapped atomic cloud prepared in a highly non-equilibrium state thermalizes and thereby crosses the Bose-Einstein condensation phase transition. The evolution of phase coherence between different regions of the sample is constantly monitored and information on the spatial first-order correlation function is obtained. We observe the growth of the spatial coherence and the formation of long-range order in real time and compare it to the growth of the atomic density. Moreover, we study the evolution of the momentum distribution during the non-equilibrium formation of the condensate.

This chapter has been published in [100]: S. Ritter, A. Öttl, T. Donner, T. Bourdel, M. Köhl and T. Esslinger, *Observing the formation of long-ranged order during Bose-Einstein condensation*, Phys. Rev. Lett. 98, 094002 (2007).

5.1 Introduction

When a gas of atoms is undergoing Bose-Einstein condensation a macroscopic number of particles starts to occupy the same quantum mechanical state—it seems like the randomly colliding atoms are suddenly forced into a lock-step motion. The understanding of this process in which phase coherence spreads over the whole gaseous cloud has intrigued physicists long before Bose-Einstein condensation has been demonstrated [104, 105]. In particular, the question when the characteristic long-range phase coherence is established is the key point for understanding the condensation process. The trajectory into the state of a Bose-Einstein condensate [104, 105, 106, 107] is much more intricate than its equilibrium properties.

The transition to a superfluid or a superconducting quantum phase is a remarkable process in which the properties of the system undergo a fundamental change. The conceptual link between quantum phases in various systems is the off-diagonal long-range order in the density matrix which describes phase correlations over macroscopic distances [18, 19]. The first-order spatial correlation function $\rho^{(1)}(r,r') = \langle\hat{\Psi}^\dagger(r)\hat{\Psi}(r')\rangle$ [49] quantifies the characteristic length scale over which phase correlations exist. Here $\hat{\Psi}$ ($\hat{\Psi}^\dagger$) denotes the annihilation (creation) operator of the atomic fields. To experimentally study how long-range order is established in space and time, real-time access to this process is required. Yet, due to the short relaxation times and the strong coupling to the environment this seems troublesome in condensed matter samples, such as liquid helium or superconducting materials.

In a trapped atomic Bose gas the situation is distinctly different. It forms an almost closed system with negligible coupling to the environment and the relaxation time scales are experimentally accessible. Previous experimental studies of the Bose-Einstein condensate formation have focused on the increasing particle density [3, 4, 6] and the influence of excitations on the momentum spread in elongated traps [5, 6]. The off-diagonal long-range order has been studied only at thermal equilibrium [20].

We present an experimental study of the evolution of off-diagonal long-range order during the formation of a Bose-Einstein condensate out of a non-equilibrium situation. We start from a Bose gas above the phase transition temperature and suddenly quench the gas into a strongly non-equilibrium state [3, 4, 5, 6]. Subsequently, the gas can be regarded as a closed system which evolves into a Bose-Einstein condensed phase. The off-diagonal long-range order is measured by studying the interference pattern of atomic matter waves originating from two different locations in the atom trap [20]. The visibility of this interference pattern measures the phase coherence be-

tween the two regions and its temporal evolution uncovers the formation of long-range order. We continuously monitor the interference pattern during the formation using a single atom counter with high temporal resolution [108]. Varying the vertical distance Δz between the two locations allows us to experimentally map out the evolution of the phase coherence in the trapped Bose gas.

In the theoretical investigation of the non-equilibrium formation of a Bose-Einstein condensate one distinguishes qualitatively between a kinetic evolution and a coherent evolution [104, 109, 110, 106]. During the kinetic stage of the evolution, the occupation numbers of the low-energetic states grow. It is governed by elastic collisions and the characteristic time scale is set by the collision time $\tau_{\mathrm{col}} = (n\sigma v_T)^{-1}$ with n being the peak density of the gas, σ the elastic collision cross section, and v_T the average thermal velocity. The coherent stage—which plays a significant role only in the regime of very large density or scattering length—describes the merging of quasicondensates, patched regions of locally constant phase, into a full Bose-Einstein condensate. The presence of quasicondensates could be revealed by the momentum distribution of the gas below the critical temperature.

5.2 Preparing a Non-Equilibrium Situation

We start the experiments by preparing a thermal cloud of atoms in the $|F = 1, m_F = -1\rangle$ hyperfine ground state of ^{87}Rb in a harmonic magnetic trapping potential. The trapping frequencies of the magnetic trap are $(\omega_x, \omega_y, \omega_z) = 2\pi \times (39, 7, 29)\,\mathrm{Hz}$, where z denotes the vertical axis. The temperature of the atom cloud $T = 240\,\mathrm{nK}$ is slightly above the transition temperature $T_c = 215\,\mathrm{nK}$ for Bose-Einstein condensation for the given number of atoms 1.3×10^7. This results in a collision time of $\tau_{\mathrm{col}} \approx 30\,\mathrm{ms}$. Temperature and atom number are measured by absorption imaging. The atom cloud is then brought into a strong non-equilibrium situation by rapidly lowering the trap depth to 620 nK and removing the high-energy tail of the Maxwell-Boltzmann distribution. Within the 100 ms of this "shock cooling" we remove 30% of the atoms. Subsequently, the cloud relaxes from its highly non-equilibrium state and within a few hundred milliseconds 3% of the atoms form a Bose-Einstein condensate. During the relaxation process particle number and total energy are conserved with minimal disturbance due to the detection process. Moreover, we do not observe oscillations of the condensate with respect to the detector resulting from the shock cooling.

5.3 Observing the Evolution of the System

We detect the evolution of both the density and the long-range order of the cloud simultaneously and in real time using radio frequency output coupling [111] and single atom counting [108, 112]. For output coupling we apply a weak monochromatic microwave frequency field which spin-flips atoms from the magnetically trapped state into the untrapped state $|F = 2, m_F = 0\rangle$. The untrapped atoms form a downwards propagating atomic beam. The output coupling region is defined by a surface of constant magnetic field and can be approximated by a horizontal plane within the atomic cloud [111]. Applying two microwave fields with different frequencies realizes output coupling from two vertically separated surfaces of constant magnetic field [20] which are chosen symmetric about the center of the cloud. The two overlapping atomic beams interfere with each other. The mean flux reflects the local density of atoms at the position of output coupling within the transverse momentum interval measured by our detector. The visibility of the interference pattern reflects the phase coherence. The interference pattern is detected in time with single atom resolution using an ultrahigh finesse optical cavity, located 36 mm below the magnetically trapped atoms [108]. The presence of an atom inside the cavity leads to a decrease in the transmission of a probe laser beam resonant with the empty cavity [21]. Our system permits a precise measurement of the time-dependent atom flux.

The mean atom flux and the visibility of the atomic interference pattern are determined in time bins of 50 ms length. In Figure 5.1 three different situations of the condensate formation are shown. For the cloud immediately after shock cooling (Figure 5.1(a)), the visibility is zero and the mean atom flux is low. As the condensation process develops (Figure 5.1(b)), the atom flux increases and interference arises. Both continue to grow up to a final value (Figure 5.1(c)) determined by the condensate fraction and detector function. The black lines are a fit of $f(t) = A\,[1 + V \sin(2\pi\nu t + \phi)]$ to the data. The frequency ν is the difference of the two microwave frequencies used for output coupling. The phase ϕ is determined by the relative phase of the two microwave fields which is locked to the experimental cycle. The output coupling of atoms with a rate $\approx 5 \times 10^4$ atoms per second is essentially not perturbing the density dynamics of the condensate formation. In particular, it has no detectable influence on the final condensate fraction.

The observation of long-range order even at a very small condensate fraction poses a severe technical challenge. Our detection scheme has specific properties which render the present measurement possible. The output coupling probability for a condensed atom is a factor of 4 larger than for a thermal atom due to their different density distributions for our equilib-

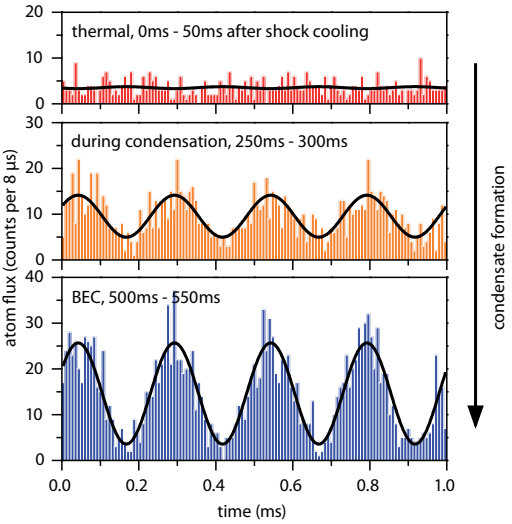

FIGURE 5.1: Buildup of density and off-diagonal long-range order during condensate formation. We plot the histogram of the atom arrival times modulo 1 ms for $\nu = 4\,\mathrm{kHz}$. The data are summed over 18 repetitions of the experiment. The black lines are fits to the data to extract the mean atom flux A and the visibility V of the interference pattern (see text).

rium parameters. Moreover, we observe unequal detection efficiencies for condensed and non-condensed atoms which we estimate to be 24% and 1%, respectively. They are mainly determined by the size of the atomic beam exceeding the active area of the detector. For thermal atoms the transverse velocity spread is larger which reduces the probability for an atom to be detected in the cavity [66]. Because of these effects the visibility of the interference pattern greatly exceeds the condensate fraction and reaches a maximum of 70% for $\Delta z > \lambda_{dB}$. We observe a reduction of the visibility towards large values of Δz (Figure 5.2). This is influenced by the following effects: Output coupling symmetrically off center from the Thomas-Fermi profile leads to a reduction of 7% at $\Delta z = 9\,\mu\mathrm{m}$. Furthermore, the spatial modes of the two interfering atom laser beams depend on their divergence and thus on the position of output coupling [113]. We calculate this effect to be 10% for the largest Δz. An additional contribution is due to the geometry of our trapping potential resulting in a tilt of the long axis of the condensate by 4° with respect to the horizontal. Moreover, the residual

uncertainty in determining the arrival times of the atoms (4 µs) limits the attainable contrast for the largest slit separations in our experiment to 94%.

5.4 Results

Figure 5.2 shows the measured visibility of the interference pattern as a function of both separation Δz and time after the quench. In the initial non-equilibrium state just after the quench we observe purely thermal-like short-range correlations which decay on a characteristic length scale given by the thermal de Broglie wavelength $\lambda_{\mathrm{dB}} \approx 0.4\,\mu\mathrm{m}$. After the first 200 ms, during which little changes are detected, the length scale over which phase correlations exist expands rapidly and the long-range order of a Bose-Einstein condensate is established after a further 100 ms. Subsequently, a stage of gradual condensate growth towards equilibrium is observed.

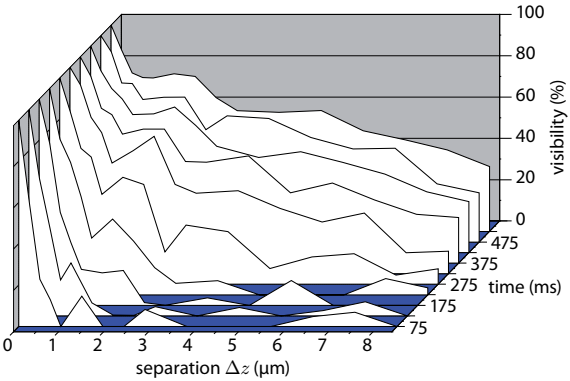

FIGURE 5.2: Formation of long-range order. Shown is the visibility of a matter wave interference pattern originating from two regions separated by Δz inside a trapped cloud. This is a measure of the first-order spatial correlation function of the atomic cloud. By shock cooling the gas is prepared in a highly non-equilibrium state at time $t = 0$ and then relaxes towards thermal equilibrium. Initially ($t = 75$ ms) the correlations are short ranged and thermal-like. The onset of Bose-Einstein condensation is marked by the appearance of long-range order extending over all measured distances ($t = 275$ ms). The largest measured distance corresponds to half of the Thomas-Fermi diameter of the final condensate. The data is taken for constant separations versus time. The substructure of the curves reflects the scatter of the initial conditions for each separation. The resulting variance in the onset of condensation is about 30 ms.

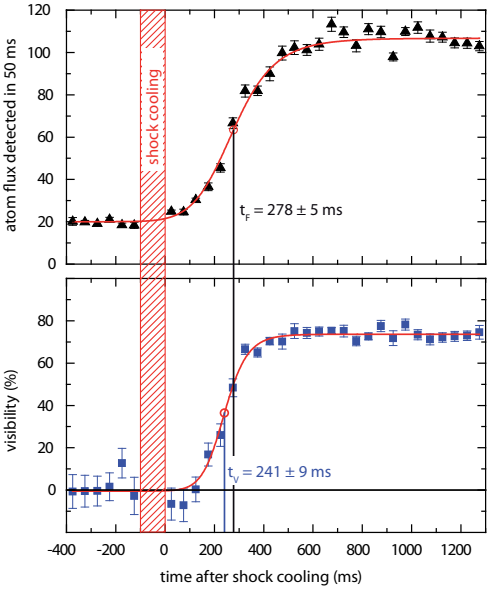

FIGURE 5.3: Growth curves for atom flux and visibility of the interference pattern during the formation of a Bose-Einstein condensate. The separation Δz between the two output-coupling regions is 1.9 µm. Before the shock cooling stage there is a low flux of thermal atoms and no interference. The growth in atom flux is significantly slower than the growth of the interference pattern. The data are averaged over 20 repetitions and the error bars indicate the statistical error of these measurements which are within a factor of 2 of the theoretical shot-noise limit.

In Figure 5.3 we show the growth of the density reflected in the mean atom flux and of the visibility for a given separation of the output coupling regions. This corresponds to a section of constant $\Delta z = 1.9\,\mu$m in Figure 5.2. We have analyzed both the delay of the formation with respect to the shock cooling stage and the speed of the formation for density and off-diagonal long-range order. We fit a function $g(t) = A_2 + (A_1 - A_2)/[1 + (t/\tau)^p]$ to the data to quantify the growth, where τ denotes the time after which 50% of the increase in flux or visibility are reached.

The duration of the condensate formation can be quantified by the time needed for an increase of both the flux and the visibility from 10% to 90% of the total increase. We find the duration to be approximately independent

of the separation Δz of the two output coupling regions. For the flux this time is 421 ± 47 ms whereas the visibility of the interference pattern grows faster in a time of 267 ± 48 ms. From the data we find that the time τ after which 50% of the total atom flux is reached is almost constant across the investigated inner region of the trapped cloud, whereas for the visibility it increases with larger slit separation. The coherent region grows with a velocity of ≈ 0.1 mm/s, approximately a factor of 5 slower than the speed of sound at the peak density of the thermal cloud. The speed of sound imposes a natural speed limit for the expansion of the coherent region. While the onset of the growth (defined by the 10 % points) starts 39 ± 54 ms earlier for the flux than for the coherence, the visibility saturates (90 % points) about 116 ± 34 ms earlier than the density. This applies to all separations Δz larger than the de Broglie wavelength.

Moreover we find that τ decreases with increasing size of the final condensate. To obtain larger condensates in equilibrium, the initial particle number or temperature or the fraction of atoms removed during shock cooling was changed. As the limiting cases we find for a final condensate number of 2.5×10^5 atoms $\tau = (282, 320)$ ms and for 8.9×10^5 atoms $\tau = (57, 114)$ ms, where the first number in the bracket refers to the visibility and the latter to the flux. The numbers are averaged over all slit separations. This decrease of the formation time for larger condensates is proportional to the increase of the elastic collision rate due to the higher final density.

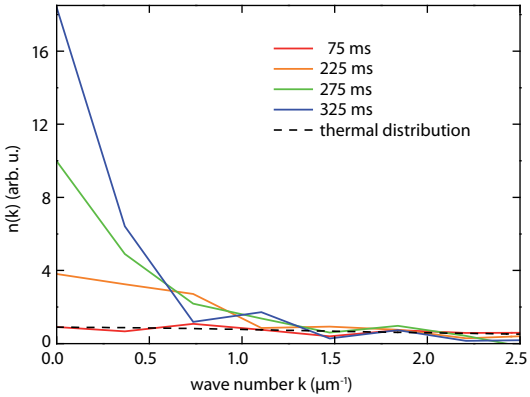

FIGURE 5.4: Temporal evolution of the momentum distribution of the detected atoms. The distribution is obtained by Fourier transformation of the visibility data. The thermal distribution is calculated for the parameters before shock cooling including a normalization factor.

It is instructive to study the evolution of the vertical momentum distribution $n(k)$ during the thermalization process. We infer the distribution $n(k)$ of the detected atoms from the Fourier transform of the visibility data of Figure 5.2 multiplied by the average flux [114]. The result is shown in Figure 5.4. For the initial state directly after the quench, the momentum distribution is well approximated by a thermal distribution (dashed line). The thermalization process after the shock cooling leads to the formation and the growth of a low-momentum peak which in equilibrium corresponds to the condensate. For our parameters in equilibrium we expect a true condensate without strong residual phase fluctuations [115]. In Figure 5.4, we focus on the beginning of the condensate formation. After 225 ms of evolution, we observe a broader low-momentum peak (width in $k \sim 0.8\,\mu\mathrm{m}^{-1}$) than for the final distribution. For evolution times of 325 ms and larger, the width of the low-momentum peak is limited by our measurement resolution of $2\pi/(16\,\mu\mathrm{m})$, which takes into account that the correlation function is symmetric with respect to $\Delta z = 0$.

In summary, we have experimentally studied the dynamics of Bose-Einstein condensation and more specifically the formation of long-range order using an interference measurement. We have quantitatively compared the evolution of the flux and of the visibility of the interference pattern. Finally, we have presented our data in terms of the atom momentum distribution.

6 Cavity QED Detection of Interfering Matter Waves

We observe the build-up of a matter-wave interference pattern from single-atom detection events in a double-slit experiment. The interference arises from two overlapping atom laser beams extracted from a Rubidium Bose-Einstein condensate. Our detector is a high-finesse optical cavity which realizes a quantum measurement of the presence of an atom and thereby projects delocalized atoms into a state with zero or one atom in the resonator. The experiment reveals simultaneously the granular and the wave nature of matter. We present a setup which is suited for applications in atom interferometry and cavity QED.

This chapter has been published as [112]: T. Bourdel, T. Donner, S. Ritter, A. Öttl, M. Köhl, and T. Esslinger. *Cavity QED detection of interfering matter waves.* Physical Review A 73(4), 043602 (2006).

6.1 Introduction

The prediction of the duality between particles and waves by de Broglie [116] is a cornerstone of quantum mechanics. The simple picture that matter waves show interferences just like classical waves neglects the granularity of matter. This analogy is valid only if the detector is classical and integrates the signal in such a way that the result is a mean particle flux. With quantum detectors that are sensitive to individual particles the discreteness of matter has to be considered. The probability to detect a particle is proportional to the square amplitude of the wave function and interferences are visible only after the signal is averaged over many particles. Interference of single massive particles have been observed using electrons [117, 118], neutrons [119], atoms [120, 121, 122] and even large molecules [123].

In the regime of atom optics, single atom detection has been achieved for example by fluorescence [124], using a microchannel plate detector for metastable atoms [125] and high-finesse optical cavities [21]. Only very recently the single atom detection capability has been achieved together with quantum degenerate samples reaching the regime of quantum atom optics [108, 126]. In our experiment, we detect single atoms from a coherent matter-wave field using a high-finesse optical cavity in the strong coupling regime of cavity quantum electrodynamics (QED) [127, 128, 73].

For atoms with a spatially extended wave function, such as in a Bose-Einstein condensate or in an atom laser beam, a measurement projects the delocalized atom into a state localized at the detector [129]. This quantum measurement requires dissipation in the detection process. For our cavity QED detection method, we study the open quantum system composed of coupled matter-wave and light fields. The two sources of dissipation are cavity losses and spontaneous emission. In particular, we calculate the time needed for the localization of an atom along the beam in the cavity measurement process. We then experimentally investigate atomic interferences using our detector, which can resolve single-atom transits in time. The high detection efficiency opens new perspectives for atom interferometry such as quantum limited detection of amplitude and phase of a matter-wave [130].

A schematic of our experimental setup is shown in Figure 6.1. We output couple two weak atom laser beams from a Bose-Einstein condensate and their wave functions overlap and interfere [20]. The flux is adjusted in such a way that there is on average only one atom at a time in the interferometer. Using the high-finesse cavity we measure single-atom arrival times in the overlapping beams. We observe the gradual appearance of a temporal high-contrast matter-wave interference pattern as more and more detection events are accumulated.

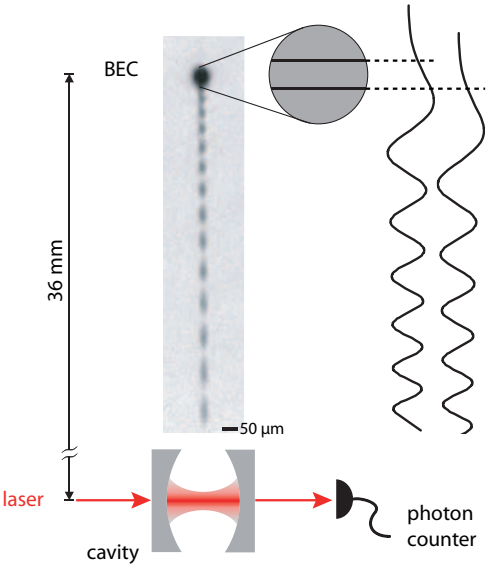

FIGURE 6.1: Schematic of the experimental setup. From two well-defined regions in a Bose-Einstein condensate (BEC), we couple atoms to an untrapped state. The real parts of the resulting atom laser wave functions are sketched on the right hand side. The absorption image shows an interference pattern corresponding to $\Delta f = 1\,\mathrm{kHz}$ and an atom flux $\sim 10^6$ times larger than in the actual single-atom interference experiment. Monitoring the transmission of a probe laser through a high-finesse optical cavity with a photon counter, single-atom transits are detected.

6.2 Quantum Measurement in a Cavity QED System

Single-atom detection in an optical cavity can be captured in a classical picture: an atom changes the index of refraction in the cavity and thereby shifts it out of resonance from the probe laser frequency. In the absence of an atom, the probe beam is resonant with the cavity and its transmission is maximal. Experimentally we use a probe power corresponding to five photons on average in the cavity. The cavity lock is sufficiently stable for the cavity transmission to be at the photon shot-noise limit. The presence of an atom results in a drop of the cavity transmission (see Figure 6.2). We set the threshold for an atom detection event to a drop in transmission

of four times the standard deviation of the photon shot noise in our 20 µs integration time. Then the overall detection efficiency of atoms extracted from a Bose-Einstein condensate is measured to be 0.23(8). It is mainly limited by the size of the atom laser which exceeds the dimension of the cavity mode and can be increased using a laser to guide the atoms into the detector.

The length of the cavity is 176 µm, the mode waist radius is 25 µm, and its finesse is 3×10^5. The maximum coupling strength between a single ^{87}Rb atom and the cavity field $g = 2\pi \times 10.4\,\mathrm{MHz}$ is larger than the cavity field decay rate $\kappa = 2\pi \times 1.4\,\mathrm{MHz}$ and the atom dipole decay rate $\gamma = 2\pi \times 3\,\mathrm{MHz}$. The probe laser and the cavity are red-detuned as compared to the atomic resonance so that the light force pulls the atoms to regions where the coupling is large, therefore enhancing the detection efficiency.

To understand the actual detection process we study the dynamics of the atom-cavity quantum system taking into account dissipation. We first consider a classical atom entering a simplified square shaped cavity mode so that its coupling to the cavity field increases suddenly to a constant value g. Thereby we do not take into account the atom dynamics due to the dipole potential of the standing-wave cavity mode. The cavity field is initially coherent with a few photons. We use a two-level approximation for the atom description and assume a 30 MHz red-detuning of the probe laser compared to the atomic resonance. Our probe beam is linearly polarized orthogonally to the magnetic field direction. We therefore do not probe on a cycling transition. The 30 MHz detuning is an effective value chosen to match the experimental conditions. In the case of strong coupling the following dynamics occur. On a short time scale given by $1/g$, the atom-cavity system exhibits coherent oscillations. It progressively reaches an equilibrium state on a time scale given by $1/\kappa$ and $1/\gamma$ due to cavity loss and atomic spontaneous emission. These are the two sources of dissipation. In the equilibrium state, the mean photon number in the cavity is reduced and the cavity transmission drops.

To evaluate this drop quantitatively, we find the steady-state of the master equation for the density matrix numerically [131, 132, 133, 60]. For our parameters the transmission as a function of the coupling strength g is plotted in Figure 6.3(a). For a maximally coupled atom $g = 2\pi \times 10.4\,\mathrm{MHz}$, the average intracavity photon number is found to be reduced from 5 to 0.8, and the number of detected photons is then reduced by the same ratio. Such a reduction corresponds well to the largest observed transmission drops. An example is shown in Figure 6.2. The detection threshold corresponds to a coupling of $g = 2\pi \times 6.5\,\mathrm{MHz}$. Experimentally, unlike in our model, an atom

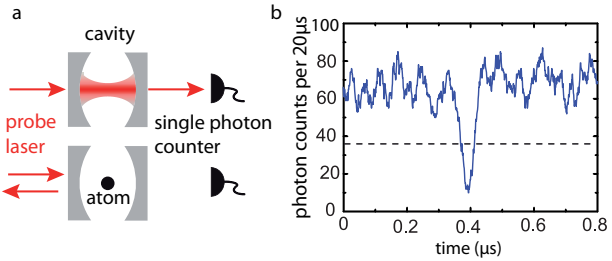

FIGURE 6.2: (a) Cavity single atom detection principle. An atom detunes the high-finesse cavity from resonance and the cavity transmission consequently drops. (b) Photon flux through the high-finesse optical cavity when an atom is detected. The photon count rate is averaged over 20 µs. The detection threshold is set to be four times the standard deviation of the photon shot noise (dashed line).

feels a position dependent coupling as it transverses the mode profile. However, the atom transit time through the cavity mode (45 µs) is long compared to the cavity relaxation time scales $1/\kappa$ and $1/\gamma$ and the atom-cavity system adiabatically follows a quasiequilibrium state. Therefore the experimental transmission drops can be compared to the calculated ones.

Specific to our experiment is that a longitudinally extended matter wave and not a classical atom enters the cavity [134]. Our system allows us to realize a quantum measurement of the presence of an atom. For our low atom flux, we can neglect the probability of having more than one atom at a time in the cavity. The incoming continuous wave function is thus projected into a state with one or zero atom in the cavity. This evolution from a pure quantum state to a statistical mixture involves decoherence. The latter is introduced by spontaneous scattering and cavity photon loss. The origin of the decoherence can be understood as unread measurements in the environment [132, 129]. For example, if a spontaneously emitted photon is detected, there is necessarily an atom in the cavity and the wave function is immediately projected. Similarly, the more different the light field with an atom in the cavity is from the field of an empty cavity, the more different is the scattered radiation out of the cavity, and the projection occurs correspondingly faster.

We now quantify the time needed for the projection to occur. For simplicity, rather than a continuous wave function, we consider a coherent mixture of one and zero atom entering a square shaped cavity at a given time. We take the limit where the probability to have one atom is low. The initial

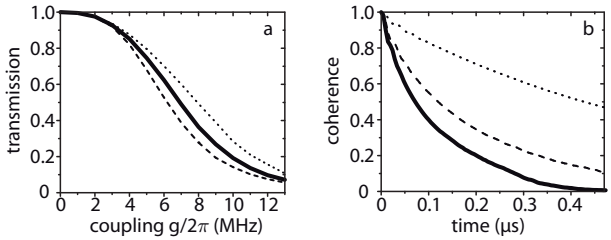

FIGURE 6.3: (a) Normalized transmission as a function of coupling strength. The solid line corresponds to our probe strength of 5 photons in the cavity in the absence of an atom. The dashed line is the weak probe limit. The dotted line corresponds to 10 photons in the cavity. (b) Coherence between the states with one and no atom as a function of time. The initial coherence is normalized to 1. Solid line: $g = 2\pi \times 10\,\mathrm{MHz}$. Dashed line: $g = 2\pi \times 6.5\,\mathrm{MHz}$. Dotted line: $g = 2\pi \times 3\,\mathrm{MHz}$.

cavity field is the one of an empty cavity. Dissipation effects are studied by computing the time evolution of the density matrix [133]. The degree of projection of the initial state can be extracted from the off-diagonal terms between states with one atom and no atom in the density matrix. More precisely, we define the coherence as the square-root of the sum of the squared modulus of the off-diagonal terms mentioned above. This quantity is maximal for a pure quantum state with equal probability to have an atom or not. The coherence is zero for a statistical mixture.

In Figure 6.3(b) the temporal evolution of the coherence is plotted. As expected, it decays to zero at long times due to dissipation. The decay time increases as the coupling to the cavity is weakened. In the limit where the coupling vanishes, the coherence is preserved. The atomic wave function then evolves as if there was no cavity. For $g > 2\pi \times 6.5\,\mathrm{MHz}$, the decoherence time is found to be a fraction of a microsecond. This time is much shorter than the 45 μs transit time of an atom through the cavity, and for all our detected atomic transits the wave function is thus well projected to a state with one atom. Our detection scheme realizes a quantum measurement of the presence of an atom in the cavity. However during an atom transit some photons are spontaneously scattered and the velocity of the atom is slightly modified.

6.3 Single Atom Interference

Using our cavity detector we can observe matter wave interferences on the single atom level. The starting point of the experiment is a quasi pure Bose-Einstein condensate with 1.5×10^6 Rubidium atoms in the hyperfine ground state $|F = 1, m_F = -1\rangle$ [108]. The atoms are magnetically trapped with frequencies $\omega_x = 2\pi \times 38.6\,\mathrm{Hz}$, $\omega_y = 2\pi \times 7.2\,\mathrm{Hz}$ and $\omega_z = 2\pi \times 29.1\,\mathrm{Hz}$ with the vertical z-axis defined by gravity. A weak and continuous microwave field locally spin-flips atoms from the Bose-Einstein condensate into the untrapped $|F = 2, m_F = 0\rangle$ state. This process is resonant for a section of the condensate where the magnetic field is constant. Because the magnetic moment of the spin flipped atoms vanishes, they fall due to gravity and form a continuous atom laser [111].

When we apply two microwave fields of different frequencies, we are able to output couple atom laser beams from two well defined slices of the condensate [20]. The two distinct atom laser wave functions overlap and interfere. At the entrance of the cavity, the atomic wave function ψ is well described by the sum of two plane waves with the following time dependence

$$\begin{aligned} \psi(t) &\propto \exp(i\omega_1 t) + \exp(i(\omega_2 t + \phi)) \\ &\propto \cos((\omega_2 - \omega_1)t/2 + \phi_2) \end{aligned} \tag{6.1}$$

where $\hbar\omega_1$ and $\hbar\omega_2$ are the energies of the two laser beams and ϕ is a fixed phase difference. The radial dependence of the wave function is neglected. The probability to detect an atom is given by the square norm of the wave function which is modulated in time and behaves like a cosine squared. The modulation frequency of the interference signal is given by the energy difference between the two atom lasers. Experimentally, it is determined by the frequency difference of the two microwave fields and is chosen to be $\Delta f = 10\,\mathrm{Hz}$, which corresponds to a distance of 5 nm between the two output-coupling regions. The two microwave fields are generated such that the interference pattern is phase stable from one experimental run to the other.

The results of the experiment are presented in Fig. 6.4. Each experimental run corresponds to output coupling from a new condensate. On average ~ 6 atoms are detected in 0.5 s. After the detection of a few atoms, the interference pattern is not yet visible (Figure 6.4(a)). Nevertheless, after adding the results of several runs, it progressively appears (Figure 6.4(b)–6.4(d)). Experimentally, the atom number fluctuation is found to be dominated by the atomic shot noise and the signal-to-noise ratio of the interference increases as more data are included. A fit to the histogram yields a contrast

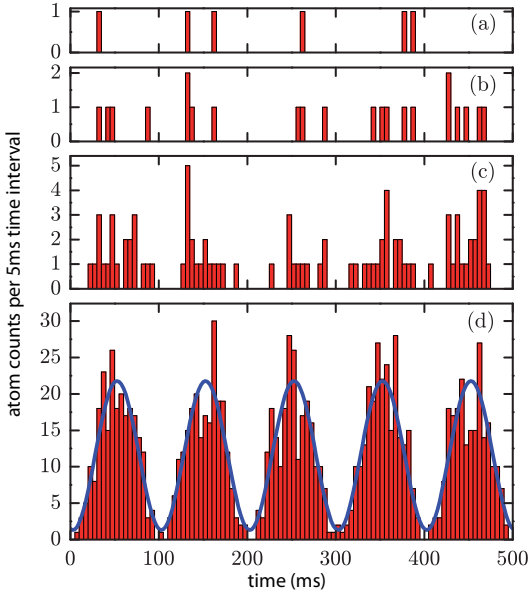

FIGURE 6.4: Histograms of the atoms detected in 5 ms time intervals. (a) Single experimental run. (b) Sum of 4 runs. (c) Sum of 16 runs. (d) Sum of 191 runs, the line is a sinusoidal fit. Please note the different scales.

of 0.89(5). The slight reduction of contrast is explained by a detected flux of about one atom every 3 runs in the absence of output coupling. We attribute this effect to artifact detection events and to atoms output coupled from stray microwave fields. Using a higher flux, we were able to detect an interference contrast in excess of 0.97.

Here, we work with a flux of one detected atom per 83 ms, which is about the time an atom needs to travel from the condensate region to the cavity. We are thus in a regime where the atoms fall one by one in the interferometer. Thereby a single atom interferes with itself. It behaves both like a wave because its time arrival probability shows an interference pattern and like a particle when detected. This can be similarly expressed by saying that each individual atom is released from both slits simultaneously. Our experiment is an atomic counterpart of Young's double slit experiment with individual photon detection.

6.4 Summary

In conclusion, we detect matter wave interferences with a high-finesse optical cavity detector which realizes a quantum measurement of the presence of an atom. We explain how dissipation plays a crucial role in the detection process and for the localization of the atom inside the cavity. Using this detector, we are able to detect a high contrast atom interference pattern at the single atom level. The coupling of a matter wave to a cavity QED system opens the route to the quantum control not only of the internal state of the atoms but also of their positions [135]. Using the presented detection technique we can probe an atomic gas with a good quantum efficiency and introduce only a minimum perturbation through the measurement. With our setup quantum limited detection of the phase between two distinct condensates would permit investigations of their relative phase evolution [136, 137], build-up [138, 139, 140], or diffusion [141].

7 Cavity QED with a Bose-Einstein Condensate

Cavity quantum electrodynamics describes the coherent interaction between matter and an electromagnetic field confined within a resonator structure, and provides a useful platform for developing concepts in quantum information processing [142]. By using high-quality resonators, a strong-coupling regime can be reached experimentally in which atoms coherently exchange a photon with a single light-field mode many times before dissipation sets in. This has led to fundamental studies with both microwave [143, 144] and optical resonators [145]. To meet the challenges posed by quantum state engineering [146] and quantum information processing, recent experiments have focused on laser cooling and trapping of atoms inside an optical cavity [147, 148, 73]. However, the tremendous degree of control over atomic gases achieved with Bose-Einstein condensation [1] has so far not been used for cavity QED. Here we achieve the strong coupling of a Bose-Einstein condensate to the quantized field of an ultrahigh-finesse optical cavity and present a measurement of its eigenenergy spectrum. This is a conceptually new regime of cavity QED, in which all atoms occupy a single mode of a matter-wave field and couple identically to the light field, sharing a single excitation. This opens possibilities ranging from quantum communication [149, 150, 151] to a wealth of new phenomena that can be expected in the many-body physics of quantum gases with cavity-mediated interactions [135, 152].

Parts of this chapter have been published as [153]: F. Brennecke, T. Donner, S. Ritter, T. Bourdel, M. Köhl, and T. Esslinger. *Cavity QED with a Bose-Einstein condensate.* Nature 450, 268 (2007).

7.1 Introduction

The coherent coupling of a single two-level atom with one mode of the quantized light field leads to a splitting of the energy eigenstates of the combined system and is described by the Jaynes-Cummings model [154]. For the experimental realization the strong-coupling regime has to be reached, where the maximum coupling strength g_0 between atom and light field is larger than both the amplitude decay rate of the excited state γ and that of the intracavity field κ. In the case of a thermal ensemble of atoms coupled to a cavity mode, the individual, position-dependent coupling for each atom has to be taken into account.

To capture the physics of a Bose-Einstein condensate (BEC) coupled to the quantized field of a cavity, we consider N atoms occupying a single wave function. Because the atoms are in the same motional quantum state, the coupling g to the cavity mode is identical for all atoms. Moreover, bosonic stimulation into the macroscopically populated ground state should largely reduce the scattering of atoms into higher momentum states during the coherent evolution. This situation is therefore well described by the Tavis-Cummings model [59], where N two-level atoms are assumed to identically couple to a single field mode. A single cavity photon resonantly interacting with the atoms then leads to a collective coupling of $g\sqrt{N}$.

A key characteristic of the coupled BEC-cavity system is its eigenenergy spectrum, which we map out with a single excitation present. An ensemble of thermal atoms does not fulfill the requirement of identical coupling, but it shows a similar energy spectrum, which can be modeled by the Tavis-Cummings Hamiltonian with an effective collective coupling [56]. In previous measurements [155, 156] and also in a very recent report [157], these eigenenergies have been measured for thermal atoms coupled to a cavity. Aside from the sensitivity of the spectrum to the precise spatial distribution of the atoms, the differences between a BEC and a thermal cloud, or between a BEC and a Mott insulator, should be accessible through the fluctuations of the coupling, that is, in the width of the resonances [158].

First experiments bringing together BEC physics and cavities concentrated on correlation measurements using single atom counting [108], studied cavity-enhanced superradiance of a BEC in a ring cavity [159], observed nonlinear and heating effects for ultracold atoms in an ultrahigh-finesse cavity [160, 161], and achieved very high control over the condensate position within an ultrahigh-finesse cavity using atom-chip technology [157].

7.2 Producing a BEC in a High-Finesse Cavity

To create a BEC inside an ultrahigh-finesse optical cavity we optically transport the atoms from the QUIC trap to the position of the cavity mode (see Section 3.3). In the magnetic trap we produce 3.5×10^6 ^{87}Rb atoms in the $|F, m_F\rangle = |1, -1\rangle$ state with a small condensate fraction present. The atoms are then loaded into the dipole potential of a vertically oriented standing wave, formed by two counter-propagating laser beams (see Figure 3.5). By varying the frequency difference δ between the upwards and the downwards propagating wave, the standing-wave pattern, and with it the confined atoms, move downwards [72, 73]. The transport of the atoms into the cavity is accomplished in $T = 100\,\mathrm{ms}$ with a maximum acceleration of $a = 22.4\,\mathrm{m\,s^{-2}}$. The intensity and frequency of each transport beam are precisely controlled by acousto-optical modulators, which are driven by two phase-locked, homebuild direct digital synthesis generators. With the maximally available power of 76 mW per beam the trap depth at the position of the magnetic trap is 1.1 µK. During transport, the power in the laser beams is kept constant until the intensity at the position of the atoms has increased by a factor of ten. Subsequently, this intensity is kept constant.

Because of continuous evaporative cooling during the transport, the number of atoms arriving in the cavity is reduced to typically 8.4×10^5 atoms with a small condensate fraction present. During the 100 ms of transport a small magnetic field is applied to provide a quantization axis and the sample remains highly spin-polarized in the $|1, -1\rangle$ state. However, owing to off-resonant scattering in the transport beams, a small fraction of the atoms undergoes transitions into the $|F = 2\rangle$ hyperfine state manifold.

At the position of the cavity mode, the atoms are loaded into a crossed-beam dipole trap formed by one of the transport beams and an additional, horizontal dipole beam with a waist radius of $w_x = w_z = 27\,\mu\mathrm{m}$ (see Figure 3.5). A final stage of evaporative cooling is performed by lowering the laser power to final trapping frequencies $(\omega_x, \omega_y, \omega_z) = 2\pi \times (290, 43, 277)\,\mathrm{Hz}$, ending up with an almost pure condensate of 2.2×10^5 atoms.

The ultrahigh-finesse cavity has a length of 176 µm and consists of symmetric mirrors with a 75 mm radius of curvature, resulting in a mode waist radius of 25 µm. A slight birefringence splits the resonance frequency of the empty cavity for the two orthogonal, principal polarization axes by 1.7 MHz. With the relevant cavity QED parameters $(g_0, \kappa, \gamma) = 2\pi \times (10.6, 1.3, 3.0)\,\mathrm{MHz}$, the system is in the strong coupling regime. The length of the cavity is actively stabilized using a laser at 830 nm [66]. The intracavity intensity of the stabilization light gives rise to an additional dipole potential of $2.4\,E_{\mathrm{rec}}$, with the recoil energy defined as $E_{\mathrm{rec}} = h^2/(2m\lambda^2)$,

where m is the mass of the atom. The chemical potential $\mu = 1.8E_{\mathrm{rec}}$ of 2.2×10^5 trapped atoms is comparable to the depth of this one-dimensional lattice, so that long-range phase coherence is well established in the atomic gas. The 1/e lifetime of the atoms in the combined trap was measured to be 2.8 s.

7.3 Theoretical Model

To characterize the coupled BEC-cavity system theoretically, we start with the second-quantized Hamiltonian describing the matter-light interaction in the electric-dipole and rotating-wave approximation (see Section 2.2). We take all hyperfine states including their Zeeman sublevels in the $5^2\mathrm{S}_{1/2}$ and $5^2\mathrm{P}_{3/2}$ state manifolds of ^{87}Rb into account. We describe the cavity degrees of freedom by two orthogonal linear polarizations of the TEM_{00} mode. The quantization axis, experimentally provided by a small magnetic field, is chosen to be oriented parallel to the cavity axis. The near-planar cavity supports higher-order transverse modes equally spaced by $\Delta_{\mathrm{t}} = 2\pi \times 18.5\,\mathrm{GHz}$. To incorporate the coupling to all higher-order transverse modes we include one additional effective cavity mode in our model with its resonance frequency shifted by Δ_{t} with respect to that of the TEM_{00} mode.

Considering only one spatial atomic mode for the ground state manifold and another one for the excited-state manifold, the Hamiltonian of the uncoupled system reads

$$\hat{H}_0 = \sum_i \hbar\omega_{g_i}\,\hat{g}_i^\dagger\hat{g}_i + \sum_j \hbar\omega_{e_j}\,\hat{e}_j^\dagger\hat{e}_j + \sum_{k=0}^{1}\sum_{p=\rightarrow,\uparrow} \hbar\omega_k\,\hat{a}_{k,p}^\dagger\hat{a}_{k,p} \tag{7.1}$$

where the indices i and j label the states $5^2\mathrm{S}_{1/2}|F, m_F\rangle$ and $5^2\mathrm{P}_{3/2}|F', m_{F'}\rangle$, respectively. The operators $\hat{g}_i^\dagger$ (or $\hat{g}_i$) and $\hat{e}_j^\dagger$ (or $\hat{e}_j$) create (or annihilate) an atom in the mode of the corresponding ground and excited states with frequencies ω_{g_i} and ω_{e_j}. The operators $\hat{a}_{k,p}^\dagger$ (or $\hat{a}_{k,p}$) create (or annihilate) a photon with energy $\hbar\omega_k$ and linear polarization p in the cavity mode k, where $k = 0, 1$ labels the TEM_{00} mode and the additional effective cavity mode, respectively.

The coupling between the BEC and the cavity is described by the interaction Hamiltonian

$$\hat{H}_{\mathrm{int}} = -i\hbar\sum_{k=0}^{1}\sum_{p=\rightarrow,\uparrow}\sum_{i,j} g_{ij}^{k,p}\,\hat{e}_j^\dagger\,\hat{a}_{k,p}\,\hat{g}_i + \mathrm{h.c.} \tag{7.2}$$

where $g_{ij}^{k,p}$ denotes the coupling strength for the transition $i \rightarrow j$ driven by the cavity mode k with polarization p, and h.c. is the hermitian conjugate.

For the TEM_{00} mode the coupling strength $g_{ij}^{0,p}$ depends on the dipole matrix element $\mathcal{D}_{ij}^{p}$ for the transition $i \to j$ driven by the polarization p, the mode volume V_0, and the overlap $\mathcal{U}_0$ between the two spatial atomic modes and the TEM_{00} mode:

$$g_{ij}^{0,p} = \mathcal{D}_{ij}^{p} \sqrt{\frac{\hbar\omega_0}{2\epsilon_0 V_0}}\, \mathcal{U}_0. \tag{7.3}$$

We numerically calculated the ground state of the Gross-Pitaevskii equation in the potential formed by the dipole trap and the cavity stabilization light for $N = 2 \times 10^5$ atoms, and found the spatial overlap between BEC and TEM_{00} mode to be $\mathcal{U}_0 = 0.63$. Because of the position uncertainty of the BEC relative to the cavity mode, the overlap might deviate by up to 20 % from this value. The repulsive interaction between the atoms leads to a slight decrease in $\mathcal{U}_0$ with increasing atom number, which was found numerically to follow $\mathcal{U}_0(N) = \sqrt{0.5}(1 - 0.0017N^{0.34})$. For the coupling strength to the additional effective cavity mode we assume $g_{ij}^{1,p} = r g_{ij}^{0,p}$, with r being a free parameter.

The initial atomic population of the several ground states i given by the free parameters N_i is relevant for the form of the energy spectrum of the coupled BEC-cavity system. To find the energy spectrum in the weak excitation limit we can restrict the analysis to states containing a single excitation. These are the states $|1_{k,p}; N_1, \ldots, N_8; 0\rangle$, where one photon with polarization p is present in the mode k and all atoms are in the ground-state manifold, and also all possible states $|0_{k,p}; N_1, \ldots, N_i - 1, \ldots, N_8; 1_j\rangle$, where no photon is present and one atom was transferred from the ground state i to the excited state j. Diagonalization of the Hamiltonian $\hat{H} = \hat{H}_0 + \hat{H}_{\mathrm{int}}$ in the truncated Hilbert space spanned by these states yields the eigenspectrum of the coupled system as a function of the cavity detuning Δ_c.

The detuning of the lower resonance branch at $\Delta_\mathrm{c} = 0$ is a function of the atom number and given by

$$|\Delta_\mathrm{p}| = \mathcal{U}_0(N) g_{\sigma^\pm} \sqrt{N} + \frac{(\mathcal{U}_0(N) r g_{\sigma^\pm})^2 N}{2\Delta_\mathrm{t}} + \mathcal{O}(1/\Delta_\mathrm{t}^2)\,. \tag{7.4}$$

7.4 Probing the Coupled System

To find the eigenenergies of the coupled BEC-cavity system for a single excitation, we perform transmission spectroscopy with a weak, linearly polarized probe laser of frequency ω_p. To this end, the resonance frequency of the empty cavity is stabilized to a frequency ω_c, which in general is detuned by a variable frequency $\Delta_\mathrm{c} = \omega_\mathrm{c} - \omega_\mathrm{a}$ with respect to the frequency ω_a of the $|F = 1\rangle \to |F' = 2\rangle$ transition of the D_2 line of $^{87}\mathrm{Rb}$. The transmission of

the probe laser through the cavity is monitored as a function of its detuning $\Delta_p = \omega_p - \omega_a$ (see Figure 7.1). The two orthogonal circular polarizations of the transmitted light are separated and detected with single-photon counting modules. The overall detection efficiency for an intracavity photon is 5 %. To probe the system in the weak excitation limit, the probe laser intensity is adjusted such that the mean intracavity photon number is always below the critical photon number $n_0 = \gamma^2/(2g_0^2) = 0.04$. A magnetic field of 0.1 G, oriented parallel (within 10 %) to the cavity axis provides a quantization axis.

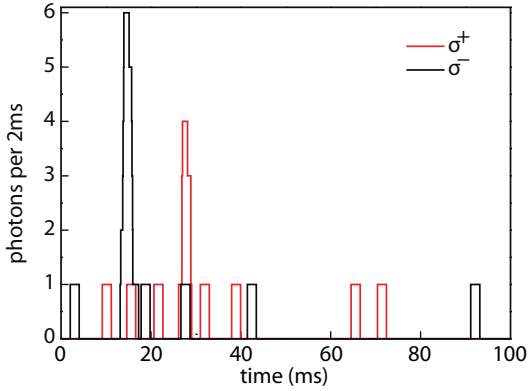

FIGURE 7.1: Cavity transmission for the σ^+ and σ^- polarization component. The probe laser frequency is scanned at a speed of 25 MHz ms^{-1} while the cavity detuning is fixed. The original transmission data, recorded with a resolution of 0.4 µs, is averaged over 2 ms using a sliding average. A single peak for each polarization can clearly be distinguished from the background of about 60 dark counts per second.

From individual recordings of the cavity transmission as shown in Figure 7.1 we map out the low-excitation spectrum of the coupled system as a function of Δ_c (see Figure 7.2). After resonant excitation we do not detect an influence on the BEC in absorption imaging for large atom numbers (see Figure 3.5). For small BECs of the order of 5,000 atoms we observe a loss of 50 % of the atoms after resonant probing. The normal mode splitting at $\Delta_c = 0$ amounts to 7 GHz for σ^+ polarization, which results in a collective cooperativity of $C = Ng^2/(2\gamma\kappa) = 1.6 \times 10^6$. The splitting for the σ^- component is smaller, because the dipole matrix elements for transitions starting in $|1, -1\rangle$ driven by this polarization are smaller than those for σ^+.

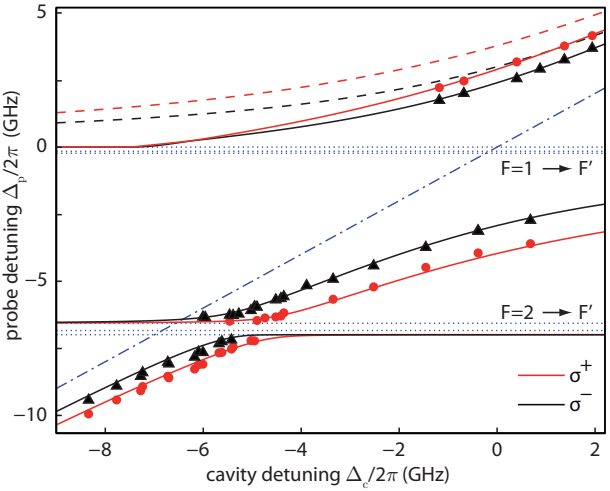

FIGURE 7.2: Energy spectrum of the coupled BEC-cavity system. The data points are measured detunings of resonances for σ^+ (red circles) and σ^- (black triangles) polarized light. Each data point is the average of three measurements with an uncertainty of about 25 MHz. The solid lines are the result of a theoretical model (see Methods). Bare atomic resonances are shown as dotted lines, whereas the empty cavity resonance of the TEM_{00} mode is plotted as a dashed-dotted line. Note the asymmetry in the splitting at $\Delta_c = 0$ caused by the influence of higher-order transverse modes. Neglecting this influence, the eigenenergies shown by the dashed lines would be expected where the free parameters were adjusted to fit the spectrum for $\Delta_p < 0$.

A striking feature of the energy spectrum in Figure 7.2 is a second avoided crossing at probe frequencies resonant with the bare atomic transitions $|F = 2\rangle \rightarrow |F' = 1, 2, 3\rangle$. It is caused by the presence of atoms in the $|F = 2\rangle$ hyperfine ground state. This avoided crossing is located at a cavity detuning where the eigenenergy branch of the BEC-cavity system with no atoms in $|F = 2\rangle$ would intersect the energy lines of the atomic transitions $|F = 2\rangle \rightarrow |F' = 1, 2, 3\rangle$. Accordingly, the avoided crossing is shifted by approximately $Ng^2/\Delta_p = 2\pi \times 1.8\,\mathrm{GHz}$ with respect to the intersection of the empty cavity resonance with the bare atomic transition frequencies.

We apply our theoretical model (see 7.3) and find good agreement between the measured data and the model (see Figure 7.2) for 154,000 atoms in the $|1, -1\rangle$ state and for 2,700 atoms (e.g. 1.7 % of the total number of atoms)

distributed over the Zeeman sublevels of the $|F = 2\rangle$ state, with the majority in $|2, -1\rangle$.

Our near-planar cavity supports higher-order transverse modes equally spaced by 18.5 GHz, which is of the order of the collective coupling $g\sqrt{N}$ in our system. In general, the presence of one additional mode with the same coupling but detuned from the TEM_{00} mode by Δ_t would shift the resonance frequencies at Δ_c to first order by $Ng^2/(2\Delta_\mathrm{t})$. Good agreement with the measured energy spectrum is found for the above given ground-state population and a coupling between BEC and the effective cavity mode (see Section 7.3) that is $r = 1.2$ times the coupling to the TEM_{00} mode. In our system, this coupling to higher order modes results in a clearly visible change of the energy spectrum with respect to a system with a single cavity mode only (see dashed lines in Figure 7.2). This can be seen as a variant of the "superstrong coupling regime" [162], in which the coupling between atoms and the light field is of the order of the free spectral range of the cavity.

7.5 Atom Number Dependence

To test the square-root dependence of the normal mode splitting on the number of atoms in the BEC, a second measurement was conducted. We set the cavity frequency to $\Delta_\mathrm{c} = 0$ and record the detuning of the lower coupled state from the bare atomic resonance $|F = 1\rangle \rightarrow |F' = 2\rangle$ as a function of the number of atoms as displayed in Fig. 7.3. The atom number was varied between 2,500 and 200,000, determined from separately taken absorption images with an estimated statistical error of $\pm 10\,\%$; possible systematic shifts are estimated to be within $\pm 7\,\%$. The dependence of $|\Delta_\mathrm{p}|$ on the number of atoms is well described by a square root, as expected from the Tavis-Cummings model (dashed lines). However, for a weakly interacting BEC the size of the atomic cloud—and thus the spatial overlap with the cavity mode—depends on the atom number. Our more detailed model, which includes this effect, as well as the influence of higher-order cavity modes, yields maximum single-atom couplings of $g_{\sigma^+} = 2\pi \times (14.4 \pm 0.3)\,\mathrm{MHz}$ and $g_{\sigma^-} = 2\pi \times (11.3 \pm 0.2)\,\mathrm{MHz}$ for the two polarization components (solid lines). This result agrees well with the theoretical predictions for the effective Clebsch-Gordan coefficients for the σ^+ ($g_{\sigma^+}^{\mathrm{theory}} = 2\pi \times 14.2\,\mathrm{MHz}$) and σ^- ($g_{\sigma^-}^{\mathrm{theory}} = 2\pi \times 11.0\,\mathrm{MHz}$) transitions starting in state $|1, -1\rangle$.

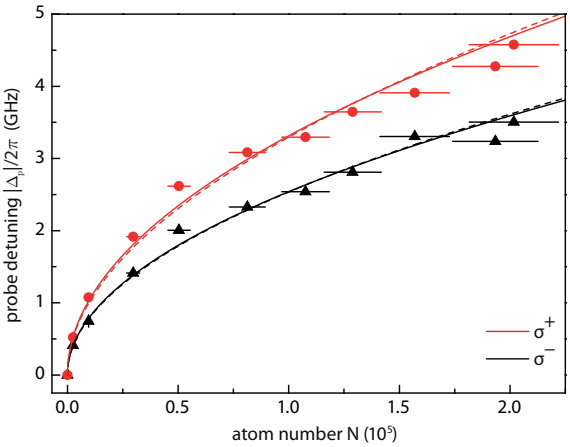

FIGURE 7.3: Shift of the lower resonance of the coupled BEC-cavity system from the bare atomic resonance. The cavity was locked at $\Delta_c = 0$. σ^+ and σ^- polarization are shown as red circles and black triangles, respectively. Each data point is the average of three measurements. The atom number was determined separately from absorption images with an assumed error of $\pm 10\%$; the vertical error bars are too small to be resolved. The dashed lines are fits of the square root dependence on the atom number, as predicted by the Tavis-Cummings model. The solid lines are fits of a more detailed theoretical model (see Methods) resulting in maximum coupling rates $g_{\sigma^+} = 2\pi \times (14.4 \pm 0.3)$ MHz and $g_{\sigma^-} = 2\pi \times (11.3 \pm 0.2)$ MHz. The ratio of the two coupling rates of 1.27 ± 0.03 agrees with the expected ratio of 1.29 of the corresponding Clebsch-Gordan coefficients.

7.6 Summary

We optically transported an ultracold atomic cloud into our ultrahigh-finesse optical cavity. The atoms were evaporatively cooled to quantum degeneracy in a crossed-beam dipole trap at the position of the cavity mode. We probed the low-excitation spectrum of the coupled system and observed a large collective coupling. The atom-number dependence of the coupling strength showed the typical square root behavior expected from the Tavis-Cummings model. We modeled the data with a detailed theory including all relevant transitions and the influence of higher-order cavity modes and found excellent agreement with the experiment.

The coupling of a single mode of a matter-wave field to a single cavity

mode opens a route to new experiments. It facilitates the manipulation and study of statistical properties of quantum-degenerate matter-wave fields by a quantized optical field, or even the generation of entanglement between these two fields [158, 163]. The detection of single atoms falling through the cavity has already been demonstrated with this set-up [108]. In principle, the detection of small impurity components embedded in a large BEC presented here can also be extended to single atoms. This is an important step towards the realization of schemes aiming at the cooling of qubits immersed in a large BEC [164].

8 Conclusions

Within the scope of this thesis, experiments were carried out combining the methods and physics of the two research fields of Bose-Einstein condensation and cavity quantum electrodynamics. A BEC apparatus including an ultra-high finesse optical cavity in the strong coupling regime was used to explore a variety of fascinating aspects of the two constituents.

Excellent control over the temperature of the gas and the high sensitivity of our interference-based measurement allowed us to explore the critical regime of a dilute, trapped and weakly interacting Bose gas for the first time. In this regime the behavior of the gas is dominated by thermally driven critical fluctuations. We observed the change in the decay of the first-order correlation function from exponential towards algebraic. The shape of the correlation function is governed by the divergence of the correlation length. From this divergence we determined the critical exponent of the correlation length $\nu = 0.67 \pm 0.13$ [75]. Prior to the experiment, it was not obvious that the determination of a critical exponent would be possible with a quantum gas. However, a unique number of conditions could be met to realize this measurement, in which local properties of a mesoscopic system are probed. This experiment represents one of the first non-trivial quantitative measurements carried out with ultracold gases.

Our method opens possibilities to investigate both classical and quantum phase transitions. A similar setup can be envisioned to investigate the superfluid to Mott insulator quantum phase transition of bosons in an optical lattice [22]. In this kind of phase transitions the critical fluctuations are driven by quantum rather than by thermal noise. By emulating condensed matter systems with the versatile methods of quantum atom optics, knowledge on otherwise unaccessible properties of complex physical situations can be gained [17].

With the real-time access to the correlation function even the dynamics of phase transitions [165] can be observed. We prepared a Bose gas in a highly non-equilibrium situation and observed how coherence spreads out when a

condensate forms [100]. This is a first step towards the measurement of non-trivial dynamic critical exponents, which characterize the critical behavior of quenched systems [166]. Of special interest in this respect are the dynamical critical exponents of quantum phase transitions [167]. Also the observation of the Kibble-Zurek mechanism of critical slowing down [168] seems to be in reach for ultracold gases.

In our most recent experiments the role of the cavity in the experiment changed from a tool to a main ingredient of the physics investigated. By setting up an optical transport we transferred several hundred thousand atoms into the cavity mode and produced for the first time a BEC strongly coupled to the light field of a high-finesse optical cavity. This realizes a situation described by the Tavis-Cummings model, where all atoms couple identically to the cavity mode. We presented a measurement of the low-excitation energy spectrum of the coupled system and observed the square-root dependence of the energy of the dressed states on the number of atoms, as predicted by the Tavis-Cummings model [153].

The ultimate control over the external degree of freedom of a BEC together with the enhanced interaction of matter with light in a cavity opens the route to build a matter-light interface for quantum information processing [169, 170]. Our apparatus features small magnetic coils put around the cavity which allow to apply magnetic field gradients for tomography experiments. In combination with a three-dimensional optical lattice inside the cavity, even single-site addressability in a crystal of atomic qubits can be envisioned.

The compound system of BEC and quantized light field in the cavity represents a quantum optical lattice [171]: for constant pumping of the cavity, a non-local atom-atom interaction is mediated by the intracavity field, and at the same time an atom-field entanglement is introduced by the retroaction of the atomic wave function on the light. Local changes in the atomic wave function modify the coupling of the whole ensemble to the dipole potential, thereby changing the resonance condition of the coupled system. In experiments currently under progress we study this mutual non-linear and non-local feedback and observe strong, periodic oscillations in the cavity output. Whereas the behavior of a BEC of dilute gases is in many situations very similar to the behavior of superfluid helium, this analogy breaks down in this new kind of experiments, where the atomic external degree of freedom is coupled to the light field.

A Bose-Einstein Condensation

Bose-Einstein condensation is the simplest form of an off-diagonal long-range order (C.N. Yang in [19])

This section gives an introduction to the theory of Bose-Einstein condensation. Following the textbook of Pitaevskii and Stringari [172] we will first introduce the concept of off-diagonal long-range order, which gives a definition of Bose-Einstein condensation and will be of great importance for most of the experiments described in this thesis. The order parameter of the Bose-Einstein condensate is introduced, before the main characteristics of a condensed Bose gas are given for the situation of a trapped, weakly interacting gas. For more details the reader is referred to textbooks [172, 173] and to some extensive overview articles [174, 175, 92, 176].

A.1 Off-Diagonal Long-Range Order

A system with a macroscopic eigenvalue in the one-particle density matrix is said to exhibit off-diagonal long-range order (ODLRO). Remote portions of a system possessing ODLRO will show correlated behavior. Off-diagonal long-range order is a key issue in the description of Bose-Einstein condensation (BEC), and is often also used for the definition of BEC. The concept of off-diagonal long-range order was introduced by Yang [19], who tied up to the work of Penrose and Onsager [177, 18] on the one-particle density matrix of a Bose condensed system.

Let us consider a many-particle system with the total number of particles N and a density matrix ρ expressed as the one-particle density matrix

$$\rho^{(1)}(\mathbf{r},\mathbf{r}') = \langle \mathbf{r}|\rho^{(1)}|\mathbf{r}'\rangle = \langle \hat{\Psi}^\dagger(\mathbf{r})\hat{\Psi}(\mathbf{r}')\rangle\,, \tag{A.1}$$

where $\hat{\Psi}^\dagger(\mathbf{r})$ (or $\hat{\Psi}(\mathbf{r})$) is the field operator creating (or annihilating) a particle at position $\mathbf{r}$ and the brackets $\langle\cdot\rangle$ symbolize an ensemble average. Equation (A.1) is valid for any system, independent of statistics or equilibrium conditions. In the following we consider a system of bosons for which the

field operators obey the commutation relations

$$[\hat{\Psi}(\mathbf{r}), \hat{\Psi}^\dagger(\mathbf{r}')] = \delta(\mathbf{r} - \mathbf{r}'), \quad [\hat{\Psi}(\mathbf{r}), \hat{\Psi}(\mathbf{r}')] = 0\,. \tag{A.2}$$

The one-particle density matrix furnishes the expectation values of single-particle observables such as the momentum or position density of the gas. It can also be identified with the first-order correlation function [49] of the system. Evaluating the one-particle density matrix for only one point in space ($\mathbf{r} = \mathbf{r}'$) one finds the density of the gas at this position

$$n(\mathbf{r}) = \langle \hat{\Psi}^\dagger(\mathbf{r}) \hat{\Psi}(\mathbf{r}) \rangle\,, \tag{A.3}$$

from which the normalization condition for the one-particle density matrix is given by the total number of particles $N = \int n(\mathbf{r}) \mathrm{d}\mathbf{r}$. Writing the field operator in momentum representation, the momentum distribution of the gas is

$$n(\mathbf{p}) = \langle \hat{\Psi}^\dagger(\mathbf{p}) \hat{\Psi}(\mathbf{p}) \rangle\,. \tag{A.4}$$

For a uniform and isotropic system in the thermodynamic limit, $\rho^{(1)}(\mathbf{r}, \mathbf{r}')$ depends only on the modulus of the relative coordinate $r = |\mathbf{r} - \mathbf{r}'|$. One finds the relation between the one-body density matrix and the momentum density by taking the Fourier transform [18, 178]

$$\rho^{(1)}(r) = \frac{1}{V} \int n(\mathbf{p}) e^{-i\mathbf{p}\cdot(\mathbf{r}-\mathbf{r}')/\hbar} \mathrm{d}\mathbf{p}\,, \tag{A.5}$$

where V is the volume of the system.

Definition of the Bose-Einstein Condensate

A thermal gas shows a smooth momentum distribution $n(\mathbf{p})$, so that the one-particle density matrix vanishes for $r \to \infty$. The situation changes if a macroscopic number N_0 of particles occupy one momentum state (e.g. $\mathbf{p} = 0$)

$$n(\mathbf{p}) = N_0 \delta(\mathbf{p}) + \tilde{n}(\mathbf{p})\,. \tag{A.6}$$

The singular term in Equation A.6 characterizes the macroscopic population in $\mathbf{p} = 0$, while the second term describes the momentum distribution for all particles with $\mathbf{p} \neq 0$. Using (A.5) one finds that the one-particle density matrix $\rho^{(1)}(r)$ does not vanish any more for $r \to \infty$ but strives to a constant value

$$\rho^{(1)}(r) \underset{r\to\infty}{\to} \frac{N_0}{V}\,. \tag{A.7}$$

This non-vanishing behavior is often used as a general definition for a Bose-Einstein condensate. Since the one-particle density matrix is different from

zero for $|\mathbf{r}-\mathbf{r}'| \to \infty$, condition (A.7) is a condition for ODLRO, involving the non-diagonal elements ($\mathbf{r} \neq \mathbf{r}'$) of $\rho^{(1)}(\mathbf{r},\mathbf{r}')$. The presence of ODLRO is equivalent to the occurrence of long-ranged phase coherence in the system. Following (A.6), Bose-Einstein condensation sets in when a single quantum state is macroscopically populated.

Finally, we can diagonalize the one-particle density matrix [172] and expand it in the basis of the single-particle wave functions ϕ_i with the eigenvalues n_i

$$\rho^{(1)}(\mathbf{r},\mathbf{r}') = N_0\phi_0^*(\mathbf{r})\phi_0(\mathbf{r}') + \sum_{i\neq 0} n_i\phi_i^*(\mathbf{r})\phi_i(\mathbf{r}')\,, \tag{A.8}$$

where we again separated the contributions of the macroscopically populated state (the Bose-Einstein condensate) with wave function $\phi_0(\mathbf{r})$ and eigenvalue N_0 from the other single-particle states $\phi_{i\neq 0}(\mathbf{r})$. The sum goes to zero for large distances, whereas the first term ensures a finite value of $\rho^{(1)}(\mathbf{r},\mathbf{r}')$ for distances $r = |\mathbf{r}-\mathbf{r}'|$ which are smaller than the extension of $\phi_0(\mathbf{r})$.

First Order Correlation Function

The normalized spatial correlation function is defined as

$$g^{(1)}(\mathbf{r},\mathbf{r}') = \frac{\rho^{(1)}(\mathbf{r},\mathbf{r}')}{\sqrt{\rho^{(1)}(\mathbf{r},\mathbf{r})}\sqrt{\rho^{(1)}(\mathbf{r}',\mathbf{r}')}} = \frac{\rho^{(1)}(\mathbf{r},\mathbf{r}')}{\sqrt{n(\mathbf{r})}\sqrt{n(\mathbf{r}')}}\,. \tag{A.9}$$

It describes the phase correlations of the quantum field, reaching unity for perfect correlations and going to zero for vanishing correlations. If the condition for ODLRO (A.7) is fulfilled, the normalized correlation function $g^{(1)}(\mathbf{r},\mathbf{r}')$ will tend for increasing $r = |\mathbf{r}-\mathbf{r}'|$ to the constant value N_0/N which is the condensate fraction. We again can separate the contribution of the BEC and of the non-condensed, thermal part of the system to the correlation function

$$g^{(1)}(\mathbf{r},\mathbf{r}') = \frac{N_0}{N} + g^{(1)}_{\mathrm{th}}(\mathbf{r},\mathbf{r}')\,. \tag{A.10}$$

For a Bose-Einstein condensate at finite temperature, the first order correlation function $g^{(1)}(\mathbf{r},\mathbf{r}')$ shows for small distances $r = |\mathbf{r}-\mathbf{r}'| \to 0$ perfect correlations and decays to a finite value for large distances. This value corresponds to the degree of long-range correlations of the system. For a thermal gas N_0 vanishes and the first order correlation function is given by $g^{(1)}_{\mathrm{th}}(\mathbf{r},\mathbf{r}')$, which—away from the phase transition—falls off to zero exponentially on a length scale given by the thermal de Broglie wavelength λ_{dB}

$$g^{(1)}_{\mathrm{th}}(\mathbf{r},\mathbf{r}') \propto e^{-\pi\frac{|\mathbf{r}-\mathbf{r}'|^2}{\lambda_{\mathrm{dB}}^2}}\,, \quad \text{with} \quad \lambda_{\mathrm{dB}} = \sqrt{\frac{2\pi\hbar^2}{mk_{\mathrm{B}}T}}\,, \tag{A.11}$$

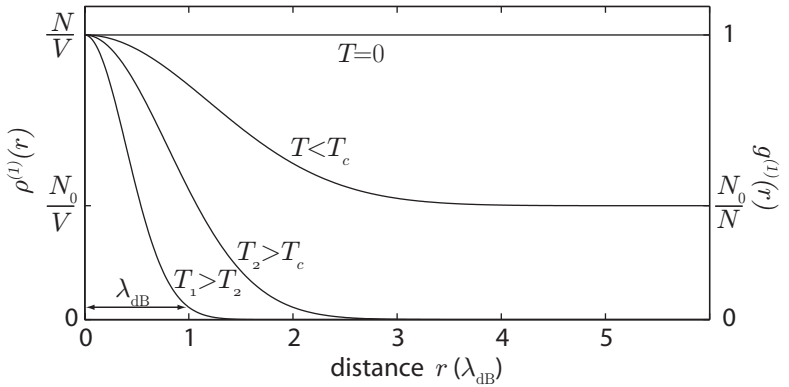

FIGURE A.1: First-order correlation function $\rho^{(1)}(r)$ of a Bose gas as a function of distance for different temperatures. On the right y-axis, the normalized values of the correlation function, $g^{(1)}(r)$, are displayed, being unity for perfect phase correlations and zero for vanishing correlations. The correlation function above the critical temperature T_c decays approximately as a Gaussian to zero, on a length scale given by the de Broglie wave length λ_{dB}. The length scale over which correlations exist becomes larger for lower temperatures ($T_2 < T_1$). The correlation function drops to a constant value, the condensate fraction, for temperatures below the transition temperature, and is unity for $T = 0$ in the case of an ideal Bose gas.

where m is the mass of the atom, k_{B} is the Boltzmann constant and T is the temperature of the gas. The shape of the first order correlation function is illustrated in Figure A.1. The behavior in proximity to the phase transition is discussed in Section 2.1.3.

A.2 Order Parameter

The field operator $\hat{\Psi}$ can be expanded in the basis of the single-particle wave functions ϕ_i introduced in (A.8)

$$\hat{\Psi}(\mathbf{r}) = \phi_0(\mathbf{r})\hat{a}_0 + \sum_{i\neq 0} \phi_i(\mathbf{r})\hat{a}_i \,, \tag{A.12}$$

where $\hat{a}_i^\dagger$ (or $\hat{a}_i$) is the operator creating (or annihilating) a particle in state ϕ_i. The separation on the right hand side of Equation (A.12) again reflects the special role of the macroscopically populated state.

For $N_0 = \langle \hat{a}_0^\dagger \hat{a}_0 \rangle \gg 1$ the Bogoliubov approximation [179] can be applied: the component $\phi_0(\mathbf{r})\hat{a}_0$ of the field operator is treated as a classical field by replacing the operators $\hat{a}_0^\dagger$ and $\hat{a}_0$ by $\sqrt{N_0}$, so that $\phi_0(\mathbf{r})\hat{a}_0 \approx \sqrt{N_0}\phi_0(\mathbf{r}) \equiv \psi(\mathbf{r})$. The field operator (A.12) can now be written as

$$\hat{\Psi}(\mathbf{r}) = \psi(\mathbf{r}) + \delta\hat{\Psi}(\mathbf{r}) \,, \tag{A.13}$$

where $\delta\hat{\Psi}(\mathbf{r}) = \sum_{i\neq 0} \phi_i(\mathbf{r})\hat{a}_i$ is a fluctuating function with $\langle \delta\hat{\Psi}(\mathbf{r}) \rangle = 0$.

The function $\psi(\mathbf{r}) = |\psi(\mathbf{r})|e^{i\phi(\mathbf{r})}$ is a complex quantity with an amplitude and a phase and is called the macroscopic wave function of the Bose-Einstein condensate. It plays the role of an order parameter for Bose-Einstein condensation, as it characterizes the Bose condensed phase and vanishes above the critical temperature.

With this new expression of the field operator, we can rewrite the first order correlation function (A.10),

$$g^{(1)}(\mathbf{r},\mathbf{r}') = \langle \hat{\Psi}^\dagger(\mathbf{r})\hat{\Psi}(\mathbf{r}') \rangle = \psi^*(\mathbf{r})\psi(\mathbf{r}') + \langle \delta\hat{\Psi}^\dagger(\mathbf{r})\delta\hat{\Psi}(\mathbf{r}') \rangle \,, \tag{A.14}$$

where the condensate wave function $\psi(\mathbf{r})$ gives rise to the long-range phase coherence of the system, and the fluctuating part $\delta\hat{\Psi}(\mathbf{r})$ is responsible for the correlations in the excitation spectrum.

A.3 Ideal Bose Gas in a Trap

For a gas of N noninteracting bosons in a three-dimensional trap, the mean number of particles n_{ϵ_i} in the energy eigenstate with energy ϵ_i is given by the Bose-Einstein distribution

$$n_{\epsilon_i} = \frac{1}{e^{(\epsilon_i - \mu)\beta} - 1} \,, \tag{A.15}$$

where μ is the chemical potential and $\beta = 1/(k_\mathrm{B}T)$ with the temperature T and the Boltzmann constant k_B. The chemical potential can be found self-consistently from the normalization to the total number of atoms. The Bose-Einstein distribution (A.15) sets the important physical constraint $\mu < \epsilon_0$ on the chemical potential. A chemical potential bigger than the lowest energy eigenstate would violate this inequality and lead to negative occupation numbers for all states with energy smaller than μ. It follows that for $\mu \to \epsilon_0$ the occupation number N_0 for the lowest energy state becomes increasingly large: Bose-Einstein condensation sets in.

Typical experiments with Bose-Einstein condensates use trapping geometries which can well be approximated by a three dimensional harmonic oscillator

$$V_\mathrm{ext}(\mathbf{r}) = \frac{1}{2}m\left(\omega_\mathrm{x}^2 x^2 + \omega_\mathrm{y}^2 y^2 + \omega_\mathrm{z}^2 z^2\right) \,, \tag{A.16}$$

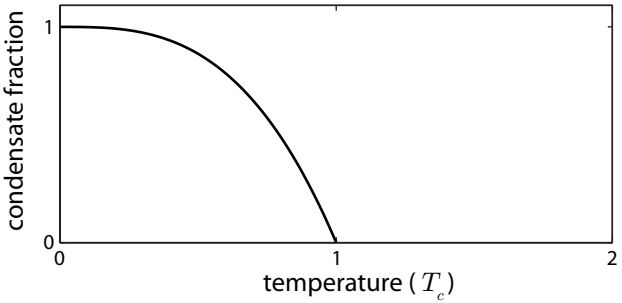

FIGURE A.2: Condensate fraction of a Bose gas as function of temperature. Above the critical temperature the condensate fraction is zero.

where m is the mass of an atom, and the ω_i are the trapping frequencies of the potential. The transition temperature T_c for a trapped, ideal Bose gas depends on the total number of atoms N and on the trapping frequencies

$$T_c = \frac{\hbar\bar{\omega}}{k_B}\left(\frac{N}{g_3(1,0)}\right)^{1/3}, \tag{A.17}$$

where we used the geometric average of the trapping frequencies $\bar{\omega} = (\omega_x\omega_y\omega_z)^{1/3}$ and have introduced the generalized Bose function [49]

$$g_\alpha(x,y) = \sum_{k=1}^{\infty}\frac{x^k y^{1/k}}{k^\alpha}. \tag{A.18}$$

The transition temperature T_c for the ideal gas is very close to the measured value for the weakly interacting gas. The deviations can be explained in more advanced theories [78, 83, 80, 180], taking into account the interactions, the finite number of particles in the system and the anisotropy of the potential.

Using the above definition for the transition temperature, the condensate fraction N_0/N as a function of temperature $T < T_c$ is given by

$$\frac{N_0}{N} = 1 - \left(\frac{T}{T_c}\right)^3; \tag{A.19}$$

This dependence is depicted in Figure A.2.

The radial extension of a trapped thermal cloud at temperature T is given by $R_{th} = \sqrt{2k_BT/(m\bar{\omega}^2)}$, so that the interatomic distance can be estimated to be $l = R_{th}/N^{1/3}$. A demonstrative interpretation of Bose-Einstein condensation is to compare the interatomic distance with the de

Broglie wavelength λ_{dB} (see Equation A.11) of the particles. At the critical temperature T_{c}, the extension of the wave packets λ_{dB} becomes comparable to l such that the particle wave functions start to overlap and the particles become indistinguishable.

A.4 Trapped Weakly Interacting Bose Gas

In a real gas particles can interact with each other via their two-body interatomic potential. At ultra-low temperatures the thermal energy can be neglected with respect to the interaction energy. One assumes that the collisions can be completely characterized by the s-wave scattering length a, that collisions do not change the internal state of the atoms, and that the gas is so dilute that only binary collisions are relevant. These assumptions are justified if the diluteness condition $n|a|^3 \ll 1$ is fulfilled, which is the case for typical experimental parameters where the density n is on the order of $10^{14}\,\mathrm{cm}^{-3}$ and $a \simeq 5.7\,\mathrm{nm}$. The interaction potential $V_0(\mathbf{r}-\mathbf{r}')$ can then be written in the Born approximation as an effective contact interaction

$$V_0(\mathbf{r}-\mathbf{r}') = U_0\delta(\mathbf{r}-\mathbf{r}') \quad \text{with} \quad U_0 = \frac{4\pi\hbar^2 a}{m}\,. \tag{A.20}$$

If the atom-atom interactions are incorporated in a mean-field approach, the Gross-Pitaevskii equation [181, 182] can be derived, which is the main theoretical tool for the description of a trapped, interacting Bose gas at ultra-low temperatures:

$$i\hbar\frac{\partial}{\partial t}\psi(\mathbf{r},t) = \left(-\frac{\hbar^2\nabla^2}{2m} + V_{\mathrm{ext}}(\mathbf{r},t) + U_0\,|\psi(\mathbf{r},t)|^2\right)\psi(\mathbf{r},t)\,. \tag{A.21}$$

The Gross-Pitaevskii equation resembles a Schrödinger equation for the condensate wave function $\psi(\mathbf{r},t)$, including the additional nonlinear mean-field term $U_0\,|\psi(\mathbf{r},t)|^2$.

Thomas-Fermi Approximation

If the zero-point energy of the harmonic oscillator is small compared to the interaction energy per particle, the kinetic energy term in the stationary form of the Gross-Pitaevskii Equation (A.21) can be neglected. One obtains the so-called Thomas-Fermi approximation for the condensate wave function

$$\psi(\mathbf{r}) = \begin{cases} \sqrt{\frac{\mu - V_{\mathrm{ext}}(\mathbf{r})}{U_0}}\,, & \text{for} \quad V_{\mathrm{ext}}(\mathbf{r}) < \mu \\ 0\,, & \text{for} \quad V_{\mathrm{ext}}(\mathbf{r}) > \mu\,. \end{cases} \tag{A.22}$$

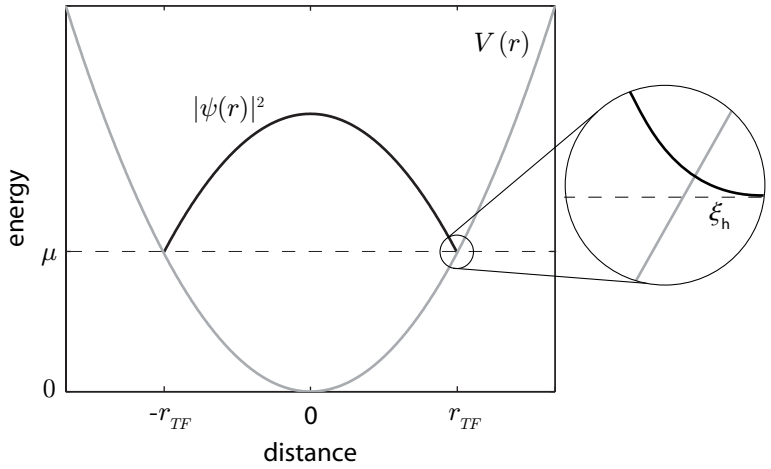

FIGURE A.3: Harmonic trapping potential (grey) $V(r)$ and the corresponding density distribution (black) $|\psi(r)|^2$ in the Thomas-Fermi approximation—the density distribution resembles the inverted trapping potential. The Thomas-Fermi approximation breaks down at the edges of the atomic cloud, where the wave function does not directly goes to zero but decays on a length scale given by the healing length ξ_h (inset).

This approximation is valid for $Na/a_\mathrm{HO} \gg 1$, where $a_\mathrm{HO} = \sqrt{\hbar/(m\bar{\omega})}$ is the characteristic length scale of the quantum mechanical harmonic oscillator. As a consequence of (A.22), the density distribution $n(\mathbf{r}) = |\psi(\mathbf{r})|^2$ resembles the shape of the inverted external potential. The radius of a trapped interacting Bose condensate can now be calculated as the Thomas-Fermi radius

$$r_\mathrm{TF} = \sqrt{\frac{2\mu_\mathrm{TF}}{m\omega_i^2}}\,, \tag{A.23}$$

where the chemical potential in the Thomas-Fermi approximation

$$\mu_\mathrm{TF} = \frac{\left(15\hbar^2 a\bar{\omega}^3 N_0\sqrt{m}\right)^{2/5}}{2} \tag{A.24}$$

has been introduced. The external potential and the resulting density distribution are illustrated in Figure A.3.

The Thomas-Fermi approximation neglects the kinetic energy term in the Gross-Pitaevskii equation. This is a good assumption, if the shape of the wave function changes only slowly. However, on the edges of the condensate the Thomas-Fermi approximation breaks down and predicts a sharp bend of the density distribution. In contrast, the solution of the Gross-Pitaevskii-equation shows a smooth decay of the density on a length scale given by the healing length $\xi_{\mathrm{h}} = (8\pi na)^{-1/2}$ (see Figure A.3).

B Approximation of the First-Order Correlation Function

We show here the calculation needed to approximate the first order correlation function (2.22)

$$\langle\hat{\Psi}^\dagger(z)\hat{\Psi}(z')\rangle = \frac{1}{\lambda_{\mathrm{dB}}^3}\sum_{s=1}^{\infty}\frac{1}{s^{3/2}}e^{s\mu/k_{\mathrm{B}}T}e^{-\frac{1}{s}\pi\frac{\Delta z^2}{\lambda_{\mathrm{dB}}^2}}$$

to find the asymptotic from (2.24)

$$\langle\hat{\Psi}^\dagger(z)\hat{\Psi}(z')\rangle \to \frac{1}{\Delta z}e^{-\Delta z/\xi}\,.$$

In a first approximation, the sum is transferred into an integral. Furthermore we are only interested in the proportionalities and neglect the pre-factors:

$$\langle\hat{\Psi}^\dagger(z)\hat{\Psi}(z')\rangle \approx\propto \int_1^\infty \mathrm{d}s\,\frac{1}{s^{3/2}}e^{s\frac{\mu}{k_{\mathrm{B}}T}}e^{-\frac{1}{s}\pi\frac{\Delta z^2}{\lambda_{\mathrm{dB}}^2}}\,.$$

Substituting $\mu' = -\frac{\mu}{k_{\mathrm{B}}T}$ and $r'^2 = \pi\frac{\Delta z^2}{\lambda^2}$ this yields

$$= \int_1^\infty \mathrm{d}s\,\frac{1}{s^{3/2}}e^{-s\mu'}e^{-\frac{r'^2}{s}} = \int_1^\infty \mathrm{d}s\,e^{-s\mu'-\frac{r'^2}{s}-\frac{3}{2}\ln s} = \int_1^\infty \mathrm{d}s\,e^{g(s)}\,,$$

with the function $g(s) = -(\frac{r'^2}{s}+s\mu'+\frac{3}{2}\ln s)$ in the exponent. The maximum $s_{\max}$ of $g(s)$ can be found from its first and second derivative. Now the saddle point method can be used to evaluate the integral:

$$\int_1^\infty \mathrm{d}s\,e^{g(s)} \approx \int_{-\infty}^\infty \mathrm{d}s e^{g(s_{\max})+g''(s_{\max})\frac{(s-s_{\max})^2}{2}} = \sqrt{2\pi}e^{g(s_{\max})}\frac{1}{\sqrt{-g''(s_{\max})}}\,.$$

Here we find $g''(s) = -2\frac{r'^2}{s^3} + \frac{3}{2}\frac{1}{s^2}$, and $s_{\max}$ can be approximated with an expansion in $1/r'$, i.e., for $r'^2 \gg 1$ equivalent to $\Delta z^2 \gg \lambda^2/\pi$.

$$s_{\max} = \frac{-3/2 \pm \sqrt{(3/2)^2 + 4\mu' r'^2}}{2\mu'} \approx -\frac{3}{4\mu'} + \frac{r'}{\sqrt{\mu'}} + O(1/r')\,,$$

such that

$$g(s_{\max}) \approx -\frac{r'^2}{\frac{r'}{\sqrt{\mu'}} - \frac{3}{4\mu'}} - \sqrt{\mu'}r' + \frac{3}{4} - \frac{3}{2}ln(\frac{r'}{\sqrt{\mu'}} - \frac{3}{4\mu'})\,.$$

This again can be approximated for $r' \gg 1$, or — more precisely — for $\Delta z \gg \lambda$

$$g(s_{\max}) \approx -2\sqrt{\mu'}r' - \frac{3}{2}\ln(\frac{r'}{\sqrt{\mu'}})\,.$$

The second derivative of g at $s_{\max}$ is found to be

$$g''(s_{\max}) \approx -2\frac{r'^2}{(\frac{r'}{\sqrt{\mu'}} - \frac{3}{4\mu'})^3} + \frac{3}{2}\frac{1}{(\frac{r'}{\sqrt{\mu'}} - \frac{3}{4\mu'})^2} \approx -2\frac{\mu'^{3/2}}{r'}\,.$$

Now we can apply the saddle-point approximation and evaluate the integral

$$\int_1^\infty \mathrm{d}s e^{g(s)} \approx \sqrt{2\pi}e^{-2\sqrt{\mu'}r'}\left(\frac{r'}{\sqrt{\mu'}}\right)^{-3/2}\left(\frac{r'}{2\mu'^{3/2}}\right)^{1/2} = \sqrt{2\pi}e^{-2\sqrt{\mu'}r'}\frac{1}{r'}\,.$$

After back transformation of r' and μ' we find for the asymptotic correlation function

$$\langle\hat{\Psi}^\dagger(z)\hat{\Psi}(z')\rangle \to \frac{1}{\Delta z}e^{-2\Delta z\sqrt{\frac{\pi|\mu|}{k_\mathrm{B}T\lambda_\mathrm{dB}^2}}}$$

So finally, by introducing the expression $\xi = \sqrt{\frac{\hbar^2}{2m|\mu|}}$, the first order correlation function can be written in the familiar form for large $\Delta z = z - z'$

$$\langle\hat{\Psi}^\dagger(z)\hat{\Psi}(z')\rangle \to \frac{1}{\Delta z}e^{-\frac{\Delta z}{\xi}}\,.$$

C Derivation of the Visibility of the Interference Pattern

In our experiment we output couple atoms from the trap and measure the time-dependent flux of atoms falling through the cavity mode. This quantity can be described in our one-dimensional model by the expectation value of the atomic density at the position r_0 of the cavity

$$\left\langle \hat{\Psi}_f^\dagger(r_0,t)\hat{\Psi}_f(r_0,t)\right\rangle \quad =$$

$$\begin{aligned}
&= \left\langle \left(\varphi_{z1}(r_0)\langle\varphi_{z1}|\hat{\Psi}_t\rangle e^{-i\omega_{z1}t} + \varphi_{z2}(r_0)\langle\varphi_{z2}|\hat{\Psi}_t\rangle e^{-i\omega_{z2}t}\right)^\dagger \cdot \right. \\
&\quad \left. \cdot \left(\varphi_{z1}(r_0)\langle\varphi_{z1}|\hat{\Psi}_t\rangle e^{-i\omega_{z1}t} + \varphi_{z2}(r_0)\langle\varphi_{z2}|\hat{\Psi}_t\rangle e^{-i\omega_{z2}t}\right)\right\rangle \\
&= \varphi_{z1}^2(r_0)\left\langle\langle\varphi_{z1}|\hat{\Psi}_t\rangle^\dagger\langle\varphi_{z1}|\hat{\Psi}_t\rangle\right\rangle + \varphi_{z2}^2(r_0)\left\langle\langle\varphi_{z2}|\hat{\Psi}_t\rangle^\dagger\langle\varphi_{z2}|\hat{\Psi}_t\rangle\right\rangle + \\
&\quad + \varphi_{z1}(r_0)\varphi_{z2}(r_0)\left\langle\langle\varphi_{z1}|\hat{\Psi}_t\rangle^\dagger\langle\varphi_{z2}|\hat{\Psi}_t\rangle e^{-i\Delta\omega t} + \langle\varphi_{z2}|\hat{\Psi}_t\rangle^\dagger\langle\varphi_{z1}|\hat{\Psi}_t\rangle e^{+i\Delta\omega t}\right\rangle .
\end{aligned}$$

Using the symmetry of the correlation function in its arguments this can be written as

$$\begin{aligned}
&= \varphi_{z1}^2(r_0)\int \varphi_{z1}^2(x)\langle\hat{\Psi}_t^\dagger(x)\hat{\Psi}_t(x)\rangle \mathrm{d}x + \varphi_{z2}^2(r_0)\int \varphi_{z2}^2(x)\langle\hat{\Psi}_t^\dagger(x)\hat{\Psi}_t(x)\rangle \mathrm{d}x + \\
&\quad + 2\varphi_{z1}(r_0)\varphi_{z2}(r_0)\int \varphi_{z1}(x_1)\varphi_{z2}(x_2)\langle\hat{\Psi}_t^\dagger(x_1)\hat{\Psi}_t(x_2)\rangle \mathrm{d}x_1\mathrm{d}x_2\cos(\Delta\omega t) .
\end{aligned}$$

In the above equation the relation between the measured flux of atoms and the correlation function of the trapped gas becomes visible. Following [49] the correlation function of the Bose gas $\left\langle\hat{\Psi}_t^\dagger(x_1)\hat{\Psi}_t(x_2)\right\rangle$ can be written as a sum $\sum_k 1/k^{3/2}\Gamma^k(R)\gamma^{1/k}(r)$ (see Equation 2.21), where $\Gamma(R)$ depends only on the center-of-mass coordinate $R = (x_1 + x_2)/2$ and $\gamma(r)$ depends only on the relative coordinate $r = x_1 - x_2$. In the following we use only the lowest

order term of this sum as the correlation function. However, the discussion is valid for each summand, and the full result can be obtained by summing over all contributions.

Until now we assumed the detector as having no extension in direction of the atomic beam. However, the cavity mode waist determines a finite detection volume, over which the flux has to be integrated. The pre-factors in front of the integrals are represented by very fast oscillating Airy functions. At the position r_0 of the cavity the wavelength of these functions is only a few nanometers which is much smaller than the cavity mode waist. Integrating over the size of the cavity mode leads to equal and constant pre factors B for the first two terms of the sum. The pre-factor of the last term is slowly oscillating in space, but its maximum value is again equal to the two other pre-factors. We now can write

$$\begin{aligned} &= B\left(\int \varphi_{z1}^2(R) e^{-\frac{R^2}{2R_{\mathrm{th}}^2}}\,\mathrm{d}R + \int \varphi_{z2}^2(R) e^{-\frac{R^2}{2R_{\mathrm{th}}^2}}\,\mathrm{d}R \right. \\ &\quad \left. + \int \varphi_{z1}(R+r/2)\varphi_{z2}(R-r/2) e^{-\frac{R^2}{2R_{\mathrm{th}}^2}} e^{-\pi\frac{r^2}{\lambda_{\mathrm{dB}}^2}}\,\mathrm{d}R\mathrm{d}r\cos(\Delta\omega t)\right), \end{aligned}$$

where we introduced the radius of a trapped thermal cloud $R_{\mathrm{th}} = \sqrt{k_{\mathrm{B}}T/(m\omega^2)}$.

The first two terms of the sum can be evaluated numerically yielding a value $1/(2A)$ with a constant A. To be only dependent on the distance Δz of the output coupling planes, we make the coordinate transformation $\tilde{r} = r + \Delta z$ with $\Delta z = |z_1 - z_2|$ and choose z_1, z_2 symmetric with respect to the origin of the coordinate system

$$\begin{aligned} &= \frac{B}{A}\left(1 + A\int e^{-\pi\frac{(\tilde{r}-\Delta z)^2}{\lambda_{\mathrm{dB}}^2}} \int \varphi_{-\tilde{r}/2}(R)\varphi_{\tilde{r}/2}(R) e^{-\frac{R^2}{2R_{\mathrm{th}}^2}}\,\mathrm{d}R\mathrm{d}\tilde{r}\cos(\Delta\omega t)\right) \\ &\propto \left(1 + V(\Delta z)\cos(\Delta\omega t)\right), \end{aligned}$$

with

$$V(\Delta z) = A\int e^{-\pi\frac{(\tilde{r}-\Delta z)^2}{\lambda_{\mathrm{dB}}^2}} \int \varphi_{-\tilde{r}/2}(R)\varphi_{\tilde{r}/2}(R) e^{-\frac{R^2}{2R_{\mathrm{th}}^2}}\,\mathrm{d}R\mathrm{d}\tilde{r}$$

We now derived Equation 4.18 and continue with the further discussion in the main text.

D Physical Constants

All physical constants used in this thesis are published in [183] and can be accessed via `http://physics.nist.gov/constants`. The data concerning ^{87}Rb has been taken from [99] and can be accessed via `http://steck.us/alkalidata/`.

Bibliography

[1] M. H. Anderson, J. R. Ensher, M. R. Matthews, C. E. Wieman, and E. A. Cornell. 'Observation of Bose-Einstein Condensation in a Dilute Atomic Vapor'. *Science* **269**, 198–201 (1995).

[2] K. B. Davis, M. O. Mewes, and W. Ketterle. 'An analytical model for evaporative cooling of atoms'. *Appl. Phys. B* **60**(2-3), 155–159 (1995).

[3] H.-J. Miesner, D. M. Stamper Kurn, M. R. Andrews, D. S. Durfee, S. Inouye, and W. Ketterle. 'Bosonic Stimulation in the Formation of a Bose-Einstein Condensate'. *Science* **279**(5353), 1005–1007 (1998).

[4] M. Köhl, M. J. Davis, C. W. Gardiner, T. W. Hänsch, and T. Esslinger. 'Growth of Bose-Einstein Condensates from Thermal Vapor'. *Phys. Rev. Lett.* **88**(8), 080402 (2002).

[5] I. Shvarchuck, C. Buggle, D. S. Petrov, K. Dieckmann, M. Zielonkowski, M. Kemmann, T. G. Tiecke, W. von Klitzing, G. V. Shlyapnikov, and J. T. M. Walraven. 'Bose-Einstein Condensation into Nonequilibrium States Studied by Condensate Focusing'. *Phys. Rev. Lett.* **89**(27), 270404 (2002).

[6] M. Hugbart, J. A. Retter, A. F. Varón, P. Bouyer, A. Aspect, and M. J. Davis. 'Population and phase coherence during the growth of an elongated Bose-Einstein condensate'. *Phys. Rev. A* **75**(1), 011602 (2007).

[7] C. Domb. *The Critical Point* (Taylor and Francis Inc. Bristol, 1996).

[8] K. Huang. *Statistical Mechanics* (John Wiley & Sons, 1987).

[9] T. Andrews. 'The Bakerian Lecture: on the Continuity of the Gaseous and Liquid States of Matter'. *Phil. Trans. R. Soc. A* **159**, 575 (1869).

[10] J. Zinn Justin. *Quantum Field Theory and Critical Phenomena* (Oxford University Press, 1996).

[11] L. D. Landau and E. Lifshitz. *Statistical Physics* (Butterworth-Heinemann, 1980).

[12] L. Onsager. 'Crystal Statistics. I. A Two-Dimensional Model with an Order-Disorder Transition'. *Phys. Rev.* **65**, 117 (1944).

[13] K. G. Wilson. 'The renormalization group and critical phenomena'. *Rev. Mod. Phys.* **55**(3), 583 (1983).

[14] H. Kleinert and V. Schulte Frohlinde. *Critical Properties of Phi-4-Theories* (World Scientific, 2001).

[15] J. A. Lipa, J. A. Nissen, D. A. Stricker, D. R. Swanson, and T. C. P. Chui. 'Specific heat of liquid helium in zero gravity very near the lambda point'. *Phys. Rev. B* **68**(17), 174518 (2003).

[16] S. Sachdev. *Quantum Phase Transitions* (Cambridge University Press, 1999).

[17] R. P. Feynman. 'Simulating Physics With Computers'. *International Journal Of Theoretical Physics* **21**(6-7), 467–488 (1982).

[18] O. Penrose and L. Onsager. 'Bose-Einstein Condensation and Liquid Helium'. *Phys. Rev.* **104**, 576–584 (1956).

[19] C. N. Yang. 'Concept of Off-Diagonal Long-Range Order and the Quantum Phases of Liquid He and of Superconductors'. *Rev. Mod. Phys.* **34**, 694–704 (1962).

[20] I. Bloch, T. W. Hänsch, and T. Esslinger. 'Measurement of the spatial coherence of a trapped Bose gas at the phase transition'. *Nature* **403**(6766), 166–170 (2000).

[21] H. Mabuchi, Q. A. Turchette, M. S. Chapman, and H. J. Kimble. 'Real-time detection of individual atoms falling through a high-finesse optical cavity'. *Opt. Lett.* **21**(17), 1393–1395 (1996).

[22] M. Greiner, O. Mandel, T. Esslinger, T. W. Hänsch, and I. Bloch. 'Quantum phase transition from a superfluid to a Mott insulator in a gas of ultracold atoms'. *Nature* **415**(6867), 39–44 (2002).

[23] J. Binney, N. Dowrick, A. Fisher, and M. Newman. *The Theory of Critical Phenomena* (Clarendon Press Oxford, 1992).

[24] Y. M. Ivanchenko and A. A. Lisyansky. *Physics of Critical Fluctuations* (Springer-Verlag New York, 1995).

[25] E. H. Stanley. *Phase Transitions and Critical Phenomena* (Clarendon Press Oxford, 1971).

[26] M. E. Fisher. 'Renormalization group theory: Its basis and formulation in statistical physics'. *Rev. Mod. Phys.* **70**(2), 653–681 (1998).

[27] H. E. Stanley. 'Phase-Transitions - Power Laws And Universality'. *Nature* **378**(6557), 554–554 (1995).

[28] H. E. Stanley. 'Scaling, universality, and renormalization: Three pillars of modern critical phenomena'. *Rev. Mod. Phys.* **71**(2), S358 (1999).

[29] P. Weiss. 'Hypothesis of the Molecular Field and Ferromagnetism'. *Journal de Physique* **6**, 661 (1907).

[30] R. B. Griffiths. 'Dependence of Critical Indices on a Parameter'. *Phys. Rev. Lett.* **24**(26), 1479 (1970).

[31] M. E. Fisher. 'The renormalization group in the theory of critical behavior'. *Rev. Mod. Phys.* **46**(4), 597 (1974).

[32] B. Widom. 'Equation Of State In Neighborhood Of Critical Point'. *Journal Of Chemical Physics* **43**(11), 3898 (1965).

[33] M. E. Fisher and M. N. Barber. 'Scaling Theory for Finite-Size Effects in the Critical Region'. *Phys. Rev. Lett.* **28**(23), 1516 (1972).

[34] K. Damle, T. Senthil, S. N. Majumdar, and S. Sachdev. 'Phase transition of a Bose gas in a harmonic potential'. *Europhys. Lett* **36**, 7 (1996).

[35] J. A. Lipa, D. R. Swanson, J. A. Nissen, Z. K. Geng, P. R. Williamson, D. A. Stricker, T. C. P. Chui, U. E. Israelsson, and M. Larson. 'Specific Heat of Helium Confined to a 57-µm Planar Geometry near the Lambda Point'. *Phys. Rev. Lett.* **84**(21), 4894 (2000).

[36] T. Vojta. 'Computing quantum phase transitions'. arXiv:cond-mat/0709.0964 (2007).

[37] T. W. B. Kibble. 'Some Implications Of A Cosmological Phase-Transition'. *Physics Reports-Review Section Of Physics Letters* **67**(1), 183–199 (1980).

[38] W. H. Zurek. 'Cosmological Experiments In Superfluid-Helium'. *Nature* **317**(6037), 505–508 (1985).

[39] R. Monaco, J. Mygind, M. Aaroe, R. J. Rivers, and V. P. Koshelets. 'Zurek-Kibble Mechanism for the Spontaneous Vortex Formation in Nb-Al/Al_{ox}/Nb Josephson Tunnel Junctions: New Theory and Experiment'. *Phys. Rev. Lett.* **96**(18), 180604–4 (2006).

[40] M. Sprenger. 'Kritische Phänomene auf chemisch strukturierten Substraten'. Ph.D. thesis, Universität Stuttgart (2006).

[41] A. Pelissetto and E. Vicari. 'Critical phenomena and renormalization-group theory'. *Physics Reports* **368**(6), 549–727 (2002).

[42] V. L. Ginzburg. 'Some remarks on second order phase transitions and microscopic theory of ferroelectrics'. *Sov. Phys. Solid State* **2**, 1824 (1960).

[43] D. I. Uzunov. *Theory of Critical Phenomena* (World Scientific, Singapore, 1993).

[44] N. Goldenfeld. *Lectures on Phase Transitions and the Renormalization Group* (ABP Westview Press, 1992).

[45] S. Giorgini, L. P. Pitaevskii, and S. Stringari. 'Condensate fraction and critical temperature of a trapped interacting Bose gas'. *Phys. Rev. A* **54**(6), R4633 (1996).

[46] S. Wellenzohn. 'Korrelationsänge des schwach wechselwirkenden Bosegases'. Master's thesis, Technische Universität München (2008).

[47] D. R. Nelson. 'Recent Developments In Phase-Transitions And Critical Phenomena'. *Nature* **269**(5627), 379–383 (1977).

[48] L. P. Kadanoff, W. Götze, D. Hamblen, R. Hecht, E. A. S. Lewis, V. V. Palciauskas, M. Rayl, J. Swift, D. Aspnes, and J. Kane. 'Static Phenomena Near Critical Points: Theory and Experiment'. *Rev. Mod. Phys.* **39**(2), 395 (1967).

[49] M. Naraschewski and R. J. Glauber. 'Spatial coherence and density correlations of trapped Bose gases'. *Phys. Rev. A* **59**(6), 4595–4607 (1999).

[50] V. Bagnato, D. E. Pritchard, and D. Kleppner. 'Bose-Einstein condensation in an external potential'. *Phys. Rev. A* **35**(10), 4354–4358 (1987).

[51] S. M. Dutra. *Cavity Quantum Electrodynamics: The Strange Theory of Light in a Box.* Wiley Series in Lasers and Applications (Wiley-Interscience, 2005).

[52] E. M. Purcell. 'Spontaneous Emission Probabilities at Radio Frequencies'. *Phys. Rev.* **69**, 674 (1946).

[53] K. J. Vahala. 'Optical microcavities'. *Nature* **424**(6950), 839–846 (2003).

[54] H. Kogelnik and T. Li. 'Laser beams and resonators'. *Appl. Opt.* **5**(10), 1550–1567 (1966).

[55] O. Svelto and D. C. Hanna. *Principles of Lasers* (Plenum Press, 1998), 4th edition.

[56] S. Leslie, N. Shenvi, K. R. Brown, D. M. Stamper Kurn, and K. B. Whaley. 'Transmission spectrum of an optical cavity containing N atoms'. *Phys. Rev. A* **69**(4), 043805 (2004).

[57] R. H. Dicke. 'Coherence in Spontaneous Radiation Processes'. *Phys. Rev.* **93**(1), 99–110 (1954).

[58] J. Simon, H. Tanji, S. Ghosh, and V. Vuletic. 'Single-photon bus connecting spin-wave quantum memories'. *Nat Phys* **3**(11), 765–769 (2007).

[59] M. Tavis and F. W. Cummings. 'Exact Solution for an N-Molecule Radiation-Field Hamiltonian'. *Phys. Rev.* **170**(2), 379–384 (1968).

[60] H. J. Carmichael. *An Open Systems Approach to Quantum Optics.* Lecture Notes in Physics, New Series M (Springer, Berlin, 1993).

[61] P. Horak, G. Hechenblaikner, K. M. Gheri, H. Stecher, and H. Ritsch. 'Cavity-Induced Atom Cooling in the Strong Coupling Regime'. *Phys. Rev. Lett.* **79**(25), 4974–4977 (1997).

[62] G. Hechenblaikner, M. Gangl, P. Horak, and H. Ritsch. 'Cooling an atom in a weakly driven high-Q cavity'. *Phys. Rev. A* **58**(4), 3030 (1998).

[63] K. Moore. 'Ultracold Atoms, Circular Waveguides, and Cavity QED with Millimeter-scale Electromagnetic Traps'. Ph.D. thesis, University of California, Berkeley (2007).

[64] A. Öttl. 'Correlations and Counting Statistics of an Atom Laser'. Ph.D. thesis, ETH Zürich (2006).

[65] S. Ritter. 'Probing Coherence During Bose-Einstein Condensation'. Ph.D. thesis, ETH Zürich (2007).

[66] A. Öttl, S. Ritter, M. Köhl, and T. Esslinger. 'Hybrid apparatus for Bose-Einstein condensation and cavity quantum electrodynamics: Single atom detection in quantum degenerate gases'. *Rev. Sci. Instrum.* **77**, 063118 (2006).

[67] T. Esslinger, I. Bloch, and T. W. Hänsch. 'Bose-Einstein condensation in a quadrupole-Ioffe-configuration trap'. *Phys. Rev. A* **58**(4), R2664–R2667 (1998).

[68] R. W. P. Drever, J. L. Hall, F. V. Kowalski, J. Hough, G. M. Ford, A. J. Munley, and H. Ward. 'Laser phase and frequency stabilization using an optical resonator'. *Appl. Phys. B* **31**(2), 97–105 (1983).

[69] H. Mabuchi, J. Ye, and H. Kimble. 'Full observation of single-atom dynamics in cavity QED'. *Appl. Phys. B* **68**(6), 1095–1108 (1999).

[70] J. Fortágh, A. Grossmann, T. W. Hänsch, and C. Zimmermann. 'Fast loading of a magneto-optical trap from a pulsed thermal source'. *J. Appl. Phys.* **84**(12), 6499–6501 (1998).

[71] M. Greiner, I. Bloch, T. W. Hänsch, and T. Esslinger. 'Magnetic transport of trapped cold atoms over a large distance'. *Phys. Rev. A* **63**(3), 031401 (2001).

[72] S. Kuhr, W. Alt, D. Schrader, M. Muller, V. Gomer, and D. Meschede. 'Deterministic Delivery of a Single Atom'. *Science* **293**(5528), 278–280 (2001).

[73] J. A. Sauer, K. M. Fortier, M. S. Chang, C. D. Hamley, and M. S. Chapman. 'Cavity QED with optically transported atoms'. *Phys. Rev. A* **69**(5), 051804 (2004).

[74] R. Jördens. 'A Radio Frequency Source for the Preparation of Quantum States'. Master's thesis, ETH Zürich (2006).

[75] T. Donner, S. Ritter, T. Bourdel, A. Ottl, M. Kohl, and T. Esslinger. 'Critical Behavior of a Trapped Interacting Bose Gas'. *Science* **315**(5818), 1556–1558 (2007).

[76] M. Köhl, T. Donner, S. Ritter, T. Bourdel, A. Öttl, F. Brennecke, and T. Esslinger. 'Criticality and Correlations in Cold Atomic Gases'. *Advances in Solid State Physics* **47**, 79–88 (2008).

[77] R. Loudon. *The Quantum Theory of Light* (Oxford University Press, 2000), third edition.

[78] G. Baym, J.-P. Blaizot, M. Holzmann, F. Laloë, and D. Vautherin. 'The Transition Temperature of the Dilute Interacting Bose Gas'. *Phys. Rev. Lett.* **83**(9), 1703 (1999).

[79] P. Arnold and G. Moore. 'BEC Transition Temperature of a Dilute Homogeneous Imperfect Bose Gas'. *Phys. Rev. Lett.* **87**(12), 120401 (2001).

[80] V. A. Kashurnikov, N. V. Prokof'ev, and B. V. Svistunov. 'Critical Temperature Shift in Weakly Interacting Bose Gas'. *Phys. Rev. Lett.* **87**, 120402 (2001).

[81] N. Prokof'ev, O. Ruebenacker, and B. Svistunov. 'Weakly interacting Bose gas in the vicinity of the normal-fluid–superfluid transition'. *Phys. Rev. A* **69**(5), 053625–11 (2004).

[82] S. Pilati, S. Giorgini, and N. Prokof'ev. 'Critical Temperature of interacting Bose gases in two and three dimensions'. arXiv:cond-mat/0801.3424 (2008).

[83] P. Arnold and B. Tomasik. 'T_c for trapped dilute Bose gases: A second-order result'. *Phys. Rev. A* **64**(5), 053609– (2001).

[84] G. Alber and G. Metikas. 'Renormalization group analysis of a confined, interacting Bose gas'. *Applied Physics B-Lasers And Optics* **73**(8), 773–780 (2001).

[85] M. Campostrini, M. Hasenbusch, A. Pelissetto, P. Rossi, and E. Vicari. 'Critical behavior of the three-dimensional XY universality class'. *Phys. Rev. B* **63**(21), 214503 (2001).

[86] H. Kleinert. 'Critical exponents from seven-loop strong-coupling ϕ^4 theory in three dimensions'. *Physical Review D* **60**(8), 085001 (1999).

[87] Q. Niu, I. Carusotto, and A. B. Kuklov. 'Imaging of critical correlations in optical lattices and atomic traps'. *Phys. Rev. A* **73**, 053604 (2006).

[88] T. Stöferle, H. Moritz, C. Schori, M. Köhl, and T. Esslinger. 'Transition from a Strongly Interacting 1D Superfluid to a Mott Insulator'. *Phys. Rev. Lett.* **92**(13), 130403 (2004).

[89] T. Kinoshita, T. Wenger, and D. S. Weiss. 'Observation of a one-dimensional Tonks-Girardeau gas'. *Science* **305**(5687), 1125–1128 (2004).

[90] B. Paredes, A. Widera, V. Murg, O. Mandel, S. Fölling, I. Cirac, G. Shlyapnikov, T. W. Hänsch, and I. Bloch. 'Tonks-Girardeau gas of ultracold atoms in an optical lattice'. *Nature* **429**, 277 (2004).

[91] Z. Hadzibabic, P. Krüger, M. Cheneau, B. Battelier, and J. Dalibard. 'Berezinskii-Kosterlitz-Thouless crossover in a trapped atomic gas'. *Nature* **441**, 1118 (2006).

[92] F. Dalfovo, S. Giorgini, L. P. Pitaevskii, and S. Stringari. 'Theory of Bose-Einstein condensation in trapped gases'. *Rev. Mod. Phys.* **71**(3), 463–512 (1999).

[93] J. Schneider and A. Schenzle. 'Investigations of a two-mode atom-laser model'. *Phys. Rev. A* **61**(5), 053611 (2000).

[94] S. Choi, Y. Japha, and K. Burnett. 'Adiabatic output coupling of a Bose gas at finite temperatures'. *Phys. Rev. A* **61**(6), 063606 (2000).

[95] R. Ballagh and C. M. Savage. 'The Theory of Atom Lasers'. *Mod. Phys. Lett. B* **14**(Suppl. Issue 1), 153–188 (2000).

[96] Immanuel Felix Bloch. 'Atomlaser und Phasenkohärenz atomarer Bose-Einstein-Kondensate'. Ph.D. thesis, Ludwig-Maximilians-Universität München (2000).

[97] O. Vainio, C. J. Vale, M. J. Davis, N. R. Heckenberg, and H. Rubinsztein Dunlop. 'Fringe spacing and phase of interfering matter waves'. *Phys. Rev. A* **73**(6), 063613–6 (2006).

[98] F. Schwabl. *Quantenmechanik* (Springer Berlin, 2002).

[99] D. A. Steck. 'Rubidium 87 D Line Data' (2003). Revision 1.6, `http://steck.us/alkalidata`.

[100] S. Ritter, A. Öttl, T. Donner, T. Bourdel, M. Köhl, and T. Esslinger. 'Observing the Formation of Long-Range Order during Bose-Einstein Condensation'. *Phys. Rev. Lett.* **98**(9), 090402 (2007).

[101] L. S. Goldner, N. Mulders, and G. Ahlers. 'Second sound very near T_λ'. *J. Low Temp. Phys.* **93**, 131 (1993).

[102] M. J. Adriaans, D. R. Swanson, and J. A. Lipa. 'The velocity of second sound near the lambda transition in superfluid 4He'. *Physica B* **194**, 733 (1993).

[103] B. D. Josephson. 'Relation between the superfluid density and order parameter for superfluid He near Tc'. *Phys. Lett.* **21**, 608 (1966).

[104] Y. M. Kagan, B. V. Svistunov, and G. V. Shlyapnikov. 'Kinetics of Bose condensation in an interacting Bose gas'. *Sov. Phys. JETP* **75**(2), 387–393 (1992). Erratum for Sov. Physics JETP 74, 279 (1992).

[105] Y. Kagan and B. V. Svistunov. 'Kinetics of the onset of long-range order during Bose condensation in an interacting gas'. *Sov. Phys. JETP* **78**(2), 187–194 (1994).

[106] B. Svistunov. 'Strongly non-equilibrium Bose-Einstein condensation in a trapped gas'. *Phys. Lett. A* **287**(1–2), 169–174 (2001).

[107] P. D. Drummond and J. F. Corney. 'Quantum dynamics of evaporatively cooled Bose-Einstein condensates'. *Phys. Rev. A* **60**(4), R2661–R2664 (1999).

[108] A. Öttl, S. Ritter, M. Köhl, and T. Esslinger. 'Correlations and Counting Statistics of an Atom Laser'. *Phys. Rev. Lett.* **95**(9), 090404 (2005).

[109] C. W. Gardiner, M. D. Lee, R. J. Ballagh, M. J. Davis, and P. Zoller. 'Quantum Kinetic Theory of Condensate Growth: Comparison of Experiment and Theory'. *Phys. Rev. Lett.* **81**(24), 5266–5269 (1998).

[110] M. J. Bijlsma, E. Zaremba, and H. T. C. Stoof. 'Condensate growth in trapped Bose gases'. *Phys. Rev. A* **62**(6), 063609 (2000).

[111] I. Bloch, T. W. Hänsch, and T. Esslinger. 'Atom Laser with a cw Output Coupler'. *Phys. Rev. Lett.* **82**(15), 3008–3011 (1999).

[112] T. Bourdel, T. Donner, S. Ritter, A. Öttl, M. Köhl, and T. Esslinger. 'Cavity QED detection of interfering matter waves'. *Phys. Rev. A* **73**(4), 043602 (2006).

[113] Y. Le Coq, J. H. Thywissen, S. A. Rangwala, F. Gerbier, S. Richard, G. Delannoy, P. Bouyer, and A. Aspect. 'Atom Laser Divergence'. *Phys. Rev. Lett.* **87**(17), 170403 (2001).

[114] F. Gerbier, J. H. Thywissen, S. Richard, M. Hugbart, P. Bouyer, and A. Aspect. 'Momentum distribution and correlation function of quasicondensates in elongated traps'. *Phys. Rev. A* **67**(5), 051602 (2003).

[115] D. S. Petrov, G. V. Shlyapnikov, and J. T. M. Walraven. 'Phase-Fluctuating 3D Bose-Einstein Condensates in Elongated Traps'. *Phys. Rev. Lett.* **87**(5), 050404 (2001).

[116] L. de Broglie. 'Waves and Quanta'. *Nature* **112**, 540 (1923).

[117] C. Jönsson. 'Elektroneninterferenzen an mehreren künstlich hergestellten Feinspalten'. *Z. Phys.* **161**(4), 454–474 (1961).

[118] A. Tonomura, J. Endo, T. Matsuda, T. Kawasaki, and H. Ezawa. 'Demonstration of single-electron buildup of an interference pattern'. *Am. J. Phys.* **57**(2), 117–120 (1989).

[119] A. Zeilinger, R. Gähler, C. G. Shull, W. Treimer, and W. Mampe. 'Single- and double-slit diffraction of neutrons'. *Rev. Mod. Phys.* **60**(4), 1067–1073 (1988).

[120] O. Carnal and J. Mlynek. 'Young's double-slit experiment with atoms: A simple atom interferometer'. *Phys. Rev. Lett.* **66**(21), 2689–2692 (1991).

[121] D. W. Keith, C. R. Ekstrom, Q. A. Turchette, and D. E. Pritchard. 'An interferometer for atoms'. *Phys. Rev. Lett.* **66**(21), 2693–2696 (1991).

[122] F. Shimizu, K. Shimizu, and H. Takuma. 'Double-slit interference with ultracold metastable neon atoms'. *Phys. Rev. A* **46**(1), R17–R20 (1992).

[123] M. Arndt, O. Nairz, J. Vos Andreae, C. Keller, G. van der Zouw, and A. Zeilinger. 'Wave-particle duality of C60 molecules'. *Nature* **401**(6754), 680–682 (1999).

[124] Z. Hu and H. J. Kimble. 'Observation of a Single-Atom in a Magnetooptical Trap'. *Opt. Lett.* **19**(22), 1888–1890 (1994).

[125] J. L. Wiza. 'Microchannel plate detectors'. *Nucl. Instrum. Methods* **162**(1–3), 587–601 (1979).

[126] M. Schellekens, R. Hoppeler, A. Perrin, J. V. Gomes, D. Boiron, A. Aspect, and C. I. Westbrook. 'Hanbury Brown Twiss Effect for Ultracold Quantum Gases'. *Science* **310**(5748), 648–651 (2005).

[127] C. J. Hood, M. S. Chapman, T. W. Lynn, and H. J. Kimble. 'Real-Time Cavity QED with Single Atoms'. *Phys. Rev. Lett.* **80**(19), 4157–4160 (1998).

[128] P. Münstermann, T. Fischer, P. Maunz, P. W. H. Pinkse, and G. Rempe. 'Dynamics of Single-Atom Motion Observed in a High-Finesse Cavity'. *Phys. Rev. Lett.* **82**(19), 3791–3794 (1999).

[129] A. M. Herkommer, H. J. Carmichael, and W. P. Schleich. 'Localization of an atom by homodyne measurement'. *Quantum Semiclass. Opt.* **8**(1), 189–203 (1996).

[130] P. Bouyer and M. A. Kasevich. 'Heisenberg-limited spectroscopy with degenerate Bose-Einstein gases'. *Phys. Rev. A* **56**(2), R1083–R1086 (1997).

[131] C. W. Gardiner and P. Zoller. *Quantum Noise* (Springer, 1991).

[132] Jean Dalibard, Yvan Castin, and Klaus Mølmer. 'Wave-function approach to dissipative processes in quantum optics'. *Phys. Rev. Lett.* **68**(5), 580–583 (1992).

[133] K. Mølmer, Y. Castin, and J. Dalibard. 'Monte Carlo wave-function method in quantum optics'. *J. Opt. Soc. Am. B* **10**, 524 (1993).

[134] M. Köhl, T. W. Hänsch, and T. Esslinger. 'Measuring the Temporal Coherence of an Atom Laser Beam'. *Phys. Rev. Lett.* **87**(16), 160404 (2001).

[135] P. Horak, S. M. Barnett, and H. Ritsch. 'Coherent dynamics of Bose-Einstein condensates in high-finesse optical cavities'. *Phys. Rev. A* **61**(3), 033609 (2000).

[136] M. Saba, T. A. Pasquini, C. Sanner, Y. Shin, W. Ketterle, and D. E. Pritchard. 'Light Scattering to Determine the Relative Phase of Two Bose-Einstein Condensates'. *Science* **307**(5717), 1945–1948 (2005).

[137] M. Albiez, R. Gati, J. Fölling, S. Hunsmann, M. Cristiani, and M. K. Oberthaler. 'Direct Observation of Tunneling and Nonlinear Self-Trapping in a Single Bosonic Josephson Junction'. *Phys. Rev. Lett.* **95**(1), 010402 (2005).

[138] J. Javanainen and S. M. Yoo. 'Quantum phase of a Bose-Einstein condensate with an arbitrary number of atoms'. *Phys. Rev. Lett.* **76**(2), 161–164 (1996).

[139] J. I. Cirac, C. W. Gardiner, M. Naraschewski, and P. Zoller. 'Continuous observation of interference fringes from Bose condensates'. *Phys. Rev. A* **54**(5), R3714–R3717 (1996).

[140] Y. Castin and J. Dalibard. 'Relative phase of two Bose-Einstein condensates'. *Phys. Rev. A* **55**(6), 4330–4337 (1997).

[141] J. Javanainen and M. Wilkens. 'Phase and Phase Diffusion of a Split Bose-Einstein Condensate'. *Phys. Rev. Lett.* **78**(25), 4675–4678 (1997).

[142] S. J. van Enk, H. J. Kimble, and H. Mabuchi. 'Quantum Information Processing in Cavity-QED'. *Quantum Information Processing* **3**(1), 75–90 (2004).

[143] J. M. Raimond, M. Brune, and S. Haroche. 'Colloquium: Manipulating quantum entanglement with atoms and photons in a cavity'. *Rev. Mod. Phys.* **73**(3), 565 (2001).

[144] H. Walther. 'Quantum phenomena of single atoms'. *Adv. Chem. Phys.* **122**, 167–197 (2002).

[145] H. J. Kimble. 'Strong interactions of single atoms and photons in cavity QED'. *Physica Scripta* **T76**, 127–137 (1998).

[146] H. Mabuchi and A. C. Doherty. 'Cavity Quantum Electrodynamics: Coherence in Context'. *Science* **298**(5597), 1372–1377 (2002).

[147] A. D. Boozer, A. Boca, R. Miller, T. E. Northup, and H. J. Kimble. 'Cooling to the Ground State of Axial Motion for One Atom Strongly Coupled to an Optical Cavity'. *Phys. Rev. Lett.* **97**(8), 083602 (2006).

[148] S. Nußmann, K. Murr, M. Hijlkema, B. Weber, A. Kuhn, and G. Rempe. 'Vacuum-stimulated cooling of single atoms in three dimensions'. *Nat. Phys.* **1**(2), 122–125 (2005).

[149] T. Pellizzari, S. A. Gardiner, J. I. Cirac, and P. Zoller. 'Decoherence, Continuous Observation, and Quantum Computing: A Cavity QED Model'. *Phys. Rev. Lett.* **75**(21), 3788 (1995).

[150] L.-M. Duan, M. D. Lukin, J. I. Cirac, and P. Zoller. 'Long-distance quantum communication with atomic ensembles and linear optics'. *Nature* **414**(6862), 413–418 (2001).

[151] J. I. Cirac, P. Zoller, H. J. Kimble, and H. Mabuchi. 'Quantum State Transfer and Entanglement Distribution among Distant Nodes in a Quantum Network'. *Phys. Rev. Lett.* **78**(16), 3221–3224 (1997).

[152] M. Lewenstein, A. Kubasiak, J. Larson, C. Menotti, C. Morigi, K. Osterloh, and A. Sanpera. 'Travelling to exotic places with ultracold atoms'. In *Atomic Physics 20*, edited by C. Roos, H. Häffner, and R. Blatt, volume 869 of *XX International Conference on Atomic Physics; ICAP 2006*, pp. 201–211 (American Institute of Physics, 2006).

[153] F. Brennecke, T. Donner, S. Ritter, T. Bourdel, M. Kohl, and T. Esslinger. 'Cavity QED with a Bose-Einstein condensate'. *Nature* **450**(7167), 268–271 (2007).

[154] E. Jaynes and F. Cummings. 'Comparison of quantum and semiclassical radiation theories with application to the beam maser'. *Proc. IEEE* **51**(1), 89–109 (1963).

[155] M. G. Raizen, R. J. Thompson, R. J. Brecha, H. J. Kimble, and H. J. Carmichael. 'Normal-mode splitting and linewidth averaging for two-state atoms in an optical cavity'. *Phys. Rev. Lett.* **63**(3), 240–243 (1989).

[156] A. K. Tuchman, R. Long, G. Vrijsen, J. Boudet, J. Lee, and M. A. Kasevich. 'Normal-mode splitting with large collective cooperativity'. *Phys. Rev. A* **74**(5), 053821–4 (2006).

[157] Y. Colombe, T. Steinmetz, G. Dubois, F. Linke, D. Hunger, and J. Reichel. 'Strong atom-field coupling for Bose-Einstein condensates in an optical cavity on a chip'. *Nature* **450**(7167), 272–276 (2007).

[158] I. B. Mekhov, C. Maschler, and H. Ritsch. 'Probing quantum phases of ultracold atoms in optical lattices by transmission spectra in cavity quantum electrodynamics'. *Nat. Phys.* **3**, 319–323 (2007).

[159] S. Slama, S. Bux, G. Krenz, C. Zimmermann, and P. W. Courteille. 'Superradiant Rayleigh Scattering and Collective Atomic Recoil Lasing in a Ring Cavity'. *Phys. Rev. Lett.* **98**(5), 053603 (2007).

[160] K. W. Murch, K. L. Moore, S. Gupta, and D. M. Stamper Kurn. 'Measurement of Intracavity Quantum Fluctuations of Light Using an Atomic Fluctuation Bolometer'. arXiv:quant-ph/0706.1005 (2008).

[161] S. Gupta, K. L. Moore, K. W. Murch, and D. M. Stamper Kurn. 'Cavity Nonlinear Optics at Low Photon Numbers from Collective Atomic Motion'. *Phys. Rev. Lett.* **99**(21), 213601 (2007).

[162] D. Meiser and P. Meystre. 'Superstrong coupling regime of cavity quantum electrodynamics'. *Phys. Rev. A* **74**(6), 065801 (2006).

[163] M. G. Moore, O. Zobay, and P. Meystre. 'Quantum optics of a Bose-Einstein condensate coupled to a quantized light field'. *Phys. Rev. A* **60**(2), 1491–1506 (1999).

[164] A. J. Daley, P. O. Fedichev, and P. Zoller. 'Single-atom cooling by superfluid immersion: A nondestructive method for qubits'. *Phys. Rev. A* **69**(2), 022306 (2004).

[165] A. Onuki. *Phase Transition Dynamics* (Cambridge University Press, 2002).

[166] P. C. Hohenberg and B. I. Halperin. 'Theory of dynamic critical phenomena'. *Rev. Mod. Phys.* **49**(3), 435 (1977).

[167] D. Sen, K. Sengupta, and S. Mondal. 'Defect production in nonlinear quench across a quantum critical point'. arXiv:cond-mat.str-el/0803.2081 (2008).

[168] W. H. Zurek. 'Cosmological experiments in condensed matter systems'. *Physics Reports* **276**(4), 177–221 (1996).

[169] I. Chuang and M. Nielsen. *Quantum Computation and Quantum Information* (Cambridge Univ. Press, Cambridge, 2000).

[170] A. S. Sørensen and K. Mølmer. 'Measurement Induced Entanglement and Quantum Computation with Atoms in Optical Cavities'. *Phys. Rev. Lett.* **91**(9), 097905 (2003).

[171] C. Maschler and H. Ritsch. 'Cold Atom Dynamics in a Quantum Optical Lattice Potential'. *Phys. Rev. Lett.* **95**(26), 260401 (2005).

[172] L. Pitaevskii and S. Stringari. *Bose-Einstein Condensation* (Oxford University Press, 2003).

[173] C. J. Pethick and H. Smith. *Bose-Einstein Condensation in Dilute Gases* (Cambridge University Press, 2002).

[174] W. Ketterle, D. S. Durfee, and D. M. Stamper Kurn. 'Making, probing and understanding Bose-Einstein condensates'. In *Bose-Einstein Condensation in Atomic Gases*, edited by M. Inguscio, S. Stringari, and C. Wieman, volume CXL of *Proceedings of the International School of Physics Enrico Fermi*, pp. 67–176 (IOS Press, Amsterdam, 1999).

[175] A. J. Leggett. 'Bose-Einstein condensation in the alkali gases: Some fundamental concepts'. *Rev. Mod. Phys.* **73**(2), 307–50 (2001). Erratum: Rev. Mod. Phys. 75, 1083 (2003).

[176] J. R. Anglin and W. Ketterle. 'Bose-Einstein condensation of atomic gases'. *Nature* **416**(6877), 211–218 (2002).

[177] O. Penrose. 'On the Quantum Mechanics of Helium'. *Philos. Mag.* **52**, 1373–1377 (1951).

[178] F. Zambelli, L. Pitaevskii, D. M. Stamper Kurn, and S. Stringari. 'Dynamic structure factor and momentum distribution of a trapped Bose gas'. *Phys. Rev. A* **61**(6), 063608 (2000).

[179] N. Bogoliubov. 'On the theory of superfluidity'. *J. Phys. (USSR)* **11**, 23 (1947).

[180] J.-P. Blaizot. 'Non Perturbative Renormalization Group and Bose-Einstein Condensation'. arXiv:cond-mat/0801.0009 (2007).

[181] E. Gross. 'Structure of a quantized vortex in boson systems'. *Nuovo Cimento* **20**, 454 (1961).

[182] L. Pitaevskii. 'Vortex lines in an imperfect Bose gas'. *Sov. Phys. JETP* **13**, 451 (1961).

[183] P. J. Mohr and B. N. Taylor. 'CODATA recommended values of the fundamental physical constants: 2002'. *Rev. Mod. Phys.* **77**(1), 1–107 (2005).

List of Publications

1. **Cavity QED detection of interfering matter waves**
   T. Bourdel, T. Donner, S. Ritter, A. Öttl, M. Köhl, and T. Esslinger
   Phys. Rev. A 73, 043602 (2006).

2. **Time interval distributions of atoms in atomic beams**
   M. Köhl, A. Öttl, S. Ritter, T. Donner, T. Bourdel, and T. Esslinger
   Appl. Phys. B 86, 391 (2007).

3. **Observing the Formation of Long-Range Order during Bose-Einstein Condensation**
   S. Ritter, A. Öttl, T. Donner, T. Bourdel, M. Köhl, T. Esslinger
   Phys. Rev. Lett. 98, 090402 (2007).

4. **Critical Behavior of a Trapped Interacting Bose Gas**
   T. Donner, S. Ritter, T. Bourdel, A. Öttl, M. Köhl, T. Esslinger
   Science 315, 1556 (2007).

5. **Cavity QED with a Bose-Einstein condensate**
   F. Brennecke, T. Donner, S. Ritter, T. Bourdel, M. Köhl, T. Esslinger
   Nature 450, 268 (2007).

6. **Criticality and Correlations in Cold Atomic Gases**
   M. Köhl, T. Donner, S. Ritter, T. Bourdel, A. Öttl, F. Brennecke, T. Esslinger
   Advances in Solid State Physics 47, 79 (2008).

Credits

Die Zeit als Doktorand an der ETH ist sowohl beruflich als auch persönlich eine sehr schöne, reiche und glückliche Erfahrung für mich. Ich konnte in einer grossartigen, vom Wissensdrang getriebenen, herzlichen und stets fairen Arbeitsgruppe arbeiten, begegnete einer Vielzahl faszinierender physikalischer Fragestellungen (und auch einigen Antworten), und lernte hilfreiche und teilweise wundersame Techniken und Kniffe im Laboralltag kennen. Das Leben in Zürich ist ein schönes, sicher nicht zuletzt dank meiner Frau und meiner Tochter, guten Freunden und einer phantastischen WG. Es gibt also einigen Dank auszusprechen:

- zuallererst und mit ganzem Herzen Tilman Esslinger, der eine so stimulierende und erfreuliche Atomsphäre schafft, dass das Arbeiten fast immer Freude bereitet. Danke für die sprudelnden wissenschaftlichen Ideen und Diskussionen, die positive Art und die Unterstützung in jeder Hinsicht!

- Michael Köhl für Rat und Tat zu jeder Zeit, für die Hilfe zur Selbsthilfe in Theorie und Experiment und für die viele Motivation.

- Stephan Ritter und Toni Öttl, meinen zwei Vorgängern, gebührt besonderer Dank: für den Aufbau eines beeindruckend durchdachten und meist reibungslos funktionierenden Experiments, für viele spannende Diskussionen und für eine hervorragende Zusammenarbeit.

- Thomas Bourdel und Ferdinand Brennecke für fröhliches Experimentieren und ausführliche theoretische Interpretationen. Einen besonderen Dank an Ferdinand für die Hilfe bei den theoretischen Überlegungen zur Zweifrequenz-Auskopplung.

- den "altgedienten Gitterphysikern" Thilo Stöferle und Henning Moritz für anregende Diskussionen und für Beistand aus dem Nachbarlabor im Kampf mit Informatik und Optik.

- den "jungen Gitterphysikern" Ken Günter, Niels Strohmaier sowie Robert Jördens für Einblicke in ihre Gitter, freche Sprüche und die gute Stimmung. An Robert noch ein Dank für den DDS und allerlei Computer-Beistand.

- Bruno Zimmermann für die spannenden Ausflüge zu allerlei Konferenzen.

- den neuen Mitarbeitern Kristian Baumann und Christine Guerlin, Torben Müller und Jakob Meineke sowie Daniel Greif Danke für die lebendige Atmosphäre!

- für die wissenschaftliche Zusammenarbeit möchte ich mich bei Anatoly Kuklov, Wilhelm Zwerger, Gianni Blatter, Gora Shlyapnikov, Matthias Troyer, Yuri Kagan, Helmut Ritsch, Atac Imamoglu und vielen anderen herzlich bedanken.

- Alexander Frank gilt ein Dank für seinen grossartigen Einsatz, uns mit hervorragendem elektronischen Gerät zu versorgen.

- dem ETH-Team im Hintergrund, mit Jean-Pierre Stucki und Paul Herrmann, sowie der gesamten Werkstatt für die vielseitigen Beiträge zum Gelingen unserer Experimente.

- Veronica Bürgisser Danke für ihre sorgfältige und vorausschauende Arbeit im Büro, die uns so viele Dinge erleichtert.

- Danke an Curra und Enrique für die Bereitstellung des Photos auf dem Umschlag.

- meinen Eltern und meiner Schwester ein grosser Dank für all die Unterstützung und die mitgegebene Neugier.

- ein liebevoller Dank an unsere Tochter Lisa für so viele freudige Momente und so wenige unausgeschlafene Morgen.

- und ein ganz besonderer Dank gilt Michaela für ihre Liebe, Unterstützung, Lebensfreude und Geduld.

Curriculum Vitae

Personal Details

Ulrik Tobias Donner

Date of birth: 13. October, 1977
Place of birth: Uppsala, Sweden
Citizenship: German

Eichstrasse 14
8045 Zürich
Switzerland
donner@phys.ethz.ch

Education and Degrees

01/2005—05/2008	Swiss Federal Institute of Technology (ETH) Zürich *PhD Research in Quantum Optics*
06/2004	Diplom (University of Tübingen) *Diploma Thesis: Mixtures of Rubidium and Lithium in the degenerate regime*
08/2002—06/2004	University of Tübingen, Germany
09/2001—07/2002	University of Uppsala, Sweden *Scholarship holder of the German Academic Exchange Service (DAAD)*
08/2001	Vordiplom (University of Tübingen)
10/1998—08/2001	University of Tübingen, Germany *Studies in Physics (major), Mathematics and Chemistry* *Scholarship holder of the Friedrich-Ebert-Stiftung*
08/1997—09/1998	Civil Service
07/1997	Abitur (Labenwolf-Gymnasium Nürnberg, Germany)